



저작자표시-비영리-동일조건변경허락 2.0 대한민국

이용자는 아래의 조건을 따르는 경우에 한하여 자유롭게

- 이 저작물을 복제, 배포, 전송, 전시, 공연 및 방송할 수 있습니다.
- 이차적 저작물을 작성할 수 있습니다.

다음과 같은 조건을 따라야 합니다:



저작자표시. 귀하는 원저작자를 표시하여야 합니다.



비영리. 귀하는 이 저작물을 영리 목적으로 이용할 수 없습니다.



동일조건변경허락. 귀하가 이 저작물을 개작, 변형 또는 가공했을 경우에는, 이 저작물과 동일한 이용허락조건하에서만 배포할 수 있습니다.

- 귀하는, 이 저작물의 재이용이나 배포의 경우, 이 저작물에 적용된 이용허락조건을 명확하게 나타내어야 합니다.
- 저작권자로부터 별도의 허가를 받으면 이러한 조건들은 적용되지 않습니다.

저작권법에 따른 이용자의 권리는 위의 내용에 의하여 영향을 받지 않습니다.

이것은 [이용허락규약\(Legal Code\)](#)을 이해하기 쉽게 요약한 것입니다.

[Disclaimer](#)

이학박사 학위논문

**Phase competition and impurity effects  
in the single crystals of  
(Li,Na)FeAs superconductors**

(Li,Na)FeAs 초전도체 단결정에서의  
상 경쟁 및 불순물 효과 연구

2015 년 2 월

서울대학교 대학원

물리천문학부

이 범 성



# Phase competition and impurity effects in the single crystals of (Li,Na)FeAs superconductors

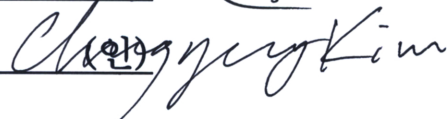
(Li,Na)FeAs 초전도체 단결정에서의  
상 경쟁 및 불순물 효과 연구

지도 교수 김기훈

이 논문을 이학박사 학위논문으로 제출함  
2014년 11월

서울대학교 대학원  
물리천문학부  
이 범 성

이범성의 이학박사 학위논문을 인준함  
2014년 12월

|      |     |   |
|------|-----|---|
| 위원장  | 차국린 | (인)  |
| 부위원장 | 김기훈 | (인)  |
| 위원   | 노태원 | (인)  |
| 위원   | 유재준 | (인)  |
| 위원   | 김창영 | (인)   |



## Abstract

# Phase competition and impurity effects in the single crystals of (Li,Na)FeAs superconductors

Bumsung Lee

Department of Physics and Astronomy

The Graduate School

Seoul National University

Fe-based superconductors are newly-found unconventional superconductors after the famous high  $T_c$  cuprate superconductors were discovered. Since the Fe-based superconductors shares many common characteristics with the high  $T_c$  cuprates, such as the magnetic ground state of pristine compounds and the superconductivity induced by chemical doping or external pressure, they have attracted lots of interest from many researchers in the condensed matter physics. The spin-fluctuation-mediated pairing mechanism and multi-band nature of the Fe-based superconductors are predicted the result of the  $s_{\pm}$ -wave gap symmetry, which is rather unique among the reported superconductors.

Among the Fe-based superconductors, LiFeAs and NaFeAs, so called 111 systems, are exceptional due to their intriguing ground states. At the ambient condition, LiFeAs is known to be a clean limit bulk superconductor without any structural and magnetic transitions while NaFeAs has the coexisting phases of the

spin-density-wave ground states and the superconductivity. These unusual ground states will provide better chances to investigate the superconductivity and the phase competition of the Fe-based superconductors.

In this thesis, high quality single crystals of LiFeAs and NaFeAs are successfully grown by the flux methods and the crystals with various doping are also prepared to investigate the superconductivity of the 111 systems.

At first, the physical properties of the LiFeAs single crystals are investigated. The bulk superconductivity of LiFeAs is examined by the means of the magnetic susceptibility and the specific heat. The upper critical fields,  $H_{c2}$ , near the transition temperature are measured and their anisotropy evidences the electron-electron correlation in the system. The initial slope of the upper critical fields, in addition, imply the LiFeAs is a clean limit superconductor.

The doping dependence is also investigated in the Li(Fe<sub>1-x</sub>Co<sub>x</sub>)As and Li(Fe<sub>1-x</sub>Mn<sub>x</sub>)As series. The Fermi liquid temperature dependence is found in the resistivity of the Li(Fe<sub>1-x</sub>Co<sub>x</sub>)As series, and the increase of the Fermi liquid  $T^2$  coefficient indicates the Fermi energy level shift induced by the Co doping with additional electron carriers. The magnetization curves of the Li(Fe<sub>1-x</sub>Mn<sub>x</sub>)As series indicate that the Mn content introduces local magnetic moments into the system. The suppression of the superconductivity, moreover, by the Mn content is much stronger than one of the Co and Cu content. This result supports the  $s_{\pm}$ -wave gap symmetry and the spin-fluctuation-mediated pairing mechanism of the superconductivity of the LiFeAs system.

At last, the complete phase diagram of the (Na<sub>1-x</sub>Li<sub>x</sub>)FeAs series is realized by the means of the magnetic susceptibility, the electrical resistivity, and the Hall effect measurements. The spin-density-wave ground states is suppressed by the Li

substitution, and the superconductivity arises from the phase competition. The superconducting gap structure, furthermore, of the optimal  $(\text{Na}_{0.95}\text{Li}_{0.05})\text{FeAs}$  is investigated. Both results of the lower critical fields and the specific heat measurements indicate that a small gap of  $\sim 0.5$  meV is dominant in the system within the analysis based on the 2-gap model. The underlying nature of the isovalent Li substitution effect resulting the development of the superconductivity in the phase space and the small-gap-dominant superconducting gap structure is discussed.

**Keywords: Fe-based superconductor, single crystal growth, phase diagram, impurity effect, phase competition, superconducting gap.**

**Student Number: 2008-20445**

# Contents

|   |       |               |
|---|-------|---------------|
| <b>Abstract</b>   | ..... | <b>i</b>      |
| <b>List of Figures</b>                                  | ..... | <b>viii</b>   |
| <b>1. Introduction</b>                                  | ..... | <b>- 1 -</b>  |
| 1.1. Brief review of superconductivity                  | ..... | - 1 -         |
| 1.2. Fe-based superconductors                           | ..... | - 4 -         |
| 1.3. $AFeAs$ system ( $A = Li, Na$ )                    | ..... | - 7 -         |
| 1.4. References   | ..... | - 12 -        |
| <b>2. Theory</b>  | ..... | <b>- 15 -</b> |
| 2.1. Superconducting gap                                | ..... | - 15 -        |
| 2.1.1. 2-gap model of electronic specific heat          | ..... | - 17 -        |
| 2.1.2. 2-gap model of lower critical fields             | ..... | - 20 -        |
| 2.2. 2-band model of magneto-resistance and Hall effect | ...   | - 24 -        |
| 2.3. References   | ..... | - 28 -        |
| <b>3. Experimental method</b>                           | ..... | <b>- 29 -</b> |
| 3.1. Single crystal growth                              | ..... | - 29 -        |
| 3.1.1. Sn-flux method                                   | ..... | - 29 -        |
| 3.1.2. Self-flux method                                 | ..... | - 32 -        |
| 3.2. Preparation for various measurements               | ..... | - 35 -        |
| 3.2.1. X-ray diffraction                                | ..... | - 35 -        |

|  |       |               |
|--|-------|---------------|
| 3.2.2. Composition measurement   | ..... | - 37 -        |
| 3.2.3. Magnetic property   | ..... | - 38 -        |
| 3.2.4. Electronic property   | ..... | - 39 -        |
| 3.2.5. Specific heat   | ..... | - 40 -        |
| 3.3. References  | ..... | - 41 -        |
| <b>4. Superconducting properties of LiFeAs</b>                             | ..... | <b>- 43 -</b> |
| 4.1. Introduction  | ..... | - 43 -        |
| 4.2. High quality single crystal   | ..... | - 45 -        |
| 4.3. Anisotropy of the upper critical fields                               | ..... | - 51 -        |
| 4.4. Superconductivity in a clean-limit                                    | ..... | - 54 -        |
| 4.5. Summary   | ..... | - 57 -        |
| 4.6. References  | ..... | - 58 -        |
| <b>5. Fermi energy level shift in Li(Fe<sub>1-x</sub>Co<sub>x</sub>)As</b> | ..... | <b>- 60 -</b> |
| 5.1. Introduction  | ..... | - 60 -        |
| 5.2. X-ray diffraction   | ..... | - 62 -        |
| 5.3. Doping dependence of RRR and $T_c$                                    | ..... | - 63 -        |
| 5.4. Fermi liquid behavior and the increase of $A$                         | ..... | - 68 -        |
| 5.5. Summary   | ..... | - 74 -        |
| 5.6. References  | ..... | - 75 -        |
| <b>6. Impurity effects in Li(Fe<sub>1-x</sub>Mn<sub>x</sub>)As</b>         | ..... | <b>- 77 -</b> |
| 6.1. Introduction  | ..... | - 77 -        |
| 6.2. Structural and compositional properties                               | ..... | - 80 -        |

|           |  |       |                |
|-----------|--|-------|----------------|
| 6.3.      | Superconducting transition temperature   | ..... | - 82 -         |
| 6.4.      | Curie-Weiss behavior and local magnetic moments                                  | ..... | - 85 -         |
| 6.5.      | Electrical resistivity and impurity scattering                                   | ..... | - 88 -         |
| 6.6.      | Suppression rate of $T_c$ and impurity effects                                   | ..... | - 92 -         |
| 6.7.      | Summary  | ..... | - 98 -         |
| 6.8.      | References   | ..... | - 98 -         |
| <b>7.</b> | <b>Phase competition in <math>(\text{Na}_{1-x}\text{Li}_x)\text{FeAs}</math></b> | ..... | <b>- 100 -</b> |
| 7.1.      | Introduction   | ..... | - 100 -        |
| 7.2.      | Structure, composition, and crystallinity  | ..... | - 102 -        |
| 7.3.      | Development of the superconductivity   | ..... | - 105 -        |
| 7.4.      | Suppression of the spin-density-wave transition                                  | ..... | - 107 -        |
| 7.5.      | Complete phase diagram   | ..... | - 112 -        |
| 7.6.      | Signature of disorder  | ..... | - 114 -        |
| 7.7.      | $H_{c1}$ and $C_p$ of $(\text{Na}_{0.95}\text{Li}_{0.05})\text{FeAs}$            | ..... | - 117 -        |
| 7.8.      | Small-gap-dominant superconductivity   | ..... | - 123 -        |
| 7.9.      | Summary  | ..... | - 125 -        |
| 7.10.     | References   | ..... | - 125 -        |
| <b>8.</b> | <b>Conclusion</b>  | ..... | <b>- 127 -</b> |
|           | <b>List of Publications</b>  | ..... | <b>- 130 -</b> |
|           | <b>Appendix A. Manual for the arc melting chamber</b>                            | ..... | <b>- 133 -</b> |
|           | <b>Appendix B. Service manual for the glove box</b>                              | ..... | <b>- 138 -</b> |

|  |               |
|--|---------------|
| <b>Appendix C. Capillary preparation for XRD</b> | ..... - 141 - |
| <b>Appendix D. Drawings and designs</b>          | ..... - 145 - |
| <b>Appendix E. Mathematica codes</b>             | ..... - 153 - |
| <b>국문 초록</b>                                     | ..... - 158 - |

## List of Figures

- Figure 1.1. The optimal superconducting transition temperature of several (a) hole-doped and (b) electron-doped 122 systems with respect to the optimal doping level  $x$ . ..... - 5 -
- Figure 1.2. The optimal superconducting transition temperature of several isovalent-doped 122 systems and  $(\text{Na}_{1-x}\text{Li}_x)\text{FeAs}$  series with respect to the optimal doping level  $x$ . Ones of the pristine and superconducting compounds such as  $\text{KFe}_2\text{As}_2$ ,  $\text{LiFeP}$ ,  $\text{LiFeAs}$  and  $\text{NaFeAs}$  are presented together. .... - 8 -
- Figure 2.1. The temperature dependence of the superconducting energy gap. .... - 16 -
- Figure 2.2. The temperature dependence of electronic specific heat calculated with the  $\alpha$  model. .... - 19 -
- Figure 2.3. The temperature dependence of lower critical fields calculated with the  $\alpha$  model. .... - 22 -
- Figure 3.1. Binary alloy phase diagram of (a) Li-Sn, (b) As-Fe, (c) As-Sn, and (d) Fe-Sn. .... - 31 -
- Figure 3.2. Temperature dependent vapor pressure curves for As, Li, and Na. .... - 33 -
- Figure 4.1. X-ray diffraction pattern of the  $\text{LiFeAs}$  single crystal piece aligned along the (001) plane. .... - 45 -

|   |        |
|---|--------|
| Figure 4.2. Temperature dependence of (a) the resistivity and (b) the magnetic susceptibility with applied magnetic fields of 9 T along <i>ab</i> -plane.   | - 46 - |
| Figure 4.3. (a) DC magnetic susceptibility measured with $H$ of $\sim 10$ Oe applied along the <i>ab</i> -plane at the zero-field-cooled and field-cooled condition. (b) The specific heat of the LiFeAs crystals at zero magnetic fields. (c) The difference of specific heat between the normal and superconducting states. | - 49 - |
| Figure 4.4. The resistivity measured under (a) $H//ab$ -plane and (b) $H//c$ -axis.   | - 50 - |
| Figure 4.5. The $H_{c2}$ curves for both magnetic field directions.   | - 52 - |
| Figure 4.6. The $H_{c2}$ anisotropy near $T_c$ .  | - 53 - |
| Figure 4.7. $T_c$ realized from the resistivity of crystals with various $\rho_0$ prepared from the modified growth conditions.   | - 55 - |
| Figure 4.8. The slope of $H_{c2}$ near $T_c$ for the crystals with various $\rho_0$ .   | - 56 - |
| Figure 5.1. X-ray diffraction pattern of the powder obtained from the Li(Fe <sub>0.9</sub> Co <sub>0.1</sub> )As single crystals.   | - 62 - |
| Figure 5.2. The temperature dependence of (a) the resistivity and (b) the normalized resistivity of the Li(Fe <sub>1-x</sub> Co <sub>x</sub> )As single crystals.   | - 64 - |
| Figure 5.3. Extracted $\rho_0$ and RRR with respect to $x$ .  | - 65 - |

|   |        |
|---|--------|
| Figure 5.4. Doping dependence of $T_c$ of the $\text{Li}(\text{Fe}_{1-x}\text{Co}_x)\text{As}$ single crystals.   | - 66 - |
| Figure 5.5. The $T^2$ dependence of the resistivity curves.   | - 70 - |
| Figure 5.6. Doping dependence of the coefficient $A$ , estimated from the fitting explained in the text.  | - 71 - |
| Figure 5.7. The partial density of states near the Fermi energy level calculated for the 3 hole-bands of $\text{LiFeAs}$ .  | - 73 - |
| Figure 6.1. Powder x-ray diffraction patterns of the $\text{Li}(\text{Fe}_{1-x}\text{Mn}_x)\text{As}$ single crystals. The patterns of (a) $x = 0.000$ , (b) $x = 0.012$ , (c) $x = 0.025$ , and (d) $x = 0.030$ are presented.   | - 81 - |
| Figure 6.2. The lattice constants (a) $a$ and (b) $c$ of the $\text{Li}(\text{Fe}_{1-x}\text{Mn}_x)\text{As}$ series.   | - 82 - |
| Figure 6.3. The magnetic volume susceptibility of the (a) $\text{Li}(\text{Fe}_{1-x}\text{Mn}_x)\text{As}$ and (b) $\text{Li}(\text{Fe}_{1-x}\text{Co}_x)\text{As}$ series measured under the zero-field-cooled condition with the magnetic fields of $\sim 10$ Oe along the $ab$ -plane. | - 83 - |
| Figure 6.4. The doping dependence of $T_c$ for the $\text{Li}(\text{Fe}_{1-x}\text{Mn}_x)\text{As}$ and $\text{Li}(\text{Fe}_{1-x}\text{Co}_x)\text{As}$ series.  | - 84 - |
| Figure 6.5. The temperature dependent DC magnetization curves of the (a) $\text{Li}(\text{Fe}_{1-x}\text{Mn}_x)\text{As}$ and (b) $\text{Li}(\text{Fe}_{1-x}\text{Co}_x)\text{As}$ series measured with the magnetic fields of $\sim 30000$ Oe applied along the $ab$ -plane.             | - 86 - |
| Figure 6.6. The Curie-Weiss coefficients of the $\text{Li}(\text{Fe}_{1-x}\text{Mn}_x)\text{As}$ series realized from   |        |

|  |               |
|--|---------------|
| the fitting described in the text.   | ..... - 88 -  |
| Figure 6.7. The temperature dependent electrical resistivity curves of the (a) $\text{Li}(\text{Fe}_{1-x}\text{Mn}_x)\text{As}$ and (b) $\text{Li}(\text{Fe}_{1-x}\text{Co}_x)\text{As}$ series.                                 | ..... - 89 -  |
| Figure 6.8. The $T^2$ dependence of the resistivity of the $\text{Li}(\text{Fe}_{1-x}\text{Mn}_x)\text{As}$ series.  | ..... - 90 -  |
| Figure 6.9. The doping dependence of the residual resistivity and RRR realized from the fitting for the resistivity of the $\text{Li}(\text{Fe}_{1-x}\text{Mn}_x)\text{As}$ series.  | ..... - 91 -  |
| Figure 6.10. The normalized transition temperature of the $\text{Li}(\text{Fe}_{1-x}\text{M}_x)\text{As}$ series with respect to the doping level.   | ..... - 94 -  |
| Figure 6.11. (a) The total and (b) electronic specific heat of the $\text{LiFeAs}$ single crystals.  | ..... - 96 -  |
| Figure 7.1. Powder x-ray diffraction pattern of the $(\text{Na}_{0.95}\text{Li}_{0.05})\text{FeAs}$ single crystals.   | ..... - 103 - |
| Figure 7.2. The DC volume magnetic susceptibility of the $(\text{Na}_{1-x}\text{Li}_x)\text{FeAs}$ series measured under the zero-field-cooled condition with the magnetic fields of $\sim 10$ Oe applied along the $ab$ -plane. | ..... - 105 - |
| Figure 7.3. The doping dependence of the transition temperature and the superconducting shielding fraction of the $(\text{Na}_{1-x}\text{Li}_x)\text{FeAs}$ series.  | ..... - 106 - |
| Figure 7.4. The electrical resistivity of the $(\text{Na}_{1-x}\text{Li}_x)\text{FeAs}$ series for (a) the low doping region with $0.00 \leq x \leq 0.05$ and (b) the high doping region with                                    |               |

|   |               |
|---|---------------|
| 0.05 $\leq$ x $\leq$ 0.12.  | ..... - 108 - |
| Figure 7.5. The temperature dependent magnetization curves of (a) NaFeAs, (b) (Na <sub>0.99</sub> Li <sub>0.01</sub> )FeAs, and (c) (Na <sub>0.98</sub> Li <sub>0.02</sub> )FeAs.   | ..... - 109 - |
| Figure 7.6. (a)-(c) The magnetization, (d)-(f) the 1st derivative of the resistivity, and (g)-(i) the Hall coefficient of the low doping crystals. The data of NaFeAs in (a), (d), (g), (Na <sub>0.99</sub> Li <sub>0.01</sub> )FeAs in (b), (e), (h), and (Na <sub>0.98</sub> Li <sub>0.02</sub> )FeAs in (c), (f), (i) are shown. | ..... - 111 - |
| Figure 7.7. The phase diagram of the (Na <sub>1-x</sub> Li <sub>x</sub> )FeAs series.   | ..... - 113 - |
| Figure 7.8. The resistivity normalized with the room temperature resistivity of the (Na <sub>1-x</sub> Li <sub>x</sub> )FeAs series.  | ..... - 115 - |
| Figure 7.9. The transition width in the resistivity of the (Na <sub>1-x</sub> Li <sub>x</sub> )FeAs series.   | ..... - 116 - |
| Figure 7.10. (a) The magnetic field dependence of magnetization of the (Na <sub>0.95</sub> Li <sub>0.05</sub> )FeAs single crystal measured at specific temperature and (b) the difference from the Meissner line.  | ..... - 118 - |
| Figure 7.11. The lower critical fields of the (Na <sub>0.95</sub> Li <sub>0.05</sub> )FeAs single crystal.  | ..... - 120 - |
| Figure 7.12. (a) The total and (b) electronic specific heat of the (Na <sub>0.95</sub> Li <sub>0.05</sub> )FeAs single crystals.  | ..... - 122 - |
| Figure A.1. Photograph of the arc melting chamber. (a) Overall equipment, (b) inside of the chamber, (c) the handle, and (d) the touchscreen panel.   | ..... - 134 - |

Figure C.1. Photograph of (a) the capillaries in the bottle, (b) a holder with a hole made of a paper cup, (c) the capillary loaded in the Cu adaptor, and (d) the spinning capillary stage. .... - 142 -

Figure D.1. The drawings of the specific heat probe for CCR. (a) The radiation cap and (b) the bottom ring. .... - 145 -

Figure D.2. The photographs of the specific heat probe attached on CCR. (a) The platform and the ring without the cap and (b) the capped probe. .... - 146 -

Figure D.3. The drawings of (a) the inner bottom, (b) the outer bottom, and (c) the spacer noted in (d) the schematic figure of the  $^3\text{He}$  cryostat. .... - 147 -

Figure D.4. The drawings of (a) the sample platform, (b) the radiation cap, and (c) the fitting for the electrical feedthroughs of the magneto-caloric effect probe. .... - 149 -

Figure D.5. The photograph of (a) the assembled probe, (b) the sample platform with the radiation cap, and (c) the sample loaded on the platform with the temperature sensor. .... - 150 -

Figure D.6. (a) The drawings of the vacuum cap and the sample platform and (b) the schematic figure of the platform of the In-sealed vacuum dipstick. .... - 151 -



# **1. Introduction**

## **1.1. Brief review of superconductivity**

Since the superconductivity was discovered in mercury of the transition temperature of 4.2 K [1], it has been one of the most fascinating phenomena in the condensed matter physics. The superconductivity accompanies perfect electrical conductivity and perfect diamagnetism, but these exotic phenomena are not explained by a picture of a simple perfect conductor. The Meissner effect, the expelling external magnetic fields regardless of the cooling condition, therefore, is an important key to realize the superconductivity. The superconducting phase transition is known to be 2nd order phase transition without any external magnetic fields. Besides the Meissner effect, many other exotic phenomena occur with the superconductivity, such as the breaking of the superconductivity by the thermodynamic critical magnetic fields, the magnetic flux quantization in the superconductor and the flux vortex, so called the Abrikosov vortex, penetration.

To understand and describe the superconductivity itself and also accompanying many other exotic phenomena, lots of theoretical approaches had been proposed. The London equations, for instance, were proposed to describe microscopic electric and magnetic fields as well as electrodynamic properties of superconductors [2]. The London penetration depth was introduced as a phenomenological parameter with these equations, which is revealed to be a characteristic length of the exponential screening of the external magnetic fields from the surface of a superconductor. The Ginzburg-Landau theory was another theory proposed to describe the 2nd order phase transition of the superconductivity [3]. They introduced an arbitrary order

parameter of the superconductivity, which eventually was known to be same with the number density of superconducting electrons introduced in the London equations. Based on the Ginzburg-Landau theory, many macroscopic properties such as critical fields and other important characteristic parameters were introduced. So called, the GL coherence length implies the distance between superconducting electrons, which would be revealed the characteristic length of the Cooper pair later. The Ginzburg-Landau ratio between 2 characteristic lengths, the penetration depth and the coherence length, was also named as the Ginzburg-Landau parameter and used as a scale to determine whether a superconductor is the type-I or type-II superconductor, which doesn't allow to penetrate any flux vortex or allows to penetrate the vortex inside the superconductor, respectively.

Most striking and important theory, however, is the famous BCS theory, named after J. Bardeen, L. N. Cooper, and J. R. Schrieffer [4]. It is the first theory describing the microscopic mechanism of superconductivity successfully. In the BCS theory, existence of some attractive interaction between electrons is assumed. By solving the Hamiltonian, it is proved that the attractive interaction makes electrons correlated and forming a pair of bound electrons, so called the Cooper pair, and the pair condensates into a bosonic state. This microscopic theory has been very successful to reproduce and explain many experimental phenomena including the Meissner effect, the isotope effect on transition temperature, and the energy gap at the Fermi energy level. The isotope effect evidenced that the lattice vibrations, or the phonon modes, are strongly related to the pairing mechanism, and it was eventually revealed the attractive interaction causing the pairing of electrons is mediated by the phonon in most superconductors. The superconducting energy gap is also very important in the BCS theory. The superconducting gap is opened due to the bosonic character of

the Cooper pair and results, paradoxically, the perfect conduction. And the temperature dependence of the gap induces many physical properties showing strange behavior such as the exponential increase of the electronic specific heat near the transition temperature.

The BCS theory has been triumphant to depict the superconductivity and related phenomena, but could not fully explain several newly-discovered superconductors. MgB<sub>2</sub>, for example, is believed to be a conventional phonon-mediated superconductor which has an exceptionally high transition temperature of 39 K [5]. This exotic superconductivity was simply beyond the limit of the BCS theory, the assumption that all electrons act in same way. Later on, it was revealed that the multiple bands with very different characters, resulting the multiple gaps with larger and smaller sizes, lead to the unpredicted phenomena. Another, and very important, example is the high  $T_c$  cuprate superconductors. After the first discovery of the superconductivity in the compound with the Cu-O layer [6], many compounds sharing the common Cu-O layer in their structures were turned out to be superconducting and the transition temperature became higher even up to 133 K at the ambient condition [7]. Intensive and comprehensive investigation about the superconductivity of cuprates with incredibly high transition temperature revealed that the spin fluctuations in the compounds substitute for the phonon which is the pairing glue of the Cooper pair and this spin-fluctuation-mediated superconductivity is the underlying nature of the high transition temperature and other exotic superconducting properties such as the anisotropic *d*-wave gap symmetry. Hence, the superconductivity mediated by the spin fluctuations is called unconventional while the phonon-mediated one is conventional. These exotic superconductors demanded more than the conventional BCS theory to be described, therefore the

extended theories such as the multi-gap model and the unconventional pairing mechanism with the unconventional gap structure have been included until nowadays.

## 1.2. Fe-based superconductors

Fe-based superconductors are unconventional superconductors found recently. At the early 2008, the  $\text{La}(\text{O}_{1-x}\text{F}_x)\text{FeAs}$  series were reported to be superconducting with the transition temperature of 26 K at the optimal doping level [8]. After the discovery, many other Fe-containing compounds have been turned out to be superconductors. The superconducting compounds are categorized according to the lattice structure and the chemical composition. For example,  $\text{LnOFeAs}$  structure ( $\text{Ln}$ : lanthanide),  $\text{AeFe}_2\text{As}_2$  structure ( $\text{Ae}$ : alkaline earth metal),  $\text{AFeAs}$  structure ( $\text{A}$ : alkali metal), and  $\text{FeCh}$  structure ( $\text{Ch}$ : chalcogen), as known as 1111, 122, 111, and 11 systems respectively, represent the categorized compounds [9]. All these representative structures of the Fe-based superconductors share a common component of the Fe-As tetrahedral layer. The lattice structure of the Fe-based superconductors consists of the Fe-As tetrahedral layer and the layer of other ions, which is known to be the charge reservoir layer, stacked along the crystallographic  $c$ -axis. Only the 11 systems don't include the charge reservoir layer, but their Fe- $\text{Ch}$  layer is also isostructural with the Fe-As layer of other systems. This common structural character of entire family is quite similar to one of the high  $T_c$  cuprate superconductors since the cuprates also share the common Cu-O layer.

Another similarity between the Fe-based superconductors and the cuprates is the general phase diagram based on the chemical doping or external pressure dependence. The pristine compounds of most Fe-based superconductor family are

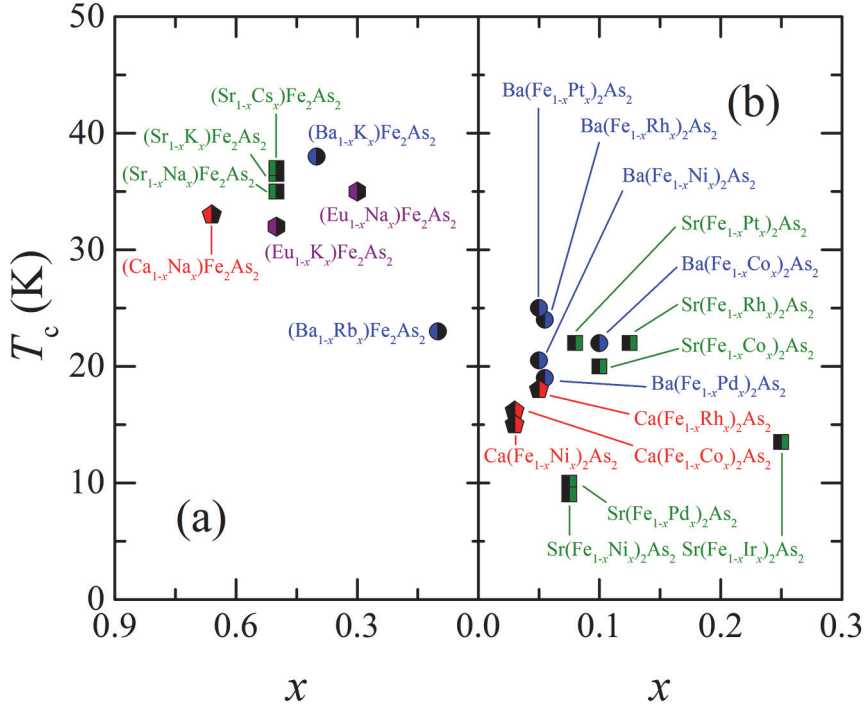


**Figure 1.1. The optimal superconducting transition temperature of several (a) hole-doped and (b) electron-doped 122 systems with respect to the optimal doping level  $x$  [9]. Blue circles, green squares, red pentagons, and purple hexagons represent the  $\text{BaFe}_2\text{As}_2$ ,  $\text{SrFe}_2\text{As}_2$ ,  $\text{CaFe}_2\text{As}_2$ , and  $\text{EuFe}_2\text{As}_2$ -based systems, respectively.**

known to have an antiferromagnetic spin-density-wave ground state. They exhibits a structural phase transition from high temperature tetragonal phase to low temperature orthorhombic phase, and a spin-density-wave transition is observed at the temperature slightly lower than the structural transition temperature. The superconductivity is not found in most pristine compounds. The structural and magnetic transitions, however, is suppressed by means of chemical doping or external pressure, and the superconductivity arises in the vicinity of phase space

where the spin-density-wave ground states is fully suppressed and disappeared. The evolution of the superconductivity with the coexistent antiferromagnetic order seems very alike with the general phase diagram of the cuprate superconductors. The spin fluctuations, therefore, are suspected to mediate the pairing in the Fe-based superconductors.

The pairing mechanism with the spin fluctuations results the unconventional superconducting gap structure of the Fe-based superconductors. It was proposed at the very beginning that the spin-fluctuations mediate the superconducting pairing in the Fe-based family, and a sign reversal in the order parameter was predicted as well [10, 11]. The predicted superconducting gap structure with the sign reversal, so called the  $s_{\pm}$ -wave gap symmetry, consists of multiple isotropic  $s$ -wave gaps whose phases are opposite to each other's. According to many experimental results reported until nowadays, most of the Fe-based superconductors have nearly-isotropic energy gaps without any nodal feature on the hole- and electron-bands near the  $\Gamma$ - and  $M$ -points, respectively, in the momentum space [12-16], implying the  $s_{\pm}$ -wave gap symmetry as predicted. This gap symmetry is somewhat similar with but rather different from the  $d$ -wave symmetry of the cuprate superconductors. The origins of the unconventional gap symmetry are expected to be same as the spin-fluctuation-mediated pairing mechanism in both the Fe-based and cuprate family. However, the Fe-based superconductors have clearly multiple gaps without any nodal feature while the gap of the cuprates is well described within the single gap model with clear nodes due to the  $d$ -wave symmetry. These unique characteristics of the Fe-based superconductors have attracted lots of researchers' interests.

As mentioned above, many experimental studies support the  $s_{\pm}$ -wave gap symmetry of the Fe-based superconductors due to the spin-fluctuation-mediated

pairing mechanism. Nevertheless, there still exist some debates about the other exotic superconducting gap structure. A couple of compounds such as  $\text{KFe}_2\text{As}_2$ ,  $\text{BaFe}_2(\text{As}_{1-x}\text{P}_x)_2$ , and  $\text{LiFeP}$ , for example, have been reported to have some nodes on their superconducting energy gaps [17-19], which is inconsistent with the simple  $s_{\pm}$ -wave gap symmetry picture. Furthermore, the possibility of the  $s_{++}$ -wave gap symmetry is still arguable since the electronic nematicity is observed in many specimens including  $\text{Ca}(\text{Fe}_{1-x}\text{Co}_x)_2\text{As}_2$ ,  $\text{BaFe}_2(\text{As}_{1-x}\text{P}_x)_2$ ,  $\text{NaFeAs}$ , and  $\text{FeSe}$  [20-23]. The early theoretical investigation suggested that the sign-preserving  $s_{++}$ -wave gap symmetry, which means that the all superconducting gaps have same sign, is more preferable than the sign-changing  $s_{\pm}$ -wave gap symmetry in the Fe-based family and the superconducting gaps would have the  $s_{++}$ -wave symmetry if the charge fluctuations mediate the pairing instead of the spin fluctuations [24]. Since the electronic nematicity is closely related to the orbital ordering and the nematic, or orbital, ordering is known to have very similar doping and pressure dependence with the magnetic ordering, one needs to consider the  $s_{++}$ -wave symmetry as well as the  $s_{\pm}$ -wave one for the Fe-based superconductors. For these unexpected exotic gap structures, many theoretical attempts to describe the superconductivity of the Fe-based family [25]. In addition to the theoretical investigation, further experimental investigations are necessary to examine the superconducting gap structure, moreover the pairing mechanism of the Fe-based superconductors.

### 1.3. $A\text{FeAs}$ system ( $A = \text{Li, Na}$ )

$\text{LiFeAs}$  and  $\text{NaFeAs}$ , representative compounds of the 111 system, are very unique among the Fe-based superconductor family. The superconductivity of  $\text{LiFeAs}$  was reported at 2008 with the transition temperature of  $\sim 18$  K at the ambient

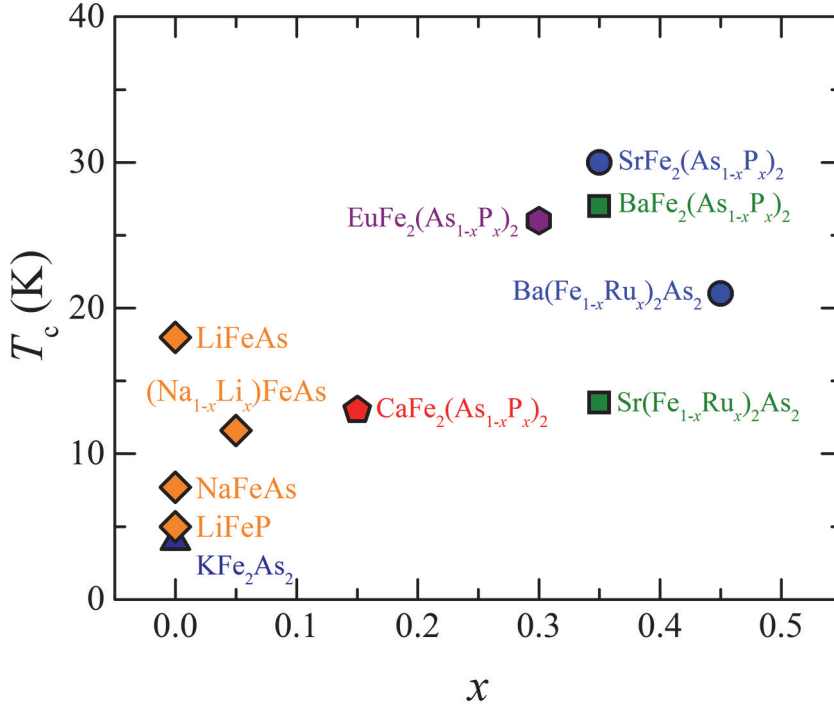


**Figure 1.2. The optimal superconducting transition temperature of several iso-valent-doped 122 systems and (Na<sub>1-x</sub>Li<sub>x</sub>)FeAs series with respect to the optimal doping level  $x$  [9]. Ones of the pristine and superconducting compounds such as KFe<sub>2</sub>As<sub>2</sub>, LiFeP, LiFeAs and NaFeAs are presented together [9]. The doping level of the pristine compounds is assumed as zero. Blue circles, green squares, red pentagons, and purple hexagons represent the BaFe<sub>2</sub>As<sub>2</sub>, SrFe<sub>2</sub>As<sub>2</sub>, CaFe<sub>2</sub>As<sub>2</sub>, and EuFe<sub>2</sub>As<sub>2</sub>-based systems, respectively, while navy triangle and orange diamonds represents KFe<sub>2</sub>As<sub>2</sub> and the 111 systems.**

condition, while any signature of structural or magnetic transitions was not found [26-28]. NaFeAs was also reported to be superconducting at 2009, but the structural and magnetic phase transitions were rather remarkable [29]. The antiferromagnetic ordering observed in the polycrystalline specimen implies the coexistence of the

superconductivity and the spin-density-wave state in NaFeAs at the ambient environment. Since most pristine compounds of the Fe-based superconductor family have the spin-density-wave ground state, the superconducting ground state with the transition temperature higher than 10 K of LiFeAs the coexistence of the spin-density-wave transition and the superconductivity in NaFeAs are exceptional. These unexpected ground states of the 111 systems are expected to provide better opportunities to investigate the superconductivity itself and also the related phases.

The absence of the other transitions makes LiFeAs a perfect candidate to study its superconductivity. Most of the superconducting ground states in the Fe-based superconductors are achieved within the presence of chemical substitution or external pressure. The chemical substitution results the superconductivity but also introduces the disorder into the system, which disturb to investigate the underlying nature by the means of macroscopic properties. The complicated experiments are, of course, very difficult to be performed under the external pressure. The bulk superconductivity at the ambient condition, therefore, is very helpful for the experimental examination of itself. Although there are several superconducting compounds in the Fe-based family, LiFeAs has advantages of higher transition temperature and cleaner electronic properties.  $\text{KFe}_2\text{As}_2$ , for example, is known to be superconducting with extremely high residual resistivity ratio to the room temperature resistivity (RRR) of  $\sim 1280$  but its transition temperature is relatively lower as  $\sim 3$  K [30]. LiFeAs, on the other hand, with the superconducting transition temperature of  $\sim 18$  K, is reported to have also high RRR from 40 to 250 in the crystals grown by the self-flux method [31-33]. In addition, the upper critical fields of the system support that the superconductivity of LiFeAs is rather close to the clean limit [34]. The clean superconductivity and normal state at the ambient condition

provide the unique opportunity to examine the physical properties such as the charge doping effect on the normal state transport properties and the impurity effect on the superconductivity. Even the superconducting gap symmetry and the pairing mechanism, furthermore, is expected to be evidenced by the intensive investigations.

The case of NaFeAs is even more exceptional than one of LiFeAs since any other pristine compound in the Fe-based superconductor family doesn't exhibit all 3 structural, magnetic, and superconducting transitions at the same time. The superconducting fraction of NaFeAs was expected to be less than 20 % while the antiferromagnetic fraction was detected to be  $\sim 90$  % [20]. The angle-resolved photoemission spectroscopy studies, moreover, revealed the absence of the bulk superconducting gap opening even at 6 K [35]. The spin-density-wave transition is suppressed by the chemical substitution such as the Co-doping in the  $\text{Na}(\text{Fe}_{1-x}\text{Co}_x)\text{As}$  series similar to the other Fe-based superconductors [36], and the magnetic state and the superconductivity are observed to coexist microscopically and to compete against each other in the scanning tunneling spectroscopy of the under-doped specimens [37]. The phase competition in the Fe-based superconductor family has been a fascinating subject for the both experimentalists and theoreticians. In that sense, it is worth to study about the NaFeAs and related compounds by the means of, for example, chemical substitution to control the phase competition between the spin-density-wave state and the superconductivity.

Experimental investigations about LiFeAs and NaFeAs, however, have been impeded by several technical difficulties. First of all, it has been very difficult to grow high quality single crystals of the 111 systems. Alkali metals including Li and Na are well known to be very sensitive to the oxygen and moisture. The high reactivity of Li and Na even causes the reaction with the quartz, which is generally

used for the intermetallic sample growth, when it is contacted with the liquid or vapor of Li and Na. The aluminum oxide, so called alumina, crucible also can be degraded by the contact with the Li liquid because of the high reactivity of Li. The melting points of Li and Na are  $\sim 180$  and  $\sim 98$  °C, respectively, which are much lower than ones of Fe and As. These lower melting points give rise to the handling problem for Li and Na. In addition to the low melting point, the vapor pressure of Na is relatively higher than other elements. Due to the high volatility and the high reactivity of Na, the quartz parts should be excluded from the growth of Na-containing compounds. The fastidiousness of Li and Na is not limited on the pure elements. The resultant LiFeAs and NaFeAs crystals are also very sensitive to the air and moisture. Complicated and special preparations, therefore, should be considered for the single crystal growth and also various physical property measurements.

In this thesis, it is reported that the single crystals of LiFeAs, NaFeAs, and related compounds are successfully grown by the flux methods which are carefully designed. In chapter 4, the physical and superconducting properties of LiFeAs single crystals grown by the Sn-flux method are discussed. It was the very first single crystals of LiFeAs at 2010 [38]. The superconducting transition is observed in electrical resistivity, magnetic susceptibility, and specific heat, indicating the bulk superconductivity. Further investigation of the upper critical fields near the transition evidences the electron-electron correlation in the system and the clean-limit superconductivity. In chapter 5, transport properties of Co-doped  $\text{Li}(\text{Fe}_{1-x}\text{Co}_x)\text{As}$  series [39]. The gradual increase of RRR with the increase of the Co content implies the less influence of spin scattering in the transport. The crystals show the Fermi liquid behavior at low temperature and the sudden increase of the  $T^2$  coefficient is found, which is expected to evidence the Fermi energy level shift induced by the

introduction of additional electron carrier by Co doping. In chapter 6, the doping dependence of  $\text{Li}(\text{Fe}_{1-x}\text{Mn}_x)\text{As}$  series is presented. The Mn content introduces local magnetic moments and act as an impurity in the system. Based on the comparison with other non-magnetic impurities, the suppression of the transition temperature by the Mn content is clearly faster than ones by others. This strong suppression is very consistent with the previous theoretical prediction about the impurity effect on the  $s\pm$ -wave gap symmetry, supporting the spin-fluctuation-mediated superconductivity of the Fe-based superconductor family. In chapter 7, a phase diagram of single-crystalline  $(\text{Na}_{1-x}\text{Li}_x)\text{FeAs}$  series is discussed. The suppression of the spin-density-wave state and the evolution of the superconductivity are shown. The disorder induced by the Li substitution in the charge reservoir layer seems to be the cause. In addition, the gap structure of the optimal  $(\text{Na}_{0.95}\text{Li}_{0.05})\text{FeAs}$  crystals is investigated by the means of lower critical fields and specific heat. Based on the experimental results, the small-gap-dominant structure is expected.

#### 1.4. References

- [1] H. K. Onnes, Commun. Phys. Lab. Univ. Leiden **12**, 120 (1911)
- [2] F. London and H. London, Proc. R. Soc. A **149**, 71 (1935)
- [3] V. L. Ginzburg and L. D. Landau, J. Exp. Theor. Phys. **20**, 1064 (1950)
- [4] J. Bardeen *et al.*, Phys. Rev. **108**, 1175 (1957)
- [5] J. Nagamatsu *et al.*, Nature **410**, 63 (2001)
- [6] J. G. Bednorz and K. A. Muller, Z. Phys. B - Condens. Matter **64**, 189 (1986)
- [7] A. Schilling *et al.*, Nature **363**, 56 (1993)
- [8] Y. Kamihara *et al.*, J. Am. Chem. Soc. **130**, 3296 (2008)
- [9] G. R. Stewart, Rev. Mod. Phys. **83**, 1589 (2011)

- [10] I. I. Mazin *et al.*, Phys. Rev. Lett. **101**, 057003 (2008)
- [11] K. Kuroki *et al.*, Phys. Rev. Lett. **101**, 087004 (2008)
- [12] H. Ding *et al.*, Europhys. Lett. **83**, 47001 (2008)
- [13] K. Gofryk *et al.*, Phys. Rev. B **83**, 064513 (2011)
- [14] T. Hanaguri *et al.*, Science **328**, 474 (2010)
- [15] U. Stockert *et al.*, Phys. Rev. B **83**, 224512 (2011)
- [16] D.-J. Jang *et al.*, Phys. Rev. B **85**, 180505 (2012)
- [17] J. K. Dong *et al.*, Phys. Rev. Lett. **104**, 087005 (2010)
- [18] K. Hashimoto *et al.*, Phys. Rev. B **81**, 220501 (2010)
- [19] K. Hashimoto *et al.*, Phys. Rev. Lett. **108**, 047003 (2012)
- [20] M. P. Allan *et al.*, Nature Phys. **9**, 3544 (2013)
- [21] S. Kasahara *et al.*, Nature **480**, 382 (2012)
- [22] E. P. Rosenthal *et al.*, Nature Phys. **10**, 225 (2014)
- [23] S.-H. Baek *et al.*, Nature Mater. (in press)
- [24] S. Onari and H. Kontani, Phys. Rev. Lett. **103**, 177001 (2009)
- [25] A. Chubukov, Annu. Rev. Condens. Matter Phys. **3**, 57 (2012)
- [26] X. C. Wang *et al.*, Solid State Commun. **148**, 538 (2008)
- [27] J. H. Tapp *et al.*, Phys. Rev. B **78**, 060505 (2008)
- [28] M. J. Pitcher *et al.*, Chem. Commun. **2008**, 5918 (2008)
- [29] D. R. Parker *et al.*, Chem. Commun. **2009**, 2189 (2009)
- [30] K. Hashimoto *et al.*, Phys. Rev. B **82**, 014526 (2010)
- [31] O. Heyer *et al.*, Phys. Rev. B **84**, 064512 (2011)
- [32] S. Kasahara *et al.*, Phys. Rev. B **85**, 060503 (2012)
- [33] F. Rullier-Albenque *et al.*, Phys. Rev. Lett. **109**, 187005 (2012)
- [34] S. Khim *et al.*, Phys. Rev. B **84**, 104502 (2011)

- [35] C. He *et al.*, Phys. Rev. Lett. **105**, 117002 (2010)
- [36] A. F. Wang *et al.*, Phys. Rev. B **85**, 224521 (2012)
- [37] P. Cai *et al.*, Nature Comm. **4**, 1596 (2013)
- [38] B. Lee *et al.*, Europhys. Lett. **91**, 67002 (2010)
- [39] B. Lee *et al.*, Physica C **495**, 130 (2013)

## 2. Theory

### 2.1. Superconducting gap

In the famous BCS theory, it is predicted that even very weak attractive interactions between electrons can form bound pairs of electrons and a minimum energy is required to break these pairs, as known as the Cooper pairs [1]. The minimum energy is known to be  $E_g = 2\Delta_0$  where  $\Delta_0$  is expected to be

$$\Delta_0 \approx 2\hbar\omega_c e^{-\frac{1}{N(0)V}} = \Delta(0)$$

with the reduced Planck constant  $\hbar$ , the critical frequency  $\omega_c$ , the density of states at the Fermi level for electrons of one spin orientation  $N(0)$  and the attractive interaction between electrons  $V$ . The superconducting transition temperature, in addition, is calculated to be

$$k_B T_c = 1.13\hbar\omega_c e^{-\frac{1}{N(0)V}}$$

within the BCS theory. Then the superconducting gap  $\Delta_0$  is realized.

$$\Delta(0) \approx 1.76 \cdot k_B T_c$$

The obtained superconducting gap, however, is only the size at the zero temperature. The temperature dependence of the gap can be computed numerically from the self-consistent equation of

$$\int_0^\infty dE \left[ \frac{\tanh\left(\frac{1}{2}\beta\sqrt{E^2 + \Delta^2}\right)}{\sqrt{E^2 + \Delta^2}} - \frac{1}{E} \tanh\left(\frac{E}{2T_c}\right) \right] = 0$$

or realized from the approximate formula alternatively [2].

$$\Delta(T) = \Delta(0) \tanh \left[ 1.82 \left\{ 1.018 \left( \frac{T_c}{T} - 1 \right) \right\}^{0.51} \right]$$

Figure 2.1 presents a calculated curve of the superconducting gap with respect to the

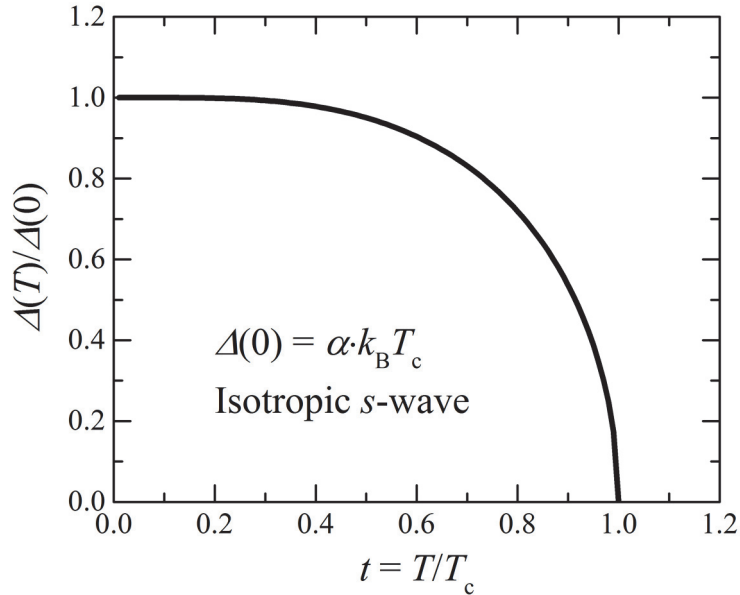


**Figure 2.1.** The temperature dependence of the superconducting energy gap. The approximated formula for the isotropic *s*-wave gap symmetry is used. The gap size normalized with the zero temperature value and the reduced temperature are employed as the axes.

reduced temperature,  $t = T/T_c$ .

The temperature dependent gap function mentioned above is only for the conventional BCS superconductors. Several theories are introduced to extend the gap function, and the  $\alpha$  model is most famous one [3]. For the strongly-coupled but still isotropic *s*-wave superconductors, an additional parameter is introduced as  $\alpha = \Delta(0)/k_B T_c$ , which is 1.76 for the conventional superconductors. With this model, the equations in the BCS theory is easily adopted for the strongly-coupled superconductors. Just simple substitution of  $\Delta(0) = \alpha \cdot k_B T_c$  help that the gap function can be applied to the strongly-coupled systems.

After the discovery of many unconventional superconductors, such as the high

$T_c$  cuprates with the  $d$ -wave gap symmetry, another approximate gap function is employed for various gap symmetries as

$$\Delta(T) = g(\mathbf{k}) \cdot \Delta_0(0) \tanh \left[ \frac{\pi T_c}{\Delta(0)} \sqrt{a \left( \frac{T_c}{T} - 1 \right)} \right]$$

with new parameters of  $g(\mathbf{k})$  and  $a$  with  $\Delta_0(0)$  [4]. These 2 parameters are dependent on the gap symmetry. This approximated gap function is very close with the parameters, for example,  $g(\mathbf{k}) = 1$ ,  $a = 1$ ,  $\Delta_0(0) = 1.76 \cdot k_B T_c$  for the isotropic  $s$ -wave superconductors, and  $g(\mathbf{k}) = \cos(2\phi)$ ,  $a = 4/3$ ,  $\Delta_0(0) = 2.14 \cdot k_B T_c$  for the 2-dimensional  $d$ -wave ones [4].

The temperature dependent functions of the superconducting energy gap are employed to interpret many temperature dependent physical properties including the electronic specific heat and the lower critical fields. Further theoretical analysis for experimental data of those physical properties will be discussed in this chapter.

### 2.1.1.2-gap model of electronic specific heat

The electronic specific heat  $C_P$  is estimated from the electronic entropy  $S$  with the well-known relation.

$$C_P = T \frac{dS}{dT}$$

The electronic entropy in the superconducting state is given by

$$S = -\frac{6}{\pi^2 k_B} \cdot \Delta_0 \cdot \gamma_N \int_0^\infty [f \ln f + (1-f) \ln(1-f)] dy$$

within the assumption of the famous  $\alpha$ -model [3, 5]. In the above equation,  $k_B$ ,  $\Delta_0$ , and  $\gamma_N$  are the Boltzmann constant, the size of the superconducting energy gap at zero temperature, and the normal state electronic specific heat so called the

Sommerfeld coefficient, respectively. The Fermi function is introduced as

$$f = \left[ \exp\left(\frac{\sqrt{\epsilon^2 + \Delta^2(T)}}{k_B T}\right) + 1 \right]^{-1}$$

where  $\epsilon$  is the energy of the normal electrons relative to the Fermi surface. The integration variable in the above equation of the electronic entropy is  $y = \epsilon/\Delta_0$  [5].

Then, the electronic entropy equation is reduced with a new integration variable of  $E = \sqrt{\epsilon^2 + \Delta^2(T)}$  as

$$S = -\frac{6}{\pi^2 k_B} \cdot \gamma_N \int_{\Delta(T)}^{\infty} [f \ln(f) + (1-f) \ln(1-f)] \frac{E}{\sqrt{E^2 - \Delta^2(T)}} dE$$

with the Fermi function of  $f = [\exp(E/k_B T) + 1]^{-1}$  and the superconducting gap function  $\Delta(T)$ .

The electronic specific heat in the superconducting state is calculated from the derivative of the above electronic entropy equation. By adjusting the  $\alpha$  value, which is corresponding to the zero temperature superconducting energy gap size and defined as  $\alpha = \Delta_0/k_B T_c$ , the temperature dependence of the electronic specific heat for various gap size is obtained and shown in figure 2.2. The  $\alpha$  value is varied from 0.3 to 3.0 with a step of 0.3, and the corresponding specific heat curves are presented. Only the curve of  $\alpha = 1.8$  is replaced with the curve of  $\alpha = 1.76$  which represents the conventional BCS superconductors. The curve for the BCS one is presented as the black line in the figure. The dashed line represents the normal state electronic specific heat. For convenience, the normalized specific heat  $C_p/T \cdot \gamma_N$  and the reduced temperature  $t = T/T_c$  are employed for the figure.

The well-known specific heat jump at the superconducting transition temperature is found in the figure, and one can notice that the size of the specific heat jump is larger in the superconductor with larger gap. Since the electronic

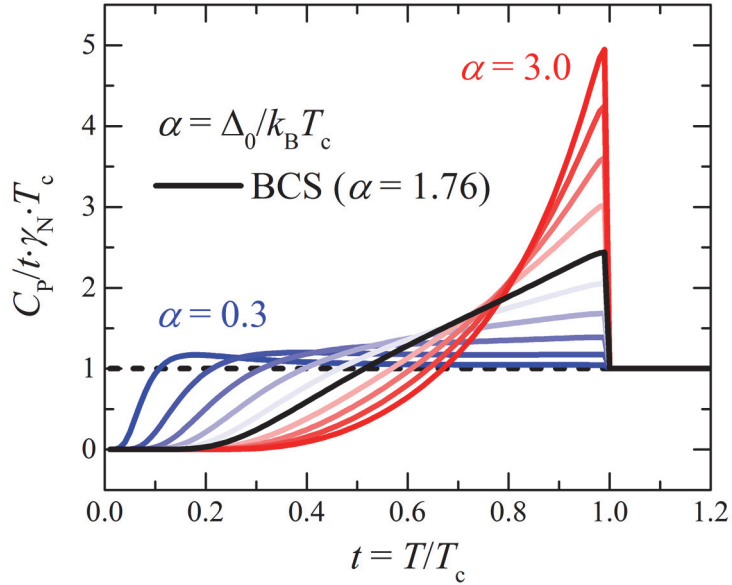


**Figure 2.2.** The temperature dependence of electronic specific heat calculated with the  $\alpha$  model. As the axes,  $C_p/T$  normalized with the normal state  $\gamma_N$  and the reduced temperature are employed. The solid lines indicate the calculated curves and the dashed line indicates the normal state  $\gamma_N$ . For the calculation, various  $\alpha$  values are chosen from 0.3 to 3.0 with a step of 0.3. Only the curve with  $\alpha = 1.8$  is replaced by one with  $\alpha = 1.76$ , the conventional BCS one.

entropy should be conserved in both superconducting and normal states, the nearly zero specific heat at low temperature is observed in wider temperature window in the curve with the larger gap as the consequence of the larger jump at the transition. In contrast to the larger gap one, the specific heat of a small gap superconductor is estimated to increase exponentially from lower temperature and to have smaller jump at the transition.

This tendency is related to the quasiparticle excitation across the

superconducting energy gap [5]. With a characteristic temperature of  $T_{\Delta} = (\alpha/3.52) \cdot T_c$ , the comparison between the temperature scale helps to understand the tendency. At the low temperature where  $T \ll T_{\Delta}$ , the quasiparticle is difficult to be excited across the energy gap by the thermal fluctuation. The difficulty makes the very small electronic specific heat. As the temperature increases, the possibility of the thermal excitation increases to be comparable to the normal state value even though the system is still superconducting. When the superconducting energy gap is closed at  $T_c$ , the quasiparticles remaining in the BCS ground state are suddenly excited into the normal states and it causes the specific heat jump. The number of remaining quasiparticles, and the specific heat jump size, are strongly dependent to the superconducting gap size therefore.

In the multi-gap superconductors, the normal state electronic specific heat is the sum of the contributions from each gap. Then, the fraction of each gap would be realized as  $x_i = \gamma_i/\gamma_N$  while  $\sum x_i = 1$ . Then, the total electronic entropy would be the sum of the each gap's contribution estimated independently from the above equation. In the case of a 2-gap superconductor, for example, the total electronic entropy would be  $S = x_1 \cdot S_1 + (1 - x_1) \cdot S_2$  and there are only 5 free parameters of  $x_1$ ,  $\Delta_1$ ,  $\Delta_2$ ,  $\gamma_N$  and  $T_c$ . If the temperature dependent electronic specific heat is measured, the 2-gap fitting can be performed to obtain the former 3 parameters,  $x_1$ ,  $\Delta_1$ , and  $\Delta_2$ , while the latter 2 parameters are realized from the experimental results.

### **2.1.2.2-gap model of lower critical fields**

The lower critical field  $H_{c1}$  is one of the critical fields observed in the type-2 superconductors. It is the magnetic fields where a very first flux vortex penetrates into the superconductor. For a 2-dimensional system with a layered structure, the

lower critical fields can be expressed as following London formulae

$$\begin{cases} H_{c1}^c = (\Phi_0/4\pi\lambda_{ab}^2) \cdot \ln \kappa_c \\ H_{c1}^{ab} = (\Phi_0/4\pi\lambda_{ab}\lambda_c) \cdot \ln \kappa_{ab} \end{cases}$$

where  $\Phi_0$  is the flux quantum and  $\lambda_{ab}$  is the penetration depth along the  $ab$ -plane while  $\lambda_c$  is one along the  $c$ -axis. The Ginzburg-Landau parameters  $\kappa_{ab}$  and  $\kappa_c$  are defined as  $\kappa_c = \lambda_{ab}/\xi_{ab}$  and  $\kappa_{ab} = \sqrt{\lambda_{ab}\lambda_c/\xi_{ab}\xi_c}$  with the coherence length  $\xi_{ab}$  and  $\xi_c$ . From these expressions, one can estimate the penetration depth or the coherence length from the lower critical fields measurements based on the combination with other measurements.

Even if one can only measure the lower critical fields, the normalization of the lower critical fields provide the normalized penetration depth. In the case of the lower critical fields with the external magnetic fields along the  $c$ -axis, the normalized lower critical fields can be expressed as

$$H_{c1}^c(T)/H_{c1}^c(0) = \lambda_{ab}(0)^2/\lambda_{ab}(T)^2 = \rho_S(T)$$

with the temperature dependent superfluid density  $\rho_S(T)$  and the assumption of the temperature independent Ginzburg-Landau parameters. Since the superfluid density is dependent on the superconducting energy gap, the temperature dependence of the lower critical fields also depends on the characteristics of the superconducting energy gap.

Within the local approximation,  $\lambda > \xi$ , and the constant Fermi velocity approximation, the superfluid density in the Meissner state is simplified as

$$\rho_S = 1 + 2 \int_0^\infty dE \frac{\partial f(E)}{\partial E} \frac{N(E)}{N(0)} = 1 + 2 \int_{\Delta(T)}^\infty dE \frac{\partial f(E)}{\partial E} \frac{E}{\sqrt{E^2 - \Delta^2(T)}}$$

where  $f(E)$  is the Fermi function and  $N(E)/N(0)$  is the angle averaged

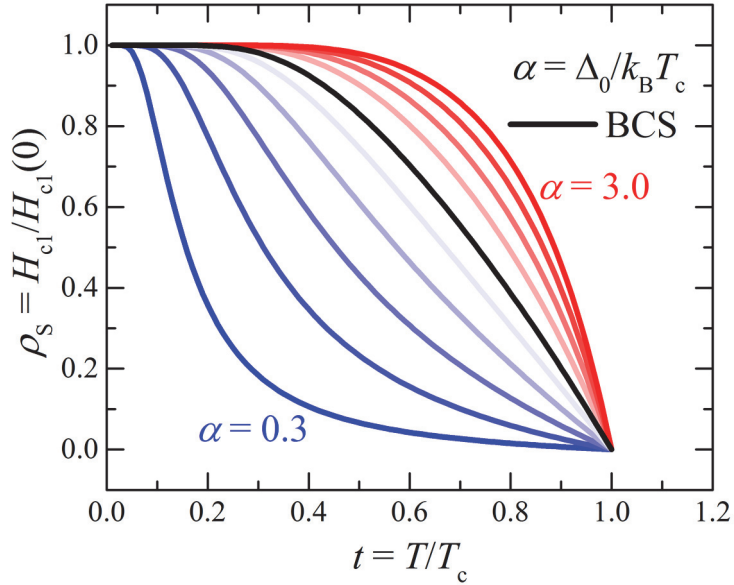


**Figure 2.3.** The temperature dependence of lower critical fields calculated with the  $\alpha$  model. As the axes, the lower critical fields normalized with the zero temperature one and the reduced temperature are employed. The solid lines indicate the calculated curves. For the calculation, various  $\alpha$  values are chosen from 0.3 to 3.0 with a step of 0.3. Only the curve with  $\alpha = 1.8$  is replaced by one with  $\alpha = 1.76$ , the conventional BCS one.

superconducting density of states divided by the normal state value at the Fermi level [2]. Then, only thing needed to calculate the superfluid density of the system is the temperature dependent gap function,  $\Delta(T)$ . For the isotropic  $s$ -wave-like superconducting gap with various  $\alpha$  values, one can employ the gap function discussed above,  $\Delta(T) = \Delta(0) \tanh[1.82 \cdot \{1.018 \cdot (T_c/T - 1)\}^{0.51}]$  where the zero temperature gap size is determined as  $\Delta(0) = \alpha \cdot k_B T_c$ .

Now, one can summarize the normalized lower critical fields as an equation based on the superconducting gap function.

$$\frac{H_{c1}(T)}{H_{c1}(0)} = 1 + 2 \int_{\Delta(T)}^{\infty} dE \frac{\partial f(E)}{\partial E} \frac{E}{\sqrt{E^2 - \Delta^2(T)}}$$

With this equation, the temperature dependence of the lower critical fields can be predicted with specific transition temperature and superconducting gap size. The calculated curves with various  $\alpha$  values are presented in figure 2.3. Thick black line represents the conventional BCS superconductors' curve, whose  $\alpha = 1.76$ . From the bottom and blue line with  $\alpha = 0.3$  to the top red line with  $\alpha = 3.0$ , 10 different  $\alpha$  values with a step of 0.3 are chosen. Only  $\alpha = 1.8$  is replaced with the BCS one. The reduced temperature  $t = T/T_c$  is employed as well as the superfluid density.

One common properties of the calculated curves is a plateau at the very low temperature. Although the temperature window for the plateau is depending on the gap size, this behavior is clearly different from the cases with other gap symmetry such as the  $d$ -wave one [4]. The superfluid density of  $d$ -wave superconductors is known to keep increasing down to zero temperature without any plateau [4]. Another noticeable point in the calculated curves in figure 2.2 is that the stiff increase of the superfluid density occurs at some temperature and this characteristic temperature is related to the gap size. In the superconductor with a large gap, for example, of  $\alpha = 3.0$ , the superfluid density starts to increase rapidly from the transition temperature. A small gap superconductor with  $\alpha = 0.3$  shows the stiff increase of the superfluid density below  $\sim 0.3T_c$ , in contrast. The  $\alpha$  value of the system as well as the superconducting gap size, therefore, can be predicted roughly based on only the temperature dependence of the lower critical fields.

Above equations and calculations are limited in the single-gap superconductors. For the multi-gap systems, a concept of simple linear combination is applied. The total superfluid density of the multi-gap system is the sum of the superfluid density

of each gap's contribution. For example, a 2-gap superconductor will be understood to have the superfluid density of

$$\rho_S = x_1 \cdot \rho_{S1} + x_2 \cdot \rho_{S2} = x_1 \cdot \rho_{S1} + (1 - x_1) \cdot \rho_{S2}$$

with the each gap's fraction of  $x_1$  and  $x_2$ . Since the total fraction  $x_1 + x_2$  must be 1, the number of unknown parameters is reduced into 3, the fraction of one gap  $x_1$  and the gap sizes of the gaps  $\Delta_1(0)$  and  $\Delta_2(0)$ . With the same manner, the system with more multiple gaps can be described.

## 2.2. 2-band model of magneto-resistance and Hall effect

The Hall effect provides important information about the charge carrier and the band structure of the system. In the semi-classical picture, the charge carrier moving along the electrical current feels the Lorentz force under the magnetic fields, changing the trajectory of the charge carrier. If we assume a 2-dimensional system with the external magnetic fields along the out-of-plane direction, the simple calculation results that the Hall coefficient as

$$R_H = \frac{\rho_{xy}}{B} = \frac{1}{nq}$$

where  $B$  is the external magnetic fields  $n$  is the carrier density and  $q$  is the charge of the carrier [6]. The Hall resistivity  $\rho_{xy}$  is defined as  $\rho_{xy} = E_y/J_x$  while one assume that the electrical current flows along  $x$ -direction. Most of the charge carriers have the net charge of  $e$ , the elementary charge, and only the sign depends on the type of the carrier, whether it is an electron-carrier or a hole-carrier. The sign of the Hall resistivity, therefore, imply the type of the charge carrier directly and the carrier density can be estimated easily. The resistivity  $\rho_{xx}$ , on the other hand, is expected to be  $\rho_{xx} = 1/en\mu$  where  $\mu$  is the mobility of the carrier. By measuring

the resistivity and the Hall resistivity, therefore, one can extract the type, the carrier density, and the mobility of the charge carrier which are closely related to the band structure.

Many other materials, however, can't be described fully within the semi-classical picture because of their complicated band structure. The multi-band metallic system, for example, each band contributes to the transport properties including the resistivity and the Hall resistivity with its own characteristics such as the carrier density and the mobility. To reduce the complexity due to the multi-band nature, one commonly applies an approximate simple 2-band model to the system. In the 2-band model, a resistivity tensor representing the contribution from each band is expected to be

$$\vec{\rho}_i = \begin{pmatrix} \rho_i & -R_i B \\ R_i B & \rho_i \end{pmatrix}$$

where  $\rho_i$  is the resistivity and  $R_i$  is the Hall coefficient of  $i$ th band. Then, the total resistivity tensor is described as

$$\vec{\rho} = (\vec{\rho}_1^{-1} + \vec{\rho}_2^{-1})^{-1}$$

and then

$$\begin{pmatrix} \rho & -RB \\ RB & \rho \end{pmatrix}^{-1} = \begin{pmatrix} \rho_1 & -R_1 B \\ R_1 B & \rho_1 \end{pmatrix}^{-1} + \begin{pmatrix} \rho_2 & -R_2 B \\ R_2 B & \rho_2 \end{pmatrix}^{-1}$$

based on the simple parallel resistor formula, and the equation is solved further with the inverse matrix to obtain the simultaneous equations.

$$\begin{aligned} & \frac{1}{\rho^2 + R^2 B^2} \begin{pmatrix} \rho & RB \\ -RB & \rho \end{pmatrix} \\ &= \frac{1}{\rho_1^2 + R_1^2 B^2} \begin{pmatrix} \rho_1 & R_1 B \\ -R_1 B & \rho_1 \end{pmatrix} + \frac{1}{\rho_2^2 + R_2^2 B^2} \begin{pmatrix} \rho_2 & R_2 B \\ -R_2 B & \rho_2 \end{pmatrix} \end{aligned}$$

And then the simultaneous equations are obtained.

$$\begin{cases} \frac{\rho}{\rho^2 + R^2 B^2} = \frac{\rho_1}{\rho_1^2 + R_1^2 B^2} + \frac{\rho_2}{\rho_2^2 + R_2^2 B^2} = \mathcal{A} \\ \frac{RB}{\rho^2 + R^2 B^2} = \frac{R_1 B}{\rho_1^2 + R_1^2 B^2} + \frac{R_2 B}{\rho_2^2 + R_2^2 B^2} = \mathcal{B} \end{cases}$$

To solve the simultaneous equations, the complex arithmetic is employed.

$$\mathcal{A} - i\mathcal{B} = \frac{\rho - iRB}{\rho^2 + R^2 B^2} = \frac{\rho_1 - iR_1 B}{\rho_1^2 + R_1^2 B^2} + \frac{\rho_2 - iR_2 B}{\rho_2^2 + R_2^2 B^2}$$

The numerators and denominators are reduced.

$$\frac{1}{\rho + iRB} = \frac{1}{\rho_1 + iR_1 B} + \frac{1}{\rho_2 + iR_2 B} = \frac{(\rho_1 + iR_1 B) + (\rho_2 + iR_2 B)}{(\rho_1 + iR_1 B)(\rho_2 + iR_2 B)}$$

By inversion of the fraction

$$\begin{aligned} \rho + iRB &= \frac{(\rho_1 + iR_1 B)(\rho_2 + iR_2 B)}{(\rho_1 + iR_1 B) + (\rho_2 + iR_2 B)} \\ &= \frac{(\rho_1 \rho_2 - R_1 R_2 B^2) + i(\rho_1 R_2 B + R_1 \rho_2 B)}{(\rho_1 + \rho_2) + i(R_1 + R_2)B} \\ &= \frac{\{(\rho_1 \rho_2 - R_1 R_2 B^2) + i(\rho_1 R_2 B + R_1 \rho_2 B)\} \cdot \{(\rho_1 + \rho_2) - i(R_1 + R_2)B\}}{(\rho_1 + \rho_2)^2 + (R_1 + R_2)^2 B^2} \end{aligned}$$

and the separation of the real and imaginary parts

$$\begin{cases} \rho = \frac{\rho_1 \rho_2 (\rho_1 + \rho_2) + (\rho_1 R_2^2 + \rho_2 R_1^2) B^2}{(\rho_1 + \rho_2)^2 + (R_1 + R_2)^2 B^2} \\ R = \frac{(\rho_1^2 R_2 + \rho_2^2 R_1) + R_1 R_2 (R_1 + R_2) B^2}{(\rho_1 + \rho_2)^2 + (R_1 + R_2)^2 B^2} \end{cases}$$

one can finally obtain the expression of the resistivity and the Hall coefficient while  $\rho = \rho_{xx}$  and  $R = \rho_{xy}/B$ . As realized in the final equations, both of the magneto-resistance and the Hall resistivity are not quadratic or linear to the magnetic fields which is in contrast to the expectation in the simple 1-band model.

Even though the magneto-resistance and the Hall resistivity have to exhibit complex magnetic-field-dependence, it can be found to be simple linear or quadratic to the fields in some extreme limit. The compensated metal, for example, which is the system can be approximated into the 2-band model with electron- and hole-bands, would show the field-independent Hall coefficient because the Hall coefficient of the electron- and hole-bands have same amplitude but opposite sign to each other resulting the cancellation of the  $B^2$  term in the numerator and the denominator at the same time. In that case,  $\rho$  and  $R$  can be reduced as

$$\begin{cases} \rho = \frac{\rho_1\rho_2 + R_2^2B^2}{\rho_1 + \rho_2} \\ R = \frac{\rho_1 - \rho_2}{\rho_1 + \rho_2} \cdot R_2 \end{cases}$$

implying that the magneto-resistance is quadratic to the magnetic fields and the Hall resistivity is linear to the fields.

The model discussed above is not yet including the magnetic field dependence of the each band's resistivity  $\rho_i$ . Due to various causes, the resistivity of each band can have arbitrary field dependence and it may be not negligible in some systems. To include the field dependence, one needs to substitute  $\rho_i$  in the equations with  $\rho_i(B)$  at the very last step and to re-arrange the formula into the field-independent and field-dependent terms. For the arbitrary field dependence, one can employ the series expansion to reduce the complexity. The Hall resistivity of the compensated metal, for instance, would magnetic field dependence as

$$R \approx \frac{(\rho_1 - \rho_2) + (\epsilon_1 - \epsilon_2)B}{(\rho_1 + \rho_2) + (\epsilon_1 + \epsilon_2)B} \cdot R_2$$

where the magneto-resistance of each band can be approximated as  $\rho_i(B) \approx \rho_i + \epsilon_i B + O(B^2)$ .

It has to be noted that the field-independent terms in both of  $\rho$  and  $R$  are not changed even if any kind of magnetic fields dependence or approximations is considered.

$$\left\{ \begin{array}{l} \rho \approx \frac{(\rho_1 \rho_2)}{\rho_1 + \rho_2} \\ R \approx \frac{\rho_1^2 R_2 + \rho_2^2 R_1}{(\rho_1 + \rho_2)^2} \end{array} \right.$$

These field-independent expression is quite useful to compare the Hall coefficient of various systems with very different magnetic fields dependence of the magneto-resistance and the Hall resistivity.

### 2.3. References

- [1] M. Tinkham, "Introduction to Superconductivity" 2nd ed. (Dover, 2004)
- [2] A. Carrington and F. Manzano, *Physica C* **385**, 205 (2003)
- [3] H. Padamsee *et al.*, *J. Low. Temp. Phys.* **12**, 387 (1973)
- [4] R. Prozorov and R. W. Giannetta, *Supercond. Sci. Tech.* **19**, R41 (2006)
- [5] F. Bouquet *et al.*, *Europhys. Lett.* **56**, 856 (2001)
- [6] J. Singleton, "Band Theory and Electronic Properties of Solids" (Oxford, 2001)

## **3. Experimental method**

### **3.1. Single crystal growth**

The single crystals of 111 systems were grown by the Sn- and self-flux methods, and all preparations for the crystal growth were performed inside the glove box with purified Ar atmosphere whose oxygen and moisture levels have been controlled to be less than 1 ppm. Chemicals of high purity metal elements were also stored in the glove box to avoid the oxidation. Tools including spoons and tweezers were dried in the oven with the dwelling temperature of 80 °C before the chemical preparations. Quartz ampoules also were stored in the oven after the cleaning by an ultrasonic cleaner and the outgassing via some heat treatment by a box furnace.

#### **3.1.1. Sn-flux method**

For the crystal growth by the Sn-flux method, various stoichiometric ratios were tried and the ratio of LiFeAs:Sn = 1:10 which has been used widely for the growth of the 122-type Fe-based superconductor crystals in our group [1-4] was realized to be optimal in this 111 crystals. High purity chemicals of Li, Fe, As, and Sn were weighed in the glove box and placed in an alumina crucible with some specific order. As and Fe powders were placed first, and then an half of Sn shots was poured on the powders. Li granules were placed on the Sn shots and the remaining Sn shots were poured again. This order was introduced to make sure that the Li granules were dissolved into the molten Sn-flux fully. The crucible carrying the chemicals was paired with another alumina crucible which was covered and partially filled with some quartz wool and the pair was clamped by a piece of Ta foil. The quartz wool

between the crucibles played a role as a sieve to separate the crystals from the molten flux during a centrifuge. The Ta foils clamped the pair of the crucibles to prevent flooding of the molten flux during the centrifuge and also absorbed the oxygen during the high temperature sequence. The clamped pair was protected by a quartz ampoule. Some quartz wool were loaded at the bottom and the top of the pair as a buffer. Without these wool buffer, the ampoule could be broken during the sealing process because of the thermal expansion of the alumina crucibles. At the top of the pair and the quartz wool, a quartz rod was placed.

The quartz ampoule carrying the crucibles was taken out from the glove box while it was closed by an O-ring fitting and a ball valve. Several conditions of pumping and pressure control were employed for the sealing. Typically, the quartz ampoule was purged with pure Ar gas more than 5 times while the ampoule was pumped by a rotary pump. After that purging, the ampoule could be pumped more by the rotary pump, or by a diffusion pump for the lower inside pressure below  $\sim 10^{-5}$  mbar. In some cases, pure Ar gas filled the ampoule with some partial pressure up to  $\sim 0.8$  bar after the purging process to control the evaporation of As and Li. After the pumping and the gas control, the ampoule was sealed and placed in the box furnace.

The ampoule was heated up to 850 °C with 2 temperature steps at 250 and 500 °C, which were chosen to dissolve Li and As thoroughly into the Sn-flux, respectively, based on the binary phase diagram [5]. Figure 3.1 present the binary phase diagrams reported previously [5]. The thick dotted lines in figure 3.1 (a), (c), and (d) indicate the specific stoichiometric ratio of  $X:\text{Sn} = 1:10$  for  $X = \text{Li}, \text{Fe},$  and  $\text{As}$ , respectively. According to the phase diagrams, Li and As are expected to be fully dissolved into the flux at  $\sim 250$  and  $500$  ° C. The temperature, therefore, was

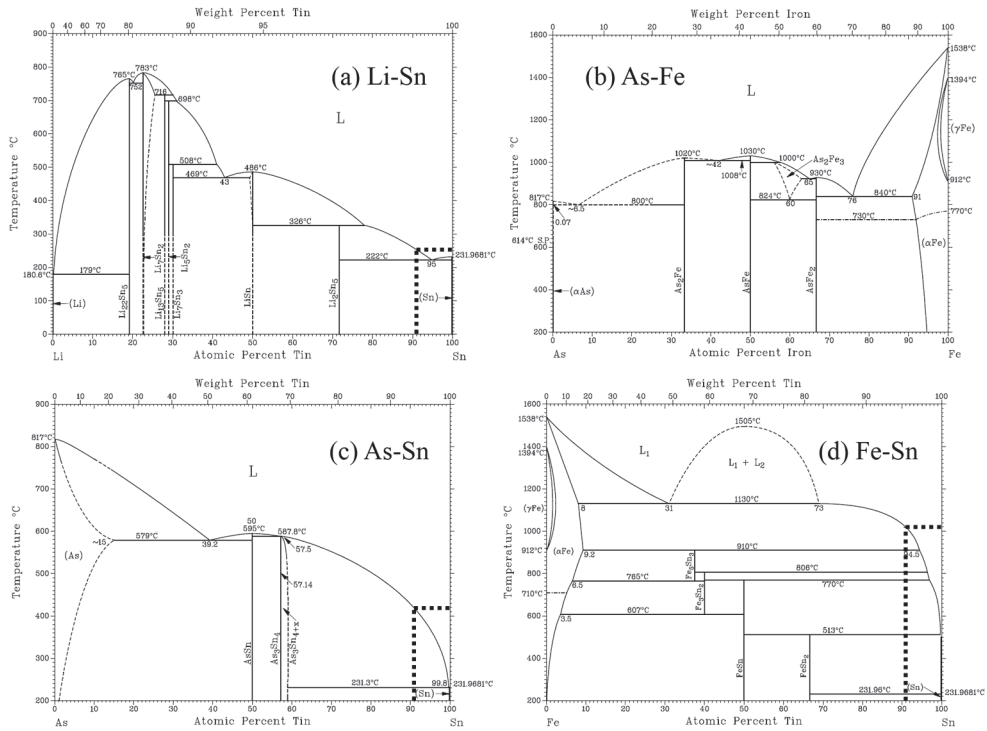


**Figure 3.1. Binary alloy phase diagram of (a) Li-Sn, (b) As-Fe, (c) As-Sn, and (d) Fe-Sn [5]. The thick dotted lines in (a), (c), and (d) are noted for the stoichiometric ratio of 1:10 for Li-Sn, As-Sn, and Fe-Sn. The ratio is chosen and used for the Sn-flux method.**

controlled to ramping up with a rate of 100 °C/h and to dwell at 250, 500, and 850 °C for 24, 4, and 4 hours, respectively, to help the dissolving and melting of the chemicals. After the heating and dwelling at highest temperature, the ampoule was slowly cooled down to 500 °C with a rate of 3.5 °C/h to grow the crystals. After the growth, the ampoule was centrifuged to separate the crystals from the flux. The ampoule was take out from the furnace while the temperature was controlled to be 500 °C and quickly placed upside down in the centrifuge. For the in-flux-annealing, the ampoule was kept in the furnace with the temperature of 500 °C several days

from right after the growth, and then centrifuged. For the lower-temperature-centrifuge, the ampoule was cooled down to 400 °C, instead of 500 °C, and then centrifuged.

After the growth, the ampoule was put into the glove box again since the crystals are extremely sensitive to the oxygen and degraded very easily in the air. The ampoule was broken inside the glove box and the crystals were harvested at the top of the quartz wool between the crucibles or at the bottom of the crucible which had carried the chemicals at the very first. The harvested crystals were kept in the glove box to avoid the degradation.

### **3.1.2. Self-flux method**

The crystal growth by the self-flux method was tried for both of the quartz ampoule and the Nb bomb. Since the vapor pressure of Na is relatively high even at the temperature below ~ 1100 °C [7] and the Na gas attacks and breaks the quartz, the crystals containing Na cannot be grown by the quartz ampoule and Nb bombs must be employed for the growth. For the convenience, LiFeAs- and NaFeAs-based crystals were grown by the quartz ampoule and the Nb bomb, respectively.

To match the growth condition of LiFeAs and NaFeAs, several stoichiometric ratios were tried and the ratio of (Li,Na):Fe:As = 3:2:4 was chosen for the growth. For the LiFeAs and related crystals, Li granules were weighed first and then As and Fe powders were weighed, but the powders were placed into the alumina crucible first and then the Li granules were added on the powders to avoid the reaction between the Li liquid and the alumina. If the Li liquid touched the alumina crucible first, the liquid easily penetrates into and reacted with the alumina, and also attacks the quartz beyond the crucible to break the ampoule. This accident must be avoided

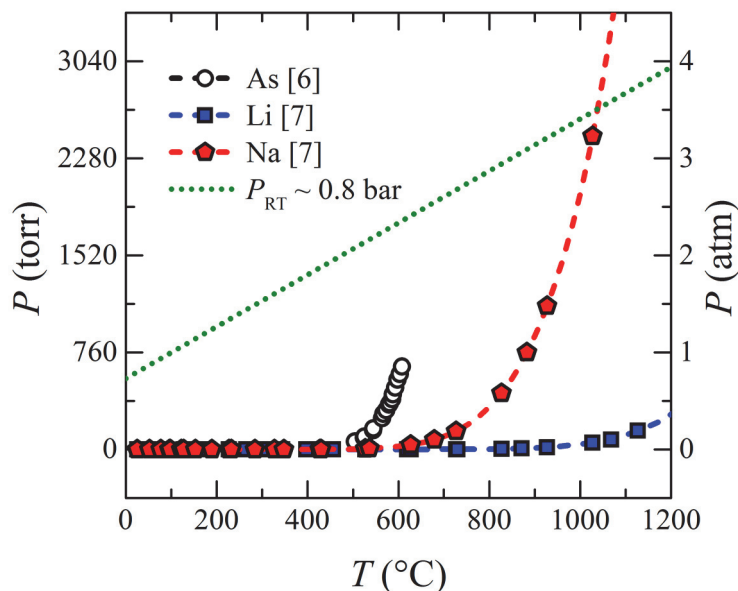


**Figure 3.2. Temperature dependent vapor pressure curves for As, Li, and Na [6-7]. Circles, squares, and pentagons indicate As, Li, and Na, respectively, and the dashed lines are drawn as guidelines. The inside pressure of the carrier which is expected to be built by the Ar gas of  $\sim 0.8$  bar at the room temperature is calculated with the simple ideal gas equation and presented as the dotted line.**

for the successful growth as well as for the safety. The crucible carrying the chemicals was loaded on the top of the bottom quartz wool buffer in the quartz ampoule. Another crucible covered it as a lid. And the top quartz wool buffer and the quartz rod were put on the pair of the crucibles. The quartz ampoule carrying the crucible pair was sealed with partial Ar pressure of  $\sim 0.8$  bar, filled after the 5-time purging with pure Ar gas performed by the rotary pump.

In the cases of the growth of NaFeAs-based crystals, Na was weighed first. 2 types of Na, solid in the ampoule or pieces in mineral oil, were used for the growth.

To use the Na pieces in the oil, the surfaces were cleaned and removed to avoid unexpected impurities come from the oil. The Na solid or pieces weighed first was placed in an alumina crucible and then As and Fe powders were weighed and added. For the Li-doped crystals, Li granules were added on the powders at the very last. This order was also introduced to avoid the reaction between Li and the alumina.

An Nb bomb was prepared from the simple tube and a lid which was shaped by a press and a mold. The lid was inserted in one side of the tube and welded by arc melting. The alumina crucible with the chemicals was carried by this one-side-welded Nb bomb. Another lid was inserted into the open side of the bomb carefully. To prevent the air exposure, the open-side of the bomb was temporarily protected by some latex and rubber band. The bomb with the protection was taken out from the glove box and mounted on the arc melting chamber quickly, and the protection was removed at the very last moment to minimize the exposure. The chamber was purged 3-time with pure Ar gas by the rotary pump and pumped by the diffusion pump to remove all oxygen inside. The bomb was welded while the chamber was filled with the Ar gas with the pressure of  $\sim 0.8$  bar. The welded bomb was protected by an evacuated quartz ampoule. The ampoule was purged more than 3 times and then sealed while it was being pumped.

The ampoule was heated up to 1050 °C directly within 6 hours and dwelled 1 hour at that temperature. The highest temperature of 1050 °C was chosen based on the binary phase diagram of As and Fe [5]. According to the binary phase diagram of As-Fe, shown in figure 3.1. (b), the melting point of As-Fe mixtures with the ratio of As:Fe = 2:1 is 1020 °C. The highest temperature is determined to be between this melting temperature and the typical experimental limit of the quartz. After the dwelling, the furnace was controlled to cool down to 750 °C with a rate of 3 °C/h

and then turned off while the ampoule was still kept in the furnace. Harvesting process including the breaking of the quartz ampoule and the opening of the Nb bomb was performed in the glove box. In contrast to the case of the Sn-flux method, crystals grown by the self-flux method should be separated from the flux mechanically. Usually the crystals with shiny surfaces were cleaved from the flux by a razor blade or other type of cutting tools.

### **3.2. Preparation for various measurements**

Since the crystals of LiFeAs, NaFeAs, and related compounds are extremely sensitive to and very easily degraded in the air, every single procedure to prepare the measurements was performed in the glove box. The oxygen and moisture levels inside the glove box were checked regularly by a hygrometer and Na pieces which is extremely sensitive to the oxygen and moisture. To prepare the sample in the glove box, a microscope and a camera connected to a monitor was brought into the glove box as well as a hotplate and a scale. Materials in liquid form, including a silver conductive paste and its solvent, a pair of silver conductive epoxies, the GE varnish and related solvents, the N-grease, were carefully treated to avoid the contamination of the atmosphere inside the glove box. Some of the materials were treated in special way to minimize the contamination of the atmosphere inside the glove box. The N-grease was heated up to 100 °C to reduce the water or air contents inside before placed inside the glove box. The varnish was diluted by an acetone-toluene solution, instead of a methanol-toluene solution to avoid the water impurity in the methanol.

#### **3.2.1. X-ray diffraction**

Powder x-ray diffraction (XRD) measurements were performed by a high-

resolution x-ray diffractometer with a sample stage built for a quartz capillary. Outer diameter of the quartz capillary was 0.3 or 0.5 mm. The powder for the measurements was obtained from the crystal pieces which were carefully selected and cleaned to exclude the flux for the measurements. The crystals were scratched by the razor blade not grounded in the mortar since it was tough to ground the crystals into fine powder because of their plate-like shape. The powder were gathered and poured into the capillary carefully. The capillary with the powder was temporarily sealed by a rubber tape in the glove box to prevent the air exposure. It was taken out from the glove box and then sealed as quickly as possible. The sealed capillary was loaded on the sample stage with a goniometer to align it. While the measurements were performed with Debye-Scherrer geometry, the capillary had been spinning to reduce the preferred orientation problem. The diffraction signal usually was collected more than 20 hours for the Rietveld analysis. The measured pattern was refined by the FullProf Suite program with references of the reported structural parameters.

For some pieces of the crystals, the XRD measurements were performed on the crystal pieces, not on the powder. A crystal sample was loaded on a sample holder with a hole. A piece of sticky tape covered the hole very carefully and the sample was attached on the sticky side of the tape. The N-grease had covered the sample usually to protect the sample from the air. The grease was melted by the hotplate inside the glove box and the molten grease was applied on the sample thoroughly. The holder was taken out from the glove box and mounted on the stage of the diffractometer while the taped-side, not the greased-side, of the sample facing the x-ray. Since the cross-section for clear diffraction pattern was limited, the sample was carefully re-aligned to obtain clear diffraction pattern.

### 3.2.2. Composition measurement

Electron probe micro-analyzer (EPMA) and inductively coupled plasma atomic emission spectroscopy (ICP-AES) measurements were performed on the crystals to confirm their actual compositions. Because Li content couldn't be detected by the EPMA measurements, some specimens among the crystals subjected in the study were selected for the ICP-AES measurements. Both EPMA and ICP-AES measurements were performed via collaborations.

For the EPMA measurements, crystals with clean surfaces were chosen carefully and carried by an evacuated quartz tube. The crystals were attached on the sample holder with some carbon tape and brought into the chamber as quickly as possible to minimize degradation of the surfaces. Any other treatment or preparation was not necessary since the crystals were metallic enough to measure. In general, more than 3 pieces of crystals from one batch were measured to confirm the homogeneity of chemical composition within each batch and also more than 5 points per piece were measured to confirm the homogeneity within each piece.

For the ICP-AES measurements, also clean crystals were selected even more carefully than one for the EPMA measurements since ICP-AES measures chemical composition of whole samples while EPMA measures single spots with micro-scale at the surface. Selected crystal pieces with total mass of ~ 10 mg were vialled and sealed by some paraffin film until the pieces were dissolved into the acidic solution as a preprocessing, and the preprocessed sample was measured.

The results from the EPMA and ICP-AES measurements were normalized to realize the stoichiometric ratio in the crystals. Since the EPMA results cannot provides information of the Li content, the summation of Fe and one substituting Fe

was chosen to be a scale in the analysis of the EPMA results. On the other hand, the summation of Li and Na was chosen to be a scale in the case of the ICP-AES results.

### **3.2.3. Magnetic property**

Magnetic properties including a superconducting shielding fraction, a normal state magnetic susceptibility, and a magnetic-field-dependent magnetization of the crystals were measured by a magnetic property measurement system (MPMS, Quantum Design) and a vibrating sample magnetometer (VSM) equipped on a physical property measurement system (PPMS, Quantum Design). Since the crystals have the common layered structure, the samples were mounted on a various type of sample holders with 2 kinds of the direction of the magnetic fields, along the  $c$ -axis ( $H//c$ -axis) and along the  $ab$ -plane ( $H//ab$ -plane). The crystallographic direction within the  $ab$ -plane was not considered.

For the measurement performed by MPMS, a transparent straw was employed as a sample holder. A long straw was cut into a half-pipe-shape piece and the sample was attached and covered at the center of the holder by small amount of the varnish. This geometry allowed to apply the magnetic fields along the  $ab$ -plane only. The straw holder with the sample was taken out from the glove box and mounted on the probe as quick as possible to minimize the air exposure.

For the case of the VSM measurements, a quartz holder which has a flat surface along the direction of the magnetic fields and a Cu holder which has a rounded shape. When one used the quartz holder, the sample was placed on the holder and a piece of Kepton tape was applied to hold and cover the sample. The sample was attached and covered by the varnish when the Cu holder was used, which is similar to the case of the straw holder of MPMS. The sample was simply laid on the rounded surface of

the Cu holder when one applied the magnetic fields along the *ab*-plane while 2 quartz rods were employed for the magnetic fields along the *c*-axis. The rods held the sample perpendicular the rounded surface of the Cu holder and were fixed on the holder by the varnish. The holders for the VSM measurements were also loaded on the probe as quick as possible to avoid the degradation of the sample.

The measurements to realize the superconducting volume fraction of the sample were performed with very small magnetic fields such as 10 Oe for both of zero-field-cooled (ZFC) and field-cooled (FC) conditions. The sample, at first, was cooled down to the base temperature of 2 K typically without any applied magnetic fields. After enough time to stabilize the temperature, small finite magnetic fields were applied and the magnetic moments of the sample were measured during the warming. And then, the sample was cooled down to the base temperature again while the magnetic fields were still applied, and the measurement was performed again. Results of the former and the latter were noted the ZFC and FC results, respectively.

The volume and molar magnetic susceptibility and the magnetization of the sample were calculated from the measured magnetic moment and the mass of the sample. The sample was weighed in the glove box before the loading on the holder. The volume of the sample was estimated from the mass and reported or measured structural information.

### **3.2.4. Electronic property**

The electronic properties including electrical resistivity, magneto-resistance, Hall resistivity, and upper critical fields were measured via typical 4- or 6-probe methods. The crystal piece was cleaved to obtain clean surfaces and shaped into a rectangular form. Since the crystals had a layered structure and easily cleaved with

the *ab*-plane, the sample usually had a thin and plate-like shape whose surfaces were perpendicular to the *c*-axis. Thin and enameled Cu wires were usually employed to make electrical contacts on the sample surface. The wires were attached on the surface by the conductive silver epoxy and the epoxy was cured on the hotplate in the glove box. The wired sample was loaded on a sapphire plate and protected by the varnish. When the electrical contacts were made by the silver paste instead of the epoxy, the sample was fixed on the platform first and then the wires placed on the sample appropriately were pasted. The thickness of the sample was measured before the contacts were prepared by a vernier calipers and the planar dimensions such as the width and length were measured from the picture of the sample with the electrical contacts.

The measurements were performed by PPMS. A rotator equipped on PPMS was used to change the direction of the magnetic fields at low temperature without additional air exposure. The DC resistance of the sample was measured by several instruments including the resistivity option equipped on PPMS, a digital multi-meter, a resistance bridge, and a lock-in amplifier with low frequency. The measured resistance was normalized with the sample dimensions. Due to the plate-like shape of the crystal sample, the measured resistivity was the in-plane component.

### **3.2.5. Specific heat**

The specific heat of crystals was measured in PPMS or a closed-cycle refrigerator (CCR). The sample platform with attached thermometer and deposited heater was used for both cryostats. The measurements were performed based on a heat-pulse-method with a curve-fitting-method which includes the 2-tau effect [8]. The accuracy of the setup was confirmed with the measurement of a pure Au sample

as a reference. The results of the Au sample were compared with the reported value [9] and the error was less than 5 % for the temperature below 30 K.

Before measuring the sample, the heat capacity of the addenda including the platform and additional N-grease, which was acting as a thermal and mechanical contact between the platform and the sample, was measured first for the temperature region where one of the sample would be measured. The result was fitted into a polynomial and used in the fitting for the measurements of the sample heat capacity. The samples were protected from the air exposure in 2 kind of methods. First one is to cover the sample fully by the N-grease included in the addenda. Another is to prepare the sample on the sapphire plate and cover it with the varnish and load the sapphire plate with the sample on the platform. For the second method, the heat capacity of the sapphire and the varnish was realized from the references [10-12] and additional measurements. The accuracy of this method also was confirmed with the measurement of the Au sample.

### 3.3. References

- [1] H.-J. Kim *et al.*, Phys. Rev. B **79**, 014514 (2009)
- [2] J. S. Kim *et al.*, J. Phys.: Condens. Matter **21**, 102203 (2009)
- [3] J. S. Kim *et al.*, Phys. Rev. B **82**, 024510 (2010)
- [4] S. Khim *et al.*, Physica C **470**, S317 (2010)
- [5] “*ASM Handbook Volume 3: Alloy Phase Diagrams*” (ASM International, 1992)
- [6] A. Lisak and K. Fitzner, J. Phase Equil. **15**, 151 (1994)
- [7] W. T. Hicks, J. Chem. Phys. **38**, 1873 (1963)
- [8] J. S. Hwang *et al.*, Rev. Sci. Instrum. **68**, 94 (1997)
- [9] D. L. Martin, Phys. Rev. B **8**, 5357 (1973)

- [10] R. Q. Fugate and C. A. Swenson, *J. Appl. Phys.* **40**, 3034 (1969)
- [11] D. G. Archer, *J. Phys. Chem. Ref. Data* **22**, 1441 (1993)
- [12] J. L. Cude and L. Finegold, *Cryogenics* **11**, 394 (1971)

## 4. Superconducting properties of LiFeAs

### 4.1. Introduction

As mentioned in chapter 1, various structure types which consist of Fe-pnictogen, or Fe-chalcogen tetrahedral layers have been found to be superconducting by intensive researches followed after the discovery of the superconductivity in  $\text{La}(\text{O}_{1-x}\text{F}_x)\text{FeAs}$  series [1]. Among these Fe-based superconductors, LiFeAs is one of the most interesting compounds since it is superconducting below  $T_c$  of  $\sim 18$  K at the ambient condition [2-4]. In addition, it has a tetragonal  $\text{Cu}_2\text{Sb}$ -type structure and possesses a single Fe-As layer sandwiched by double Li layers, which implies that there is a unique opportunity to obtain a homogeneous Li terminating surface upon cleaving. This opportunity based on the structural character is very important for many spectroscopic tools including angle-resolved photo-emission, scanning tunneling microscopy, and optical spectroscopy since those tools are very sensitive to the surface state. The possibility to realize the homogeneous surface, therefore, makes LiFeAs a good candidate to investigate the intrinsic property of the Fe-based superconductor family and also increase the need to grow clean and large single crystals of LiFeAs.

The high volatility of Li ions, however, had disrupted the successful growth of stoichiometric LiFeAs single crystals until 3 publications reported the single crystals grown by 3 different methods at 2010 [5-7]. Even though a self-flux method [5], employing FeAs precursor as a flux, and the Bridgman method [6] have been reported to be working for the growth of LiFeAs single crystals, both of methods needed high temperature above the melting point of FeAs,  $\sim 1030$  °C, which might

cause the evaporation of Li. To suppress the evaporation, both methods introduced a metal crucible welded under high Ar pressure. On the other hand, a Sn-flux method, which has been used widely for the single crystal growth of the Fe-based superconductors [8-11], has an advantage of the high solubility of most metallic elements including Li into the Sn flux as well as relatively wide growth temperature window due to the low melting point of Sn,  $\sim 232$  °C, over the other methods. While the incursion of Sn alters the intrinsic properties such as the transition temperature of the spin-density-wave transition in the  $\text{BaFe}_2\text{As}_2$  single crystal grown by the Sn-flux method [8], a quantum oscillation study on the  $\text{CaFe}_2\text{As}_2$  single crystals grown by the Sn-flux method is reported [11], which reflects the low impurity scattering in the crystals grown by the Sn-flux method, in contrast. Those previous works indicate that the Sn-flux method can be used selectively to grow high quality single crystals of the Fe-based superconductors, and also hints the possibility to apply the method to the growth of the  $\text{LiFeAs}$  single crystals.

In this chapter, the successful growth of the  $\text{LiFeAs}$  single crystals by the Sn-flux method is presented. The crystal shows clear superconducting transition in the resistivity, the DC magnetic susceptibility, and the specific heat, indicating the bulk superconductivity as well as the high quality of the crystal. The upper critical fields,  $H_{c2}$ , up to 9 T realized from the resistivity measurements also is discussed further to calculate zero-temperature coherence lengths and a moderate superconducting anisotropy of  $\sim 2.3$  near  $T_c$ , which implies that  $\text{LiFeAs}$  needs to be understood as a moderately-correlated electron system. In addition,  $H_{c2}$  of the  $\text{LiFeAs}$  crystals whose impurity level, which is represented by a residual resistivity,  $\rho_0$ , is controlled by various growth condition are studied. The slope of  $H_{c2}$  near  $T_c$  is independent to  $\rho_0$ , which means  $\text{LiFeAs}$  may be realized to be a clean limit superconductor,

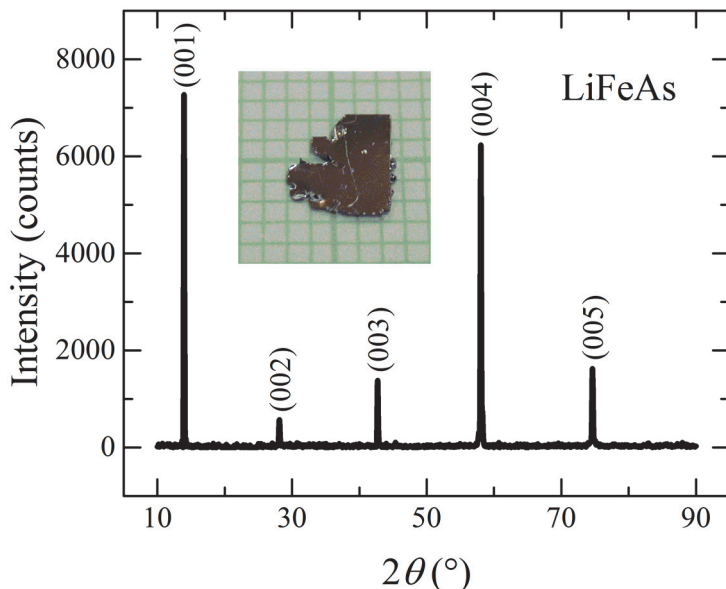


**Figure 4.1.** X-ray diffraction pattern of the LiFeAs single crystal piece aligned along the (001) plane. The Miller indices of each peak are noted in the figure. The inset is a photograph of a crystal piece. Grid in the inset represents 1 mm.

rather than a dirty limit one.

## 4.2. High quality single crystal

Figure 4.1 shows the XRD pattern of a piece of the LiFeAs single crystal grown by the Sn-flux method. Since the pieces have a plate-like shape whose plane is corresponding to the crystallographic  $ab$ -plane, all observed peaks in the pattern can be indexed as  $(00l)$  from a tetragonal structure with a symmetry group of  $P4/nmm$ , which is consistent with the structure reported previously from the polycrystalline sample [2-4]. A  $c$ -axis lattice constant is calculated from the pattern to be 6.35 Å, which agrees to the reported value again [2-4]. Any other impurity phase is not

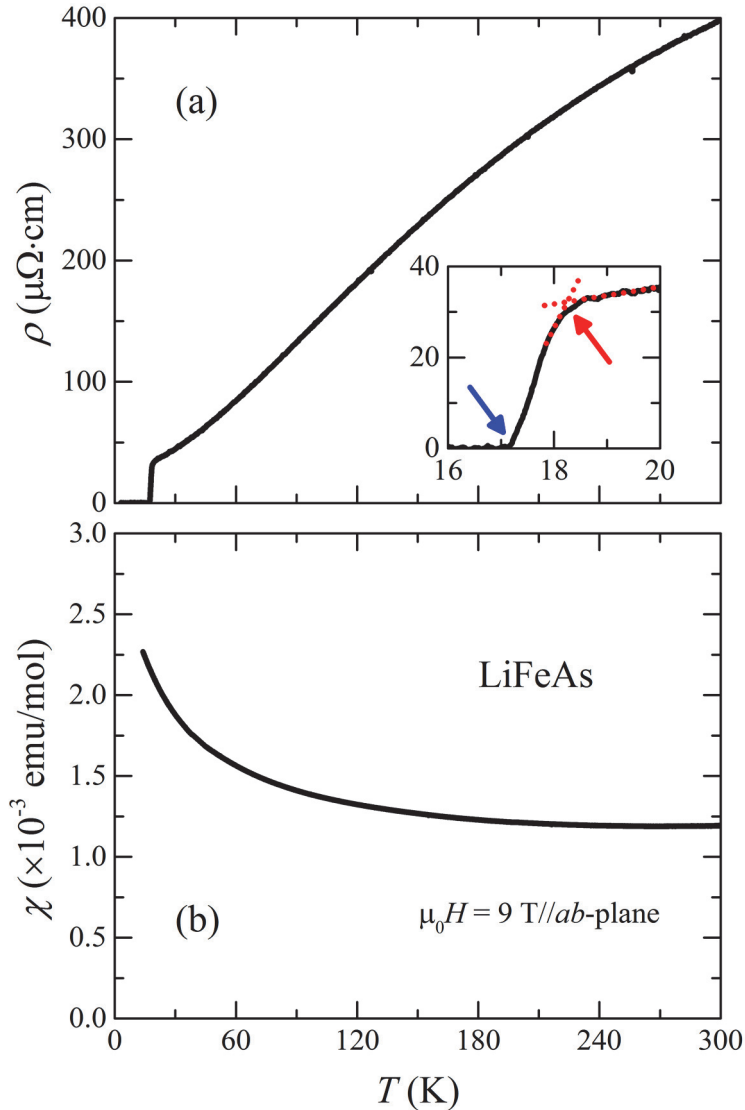


**Figure 4.2.** Temperature dependence of (a) the resistivity and (b) the magnetic susceptibility with applied magnetic fields of 9 T along  $ab$ -plane. The inset of (a) presents the resistivity near the transition. The red and blue arrows in the inset of (a) indicate the onset and zero-resistivity temperature respectively while the dotted lines are linear extrapolations of the normal and superconducting region of the resistivity curve.

detected in the pattern as presented in figure 4.1. The inset of figure 4.1 is a picture of a LiFeAs crystal piece and the size of the grid behind is 1 mm. As shown in the picture, typical lateral size of the clean crystal piece is up to  $5 \times 5 \text{ mm}^2$ .

Electrical resistivity of the crystal measured for the temperature from 3 to 300 K is presented in figure 4.2 (a) while the inset of figure 4.2 (a) presents the resistivity curve near the transition. The onset superconducting transition temperature  $T_{\text{onset}}$  is determined to be 18.2 K from linear extrapolations of the normal and superconducting region of the resistivity curve, presented as dashed lines in the inset of figure 4.2 (a), while the zero resistivity is realized at 17.1 K. It results, therefore, the transition width of 1.1 K, which is smaller than one of the other results, ranging from 2 to 4, based on the crystal grown in the early researches [2, 3, 6, 12]. This narrow transition indicates the high quality of the crystal. As shown in figure 4.2, the resistivity decreases monotonically as the temperature decreases without any anomaly, implying the absence of the spin-density-wave or structural transition. It is also consistent with the previous reports [2-4, 6]. A residual resistivity ratio to the room temperature resistivity (RRR), defined as a ratio of the resistivity at 300 K to a residual resistivity at 0 K, is found to be  $\sim 24$  in the resistivity curve presented in figure 4.2. Even though this value is smaller than one of the crystal grown by the Bridgman method [6], the crystal grown by the Sn-flux method still can be considered to have better quality than one grown by the Bridgman method because the resistivity of the latter is huge to be even  $\sim 0.27 \Omega \cdot \text{cm}$  at 300 K and the transition width of the latter is 2.2 K in the publication [6]. One notes that the value of RRR  $\sim 24$  is one of the smallest values among the pristine compounds of the Fe-based superconductors. Most pristine 122 compounds such as  $\text{BaFe}_2\text{As}_2$  and  $\text{SrFe}_2\text{As}_2$  have much smaller RRR, for example, as  $\sim 6$  and 3 for  $\text{BaFe}_2\text{As}_2$  [13] and  $\text{SrFe}_2\text{As}_2$  [9]

respectively. Only a very limited number of the systems such as  $\text{KFe}_2\text{As}_2$  shows larger RRR above 24, reaching  $\sim 1280$  [14, 15].

Figure 4.2 (b) presents the DC magnetic susceptibility for the temperature from 10 to 300 K measured with the applied magnetic fields of 90000 Oe. No anomaly is found in the magnetic susceptibility up to the room temperature as well as the resistivity, which is indicating the absence of any magnetic ordering in LiFeAs and consistent to the other results [2, 3, 6], in contrast to the cases in the other parent compounds of the Fe-based superconductors. The DC magnetic susceptibility, shown in figure 4.3 (a), is measured under the magnetic fields of  $\sim 10$  Oe applied along the *ab*-plane for both of ZFC and FC conditions. The superconducting shielding fraction realized in the ZFC susceptibility reaches  $\sim 100\%$  at 10 K, and the transition temperature determined as the temperature where the demagnetization signal starts to appear in the ZFC susceptibility is  $\sim 16.8$  K, just below the temperature of 17.1 K where the zero-resistivity is realized.

Figure 4.3 (b) presents the total specific heat divided by the temperature while figure 4.3 (c) presents the electronic contribution only. A clear jump-like feature appears below 18 K. From the fitting with the formula of  $C_p/T = \gamma + \beta \cdot T^2$  for the data of the normal state, one can extract  $\gamma$  and  $\beta$  to be  $35.0 \text{ mJ/mol}\cdot\text{K}^2$  and  $0.215 \text{ mJ/mol}\cdot\text{K}^4$ , respectively, resulting the Debye temperature  $\Theta_D$  of  $\sim 300$  K. The fitted curve is noted in figure 4.3 (b) as a dashed line. The electronic contribution of the specific heat is obtained by subtracting the phonon contribution realized by the fitting described above from the total specific heat. A thermodynamic transition temperature  $T_c$  is estimated to be 16.8 K as the midpoint of the jump-like feature, and the size of the jump is yielded from the linear-extrapolated lines, shown as dashed lines in figure 4.3 (c), to be  $\sim 20.0 \text{ mJ/mol}\cdot\text{K}^2$ . These results is comparable

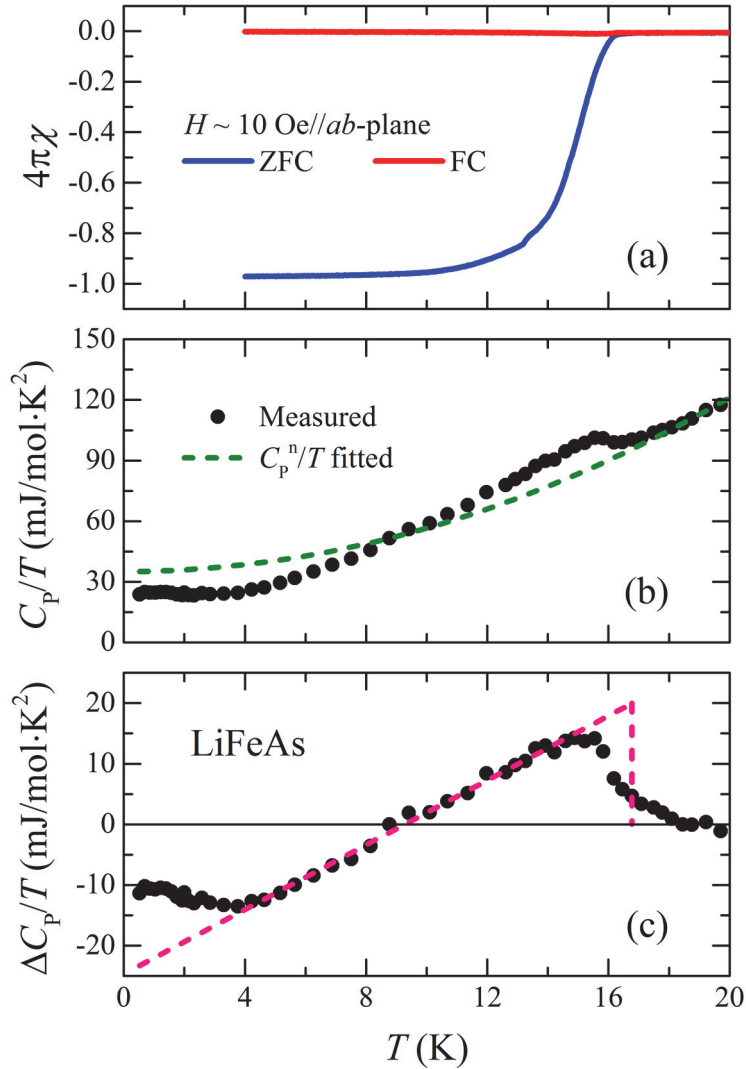
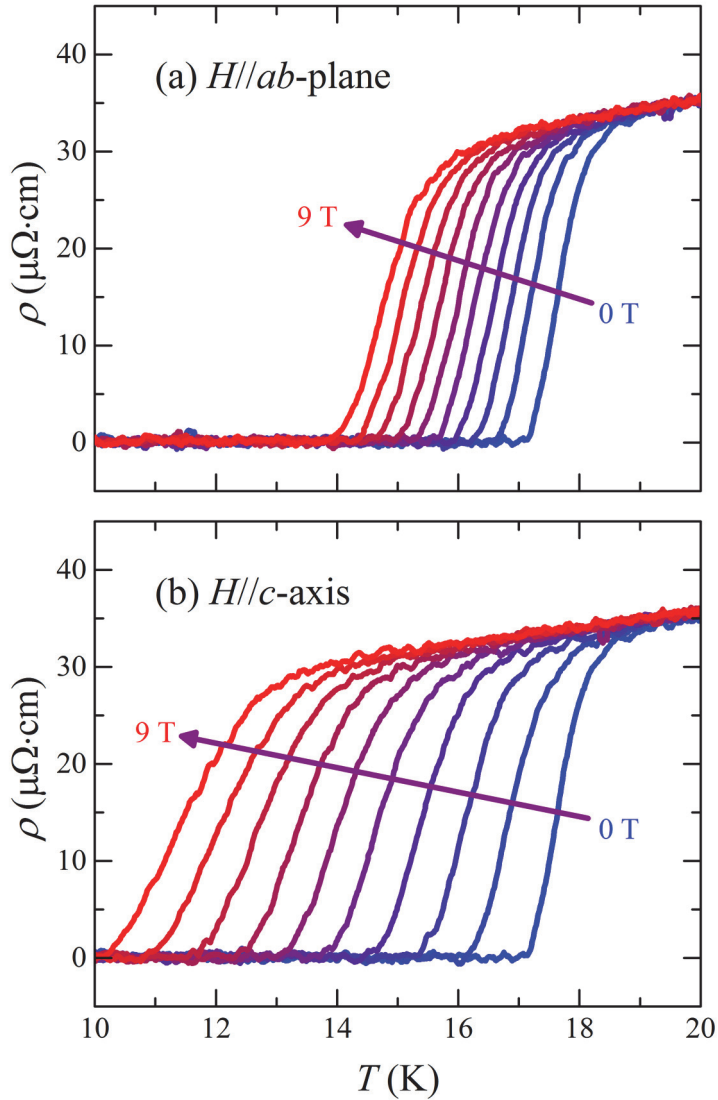


Figure 4.3. (a) DC magnetic susceptibility measured with  $H$  of  $\sim 10$  Oe applied along the  $ab$ -plane at the zero-field-cooled and field-cooled condition. (b) The specific heat of the LiFeAs crystals at zero magnetic fields. The dashed line indicates the normal state specific heat estimated from the fitting explained in the text. (c) The difference of specific heat between the normal and superconducting states.  $T_c$  and the jump in the text are estimated through linear extrapolation shown as dashed lines.



**Figure 4.4.** The resistivity measured under (a)  $H//ab$ -plane and (b)  $H//c$ -axis. The magnetic fields are applied from 0 to 9 T with a step of 1 T.

to the reported values based on the single crystals grown by the self-flux method [16] and clearly evidence the bulk superconductivity in the LiFeAs crystals grown by the Sn-flux method. One notes, furthermore, that the thermodynamic  $T_c$  in the specific

heat is rather consistent with the one from the DC magnetic susceptibility but is a littler lower than the zero-resistivity temperature, as is typical.

### 4.3. Anisotropy of the upper critical fields

The upper critical fields  $H_{c2}$  is realized through the temperature-dependent resistivity measurements under constant magnetic fields applied along both the  $c$ -axis and the  $ab$ -plane. Figure 4.4 (a) and (b) shows the resistivity curves under various magnetic fields applied along the  $ab$ -plane and the  $c$ -axis, respectively. From the resistivity curves,  $T_c$  at each magnetic field is determined by a criterion that 50 % of the normal state resistivity is realized at  $T_c$ . While  $T_c$  decreases with increasing of the magnetic fields as expected, that the superconductivity is more robust for the magnetic fields along the  $ab$ -plane is found, as summarized in figure 4.5, which is a common characteristic of the Fe-based superconductors.  $H_{c2}^c$  and  $H_{c2}^{ab}$ ,  $H_{c2}$  for each magnetic field direction of along the  $c$ -axis and the  $ab$ -plane respectively, are rather linear near  $T_c$  but show different slopes. The  $H_{c2}$  anisotropy, defined as  $\gamma \equiv H_{c2}^{ab}/H_{c2}^c$ , is calculated from the interpolated values for each temperature between the measured points and shown in figure 4.6 for the temperature near  $T_c$ . At the temperature of 15.5 K just below  $T_c$ ,  $\gamma$  is about 2.3, which is clearly smaller than one of  $\text{KFe}_2\text{As}_2$  [14] and 1111 systems [17, 18] whose values are larger than 5 but comparable to one of the most superconducting 122 compounds whose values lie within the range from 2 to 3 [8, 19-21].

The temperature dependence of the  $H_{c2}$  curves is simulated by the Werthamer-Helfand-Hohenberg (WHH) formula [22] based on the values of  $T_c$  and the slopes, and the simulated curves are presented in figure 4.5 as dotted lines. In case the orbital limiting effect is dominant in one main active band, the temperature dependence of

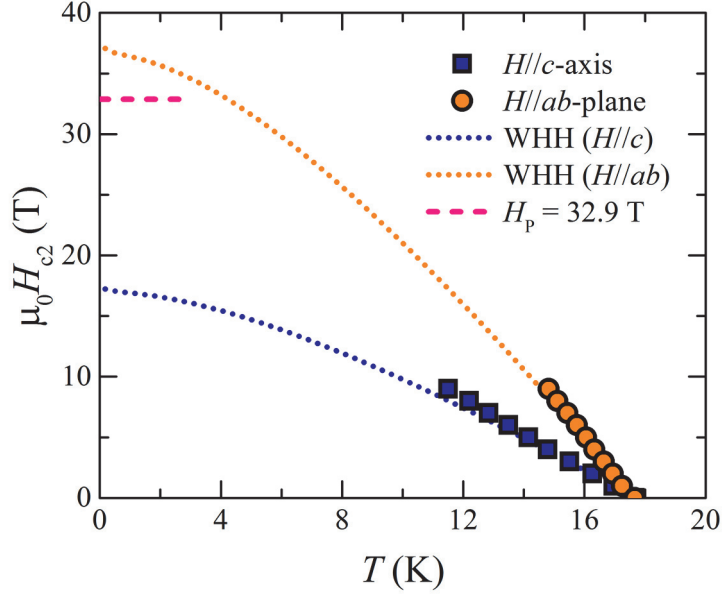


**Figure 4.5.**  $H_{c2}$  curves for both magnetic field directions.  $T_c$  is determined with a 50 % criterion described in the text. The dotted lines represent the simulated curves by the WHH formula without the Maki parameter and the spin-orbit scattering. The Pauli limiting field is shown as dashed line near 0 K.

$H_{c2}$  can be calculated with a reduced formula without the Maki parameter and the spin-orbit scattering effect, and especially one at zero temperature is calculated to be  $H_{c2}^{\text{orb}}(0) = -0.69[dH_{c2}/dT]_{T=T_c}$  if the system is in a dirty limit. Since the  $H_{c2}$  slopes near  $T_c$  are estimated to be  $-1.39$  and  $-2.99$  T/K for  $H//ab$ -plane and  $H//c$ -axis respectively,  $H_{c2}^c(0)$  and  $H_{c2}^{ab}(0)$  are expected to be  $17.2$  and  $36.9$  T respectively, resulting in the coherence length  $\xi_c(0)$  and  $\xi_{ab}(0)$  as  $2.0$  and  $4.4$  nm based on the Ginzburg-Landau relations of  $H_{c2}^c = \Phi_0/2\pi\xi_{ab}^2$  and  $H_{c2}^{ab} = \Phi_0/2\pi\xi_{ab}\xi_c$ . One can note that the expected  $H_{c2}^{ab}(0)$  of  $36.9$  T is relatively larger than the Pauli limiting field which is simply defined as  $H_p = 1.86T_c$  for a weakly

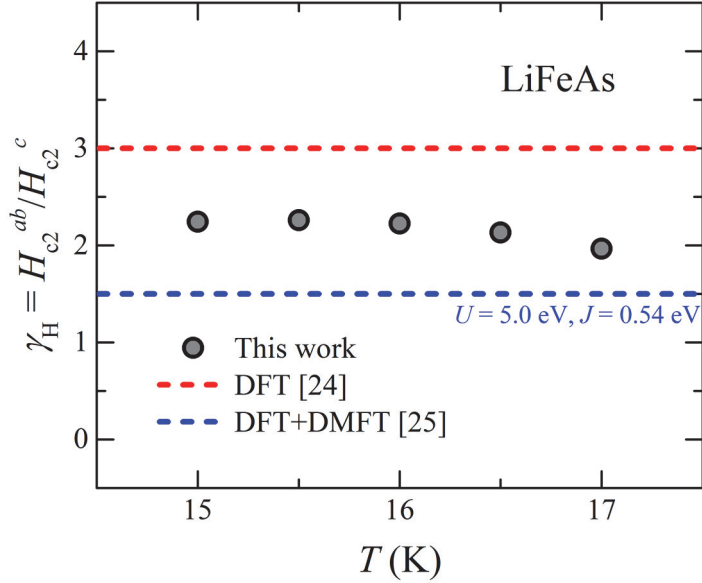


**Figure 4.6.** The  $H_{c2}$  anisotropy near  $T_c$ . The values are obtained upon interpolation of the  $H_{c2}$  curves presented in figure 4.5. The dashed lines represent the predictions from the theoretical investigations [24, 25].

coupled BCS superconductors and expected as 32.9 T for these results with  $T_c$  of 17.7 K. Since the magnetic field scales of the orbital limiting effect and the Pauli limiting effect are competitive with each other, the combined theory for both pair breaking mechanisms has to be considered to understand  $H_{c2}$  of LiFeAs. By the further experiments on these single crystals performed at the high magnetic field facility, the pair breaking mechanism of LiFeAs is revealed in detail [23].

According to the Ginzburg-Landau relations mentioned previously, the  $H_{c2}$  anisotropy is close to being the same as the anisotropy of the coherence length anisotropy as well as one of the penetration depth, particularly near  $T_c$  where the Ginzburg-Landau equations apply and the orbital limiting effect is dominant to determine  $H_{c2}$ . The  $H_{c2}$  anisotropy of 2.3 near  $T_c$ , therefore, implies that the zero-

temperature anisotropy for the coherence length and the penetration depth are also close to 2.3. At that moment, based on the first-principle calculations with GGA approximation and the assumption of isotropic relaxation time and its independence of the velocity of the conduction electrons, the penetration depth anisotropy,  $\gamma_\lambda(0)$ , of various Fe-based superconductors has been predicted [24]. According to their results, one of BaFe<sub>2</sub>As<sub>2</sub> and LiFeAs are relatively small as  $\sim 3$  while one of LaOFeAs is much bigger as  $\sim 10$ . In a later effort to include the effects of electron correlation by incorporating the dynamic mean field theory (DMFT) and the density functional theory (DFT) [25],  $\gamma_\lambda(0)$  of LiFeAs has been predicted to become smaller as  $\sim 1.5$ . The observation of a moderate  $H_{c2}$  anisotropy of 2.3 in the LiFeAs single crystal grown by the Sn-flux method is a bit smaller than the band calculation results based on the GGA approximation but also still larger than the prediction based on the calculation including the electron correlation. This result indicates that the electron correlation has to be included for the theoretical method to study LiFeAs but also the strength of the correlation may be smaller than the value introduced in the previous reports,  $U = 5.0$  and  $J = 0.54$  eV [25]. After these early studies, experimental and theoretical investigations are combined to understand the system further, and the recent report based on the angle-resolved photo-emission spectroscopy and the calculation with DMFT suggests the values of  $U = 5.0$  and  $J = 0.8$  eV [26].

#### 4.4. Superconductivity in a clean-limit

For further investigation, the single crystal growth condition is modified to prepare the single crystals with various impurity scattering level. The crystals annealed in the flux right after the growth and the crystals centrifuged at lower

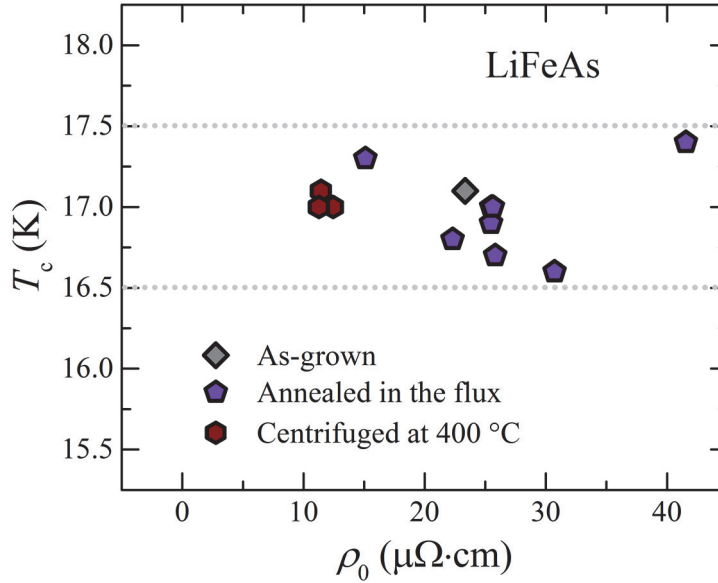


**Figure 4.7.**  $T_c$  realized from the resistivity of crystals with various  $\rho_0$  prepared from the modified growth conditions. Based on the growth condition, the scatters are categorized into 3 groups. Diamond, pentagons, and hexagons represent samples grown by the as-grown condition, the annealing condition, and the low-temperature centrifuge condition, respectively, described in chapter 3.

temperature of 400 °C are prepared and their resistivity is measured. Figure 4.7 summarizes the transition temperature  $T_c$ , determined as the temperature where the zero resistivity is realized, and the residual resistivity  $\rho_0$ , obtained from the extrapolation of the normal state resistivity, of several crystal pieces. As shown in figure 4.7,  $T_c$  is not much changed and realized within the temperature range between 16.5 and 17.5 K while  $\rho_0$ , which indicates the impurity scattering level, varies from  $\sim 10$  to  $\sim 40 \mu\Omega\cdot\text{cm}$ , and any clear correlation between  $T_c$  and  $\rho_0$  is not observed. Based on the robustness of  $T_c$  upon  $\rho_0$  within this experimental

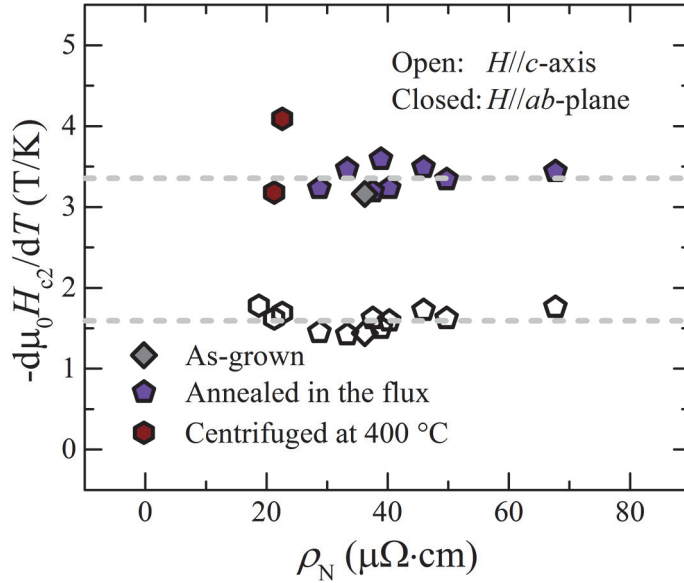


**Figure 4.8.** The slope of  $H_{c2}$  near  $T_c$  for the crystals with various  $\rho_0$ . The open and closed scatters indicate the slope for  $H//c$ -axis and  $H//ab$ -plane, respectively. The dashed lines are simple guidelines.

limit, it is expected that these crystal pieces with various  $\rho_0$  have superconducting properties, such as  $H_{c2}$ , from the same origin with the as-grown LiFeAs crystals and the properties don't change much although more impurity scatterings are introduced.

$H_{c2}$  of these pieces is also realized from the resistivity under the magnetic fields and the  $H_{c2}$  slopes near  $T_c$  are extracted for each piece and the direction of the magnetic fields by the same manner explained earlier. The results are summarized in figure 4.8 with respect to the normal state resistivity  $\rho_N$  realized at the temperature right above  $T_c$ . For the both of  $H//ab$ -plane and  $H//c$ -axis, the slopes seem to be independent to  $\rho_N$ , similar to the tendency of  $T_c$  with respect to  $\rho_0$ . The  $H_{c2}$  slope near  $T_c$ , on the other hand, relates to  $N(\epsilon_F)$ , the density of states at the Fermi level, as well as  $\rho_N$ , which is represented as  $|dH_{c2}/dT|_{T=T_c} =$

$(4eck_B/\pi)N(\epsilon_F)\rho_N$  while the system is in a dirty-limit of the WHH model [23]. This theoretical prediction is in contrast with the results in the LiFeAs crystals with various  $\rho_N$ . Although the WHH model is based on the conventional 1-band superconductor, the  $H_{c2}$  slope for  $H//ab$ -plane may be able to be interpreted by the WHH model since the LiFeAs system has the layered structure and the intra-layer property is more important to understand the pair-breaking mechanism. It is also evidenced by the temperature dependence of  $H_{c2}^{ab}$  which agrees well with the theoretical expectation based on the WHH formula with finite Maki parameter and spin-orbit scattering [23]. The disagreement between the theoretical prediction in the WHH model and the experimental results in the LiFeAs single crystals, therefore, indicates that LiFeAs is not the dirty-limit superconductor. In addition, the mean-free path  $l_{ab}$  calculated from  $\rho_N$  is laid within the range from 3 to 12 nm while the coherence length  $\xi_{ab}$  is  $\sim 3.98$  nm expected from  $H_{c2}(0)$ , implying that the system is in a clean-limit, where  $l_{ab} \gg \xi_{ab}$ , rather than the dirty-limit,  $l_{ab} \ll \xi_{ab}$ .

#### 4.5. Summary

In this chapter, the physical properties, including the electrical resistivity, the DC magnetic susceptibility, the specific heat, and the upper critical fields, of the LiFeAs single crystal grown by the Sn-flux method are presented. The onset transition temperature of 18.2 K and the narrow transition width of 1.1 K indicate the high quality of the crystals. 100 % of the superconducting shielding fraction in the ZFC magnetic susceptibility and the clear jump-like feature in the specific heat evidence the bulk superconductivity of the crystals. From the  $H_{c2}$  measurements near  $T_c$ , one can extract the anisotropy and the slopes, and the modest anisotropy of  $\sim 2.3$  is realized. This anisotropy value is a moderate value between the band

calculation results based on the GGA approximation and the one from the DMFT+DFT calculation, supporting the electron correlation in the system. In addition, it is claimed that the LiFeAs system is in the clean-limit rather than the dirty-limit based on the robustness of the  $H_{c2}$  slopes with respect to  $\rho_N$  representing the impurity scattering level in the crystals.

#### 4.6. References

- [1] Y. Kamihara *et al.*, J. Am. Chem. Soc. **130**, 3296 (2008)
- [2] X. C. Wang *et al.*, Solid State. Commun. **148**, 538 (2008)
- [3] J. H. Tapp *et al.*, Phys. Rev. B **78**, 060505 (2008)
- [4] M. J. Pitcher *et al.*, Chem. Commun. **41**, 5918 (2008)
- [5] D. S. Inosov *et al.*, Phys. Rev. Lett. **104**, 187001 (2010)
- [6] Y. J. Song *et al.*, Appl. Phys. Lett. **96**, 212508 (2010)
- [7] B. Lee *et al.*, Europhys. Lett. **91**, 67002 (2010)
- [8] N. Ni *et al.*, Phys. Rev. B **78**, 014507 (2008)
- [9] J. S. Kim *et al.*, J. Phys.: Condens. Matter **21**, 102203 (2009)
- [10] E. Dengler *et al.*, Phys. Rev. B **81**, 024406 (2010)
- [11] N. Harrison *et al.*, J. Phys.: Condens. Matter **21**, 322202 (2009)
- [12] S. J. Zhang *et al.*, Phys. Rev. B **80**, 014506 (2009)
- [13] H. Chen *et al.*, Europhys. Lett. **85**, 17006 (2009)
- [14] T. Terashima *et al.*, J. Phys. Soc. Jpn. **78**, 063702 (2009)
- [15] K. Hashimoto *et al.*, Phys. Rev. B **82**, 014526 (2010)
- [16] F. Wei *et al.*, Phys. Rev. B **81**, 134527 (2010)
- [17] J. Jaroszynski *et al.*, Phys. Rev. B **78**, 174523 (2008)
- [18] U. Welp *et al.*, Phys. Rev. B **78**, 140510 (2008)

- [19] S. Khim *et al.*, *Physica C* **470**, S317 (2010)
- [20] H. Q. Yuan *et al.*, *Nature* **457**, 565 (2009)
- [21] S. A. Baily *et al.*, *Phys. Rev. Lett.* **102**, 117004 (2009)
- [22] N. R. Werthamer *et al.*, *Phys. Rev.* 147, **295** (1966)
- [23] S. Khim *et al.*, *Phys. Rev. B* **84**, 104502 (2011)
- [24] H. Nakamura *et al.*, *J. Phys. Soc. Jpn.* **78**, 123712 (2009)
- [25] Y. J. Song *et al.*, *Europhys. Lett.* **94**, 57008 (2011)
- [26] G. Lee *et al.*, *Phys. Rev. Lett.* **109**, 177001 (2012)

## 5. Fermi energy level shift in $\text{Li}(\text{Fe}_{1-x}\text{Co}_x)\text{As}$

### 5.1. Introduction

Since the discovery of the  $\text{ReOFeAs}$  series ( $\text{Re}$  = rare earth) in early 2008, several new compounds including  $\text{AeFe}_2\text{As}_2$  ( $\text{Ae}$  = alkaline earth),  $\text{FeCh}$  ( $\text{Ch}$  = chalcogen), and  $\text{AFeAs}$  ( $\text{A}$  = alkali metal) have been found subsequently to join the Fe-based superconductor family [1-4]. As discussed earlier in chapter 1, most of pristine compounds in the superconducting family show a spin-density-wave (SDW) transition in their ground state, and the SDW transition is suppressed by chemical doping or external pressure while the superconductivity arises in the vicinity of phase space where the SDW ground state disappeared [5-9].  $\text{LiFeAs}$ , on the other hand, has a superconducting ground state with  $T_c > 10$  K instead of a SDW one without any chemical doping or external pressure [2-4]. In this regard,  $\text{LiFeAs}$  would be one of very unique members of the Fe-based superconductor family [1].

To understand the superconductivity of  $\text{LiFeAs}$  further, angle-resolved photoemission spectroscopy (ARPES) studies and associated theoretical calculation of the band structure reveal that the Fermi surfaces of  $\text{LiFeAs}$  consist of 2 electron-pockets and 3 hole-pockets, indicating that the system is a compensated metal [10, 11]. The earlier ARPES studies have focused on the imbalance between the 2 small hole-pockets and the 2 large electron-pockets since the superconductivity of the other Fe-based superconductors is believed to be induced when the balance between hole- and electron-pockets which provides the nesting condition for the SDW transition in the pristine compounds is broken by the shift of the Fermi energy level induced by introduction of additional charge carriers via chemical doping [10]. The authors

interpreted this imbalance in the band structure of LiFeAs as an “electron-over-doped-like” property, which has been supported by several experimental results. Hall coefficients of LiFeAs, for example, have been reported to be clearly negative in the temperature range above the superconducting transition [12, 13], indicating the contribution from the electron carriers is dominant in the transport property of LiFeAs. In addition, the superconducting transition is suppressed monotonically by the increase of external pressure [14-16], which is similar to the pressure dependence of other over-doped compounds in the Fe-based superconductor family [1]. Consistent with this interpretation, studies on the Li(Fe<sub>1-x</sub>Co<sub>x</sub>)As series using either polycrystalline specimens or single crystals grown by the self-flux method present the monotonic decrease of  $T_c$  with the increase of the additional electron carriers introduced by the Co substitution [17-19]. The ARPES study on the series, moreover, confirms that the electron-pockets become systematically larger with Co doping [18].

Due to the presence of the Li ions, which is highly volatile and easily oxidized in air, it had been expected to be difficult to grow the high quality single crystals of LiFeAs and related compounds. The Sn-flux method is, however, reported to be successful in the growth of high quality single crystals [20]. Herein, the successful growth of the Li(Fe<sub>1-x</sub>Co<sub>x</sub>)As single crystals with the Co doping level up to  $x = 0.1$  by the Sn-flux method is presented. Based on the temperature dependence of the resistivity measured in the crystals, it is suggested that the Co content act as impurities. In addition, the  $T^2$  dependence of the resistivity increases abruptly at the higher Co content of  $x = 0.06$  and  $0.08$ , implying that the hole-pockets become smaller while the Fermi energy level is shifted by the introduction of additional electron carrier by the Co-doping. This observation that the transport properties vary sensitively by the change of the Fermi surface suggests that the Li(Fe<sub>1-x</sub>Co<sub>x</sub>)As

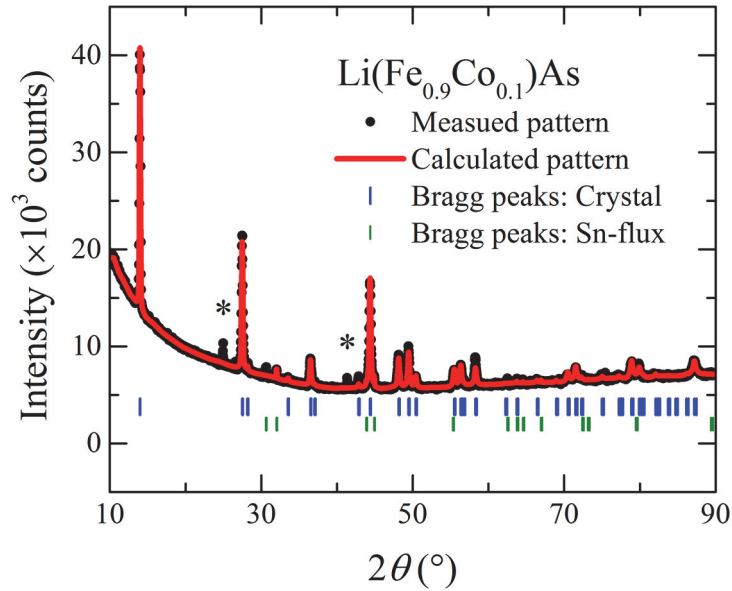


**Figure 5.1. X-ray diffraction pattern of the powder obtained from the Li(Fe<sub>0.9</sub>Co<sub>0.1</sub>)As single crystals. The measured pattern, shown as circles, is refined with 2 structural phases of LiFeAs and Sn. The solid line represents the calculated pattern while the longer (upper and blue) and shorter (lower and green) ticks indicate the Bragg peak positions for the LiFeAs and Sn phases respectively.**

system should be understood as compensated metals where both hole- and electron-pockets contribute significantly to their transport properties in the normal state even up to the Co doping level of  $x = 0.08$ , similar to the pristine compound LiFeAs.

## 5.2. X-ray diffraction

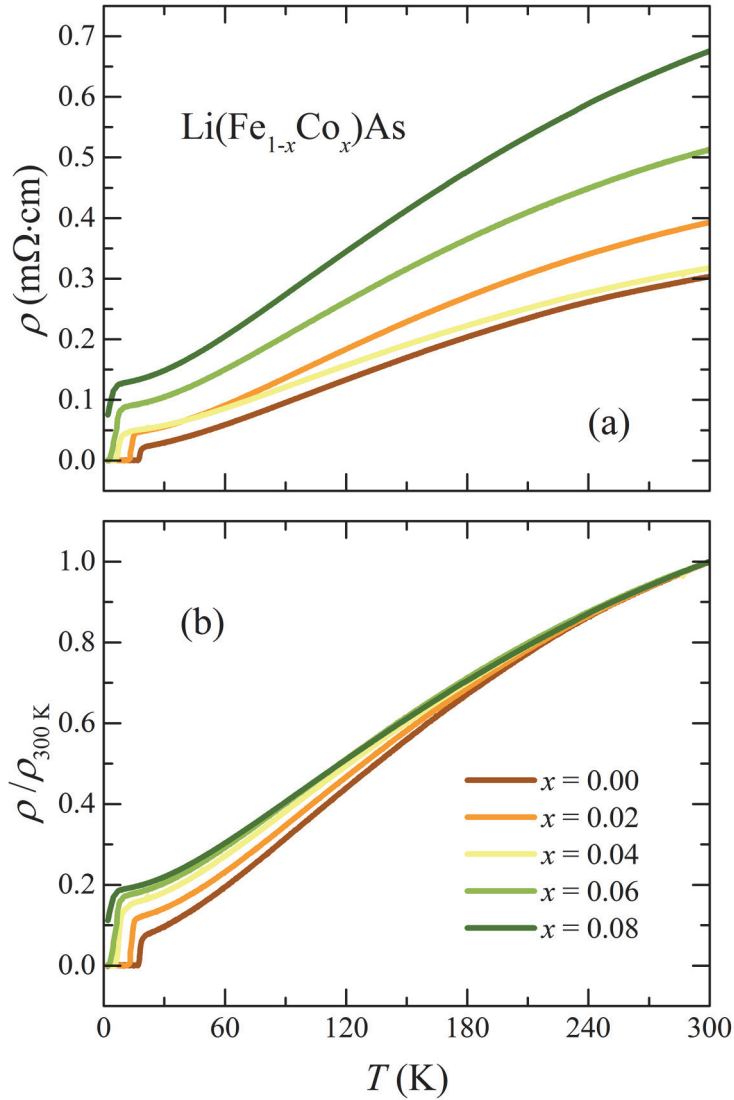
Figure 5.1 presents the powder X-ray diffraction pattern of the Li(Fe<sub>0.9</sub>Co<sub>0.1</sub>)As single crystals. The measured diffraction pattern, presented as the circles in the figure, is refined by the FullProf Suite program and the calculated pattern is presented in the

figure as the solid line. Since there is small amount of residual Sn at the surface of the crystals, the phase with the structure of Sn is included as a minor secondary phase into the refinement as well as one with the structure of LiFeAs. Bragg peak positions from the phase of the crystal sample and the residual flux are shown as long and short ticks, respectively, at the bottom of figure 5.1. The refinements with the  $R_{wp}$  factor of 17.5 result the lattice constants of the  $\text{Li}(\text{Fe}_{0.9}\text{Co}_{0.1})\text{As}$  phase as  $a = 3.7752(8)$  and  $c = 6.3252(1)$  Å, which are consistent with the reported values,  $a = 3.78105(1)$  and  $c = 6.32658(3)$  Å of the polycrystalline specimens [17]. The consistency of the lattice constants between this work and the previous report supports that the residual Sn phase exists at the crystal surfaces mostly, not inside the crystal.

Peaks which are not identified with the LiFeAs and Sn phases and noted with asterisks are known to represent the oxidized fraction of the crystals. Although a quartz capillary has been employed to minimize the air exposure, it seems that small amount of air penetrated into the powder during the sealing procedure of the capillary. Those peaks, however, indicating the degradation of the crystals didn't become larger during the measurement with the running time of ~ 20 h, which means that the air exposure happened only at the moment of the sealing procedure and there was no more degradation after the sealing.

### **5.3. Doping dependence of RRR and $T_c$**

The temperature dependence of the resistivity and the normalized one with the resistivity at 300 K are presented in figure 5.2 (a) and (b) respectively. The resistivity measurements were performed with the temperature range from 2 K to 300 K for the  $\text{Li}(\text{Fe}_{1-x}\text{Co}_x)\text{As}$  crystals with  $x = 0.00, 0.02, 0.04, 0.06,$  and  $0.08$ . Since the crystals



**Figure 5.2.** The temperature dependence of (a) the resistivity and (b) the normalized resistivity of the  $\text{Li}(\text{Fe}_{1-x}\text{Co}_x)\text{As}$  single crystals.

with  $x = 0.10$  have not exhibited a superconducting transition down to 2 K, those specimens would not be discussed further in this chapter. The resistivity of all samples decreases monotonically without any other anomaly or transition-like

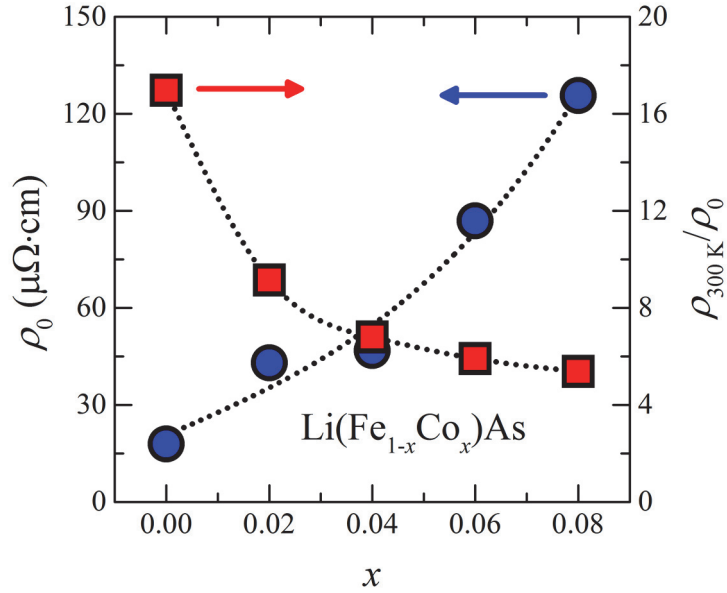


**Figure 5.3.** Extracted  $\rho_0$  and RRR with respect to  $x$ . Blue circles with the left axis and red squares with the right axis represent  $\rho_0$  and RRR, respectively. A formula of  $\rho = \rho_0 + A \cdot T^2$  is employed to extract  $\rho_0$ .

feature except the superconducting transition. It is noteworthy, moreover, that the residual resistivity  $\rho_0$ , as well as a residual resistivity ratio to the room temperature resistivity (RRR) which is defined as  $\text{RRR} = \rho_{300\text{K}}/\rho_0$ , increases systematically with the Co content. The values of  $\rho_0$  and RRR are summarized in the figure 5.3 with respect to  $x$ . In these figures, the residual resistivity is extracted based on the fitting with a formula of the Fermi-liquid-like temperature dependence of the resistivity,  $\rho = \rho_0 + A \cdot T^2$ , in the temperature range of 20 K from the temperature right above the transition temperature  $T_c$ . The resultant RRR value of LiFeAs is  $\sim 17$ , which is a bit lower than those of the single crystals grown by the self-flux method [12, 13, 18]. With the increase of the Co content, the RRR value decreases monotonically, reaching 5.4 at  $x = 0.08$ .

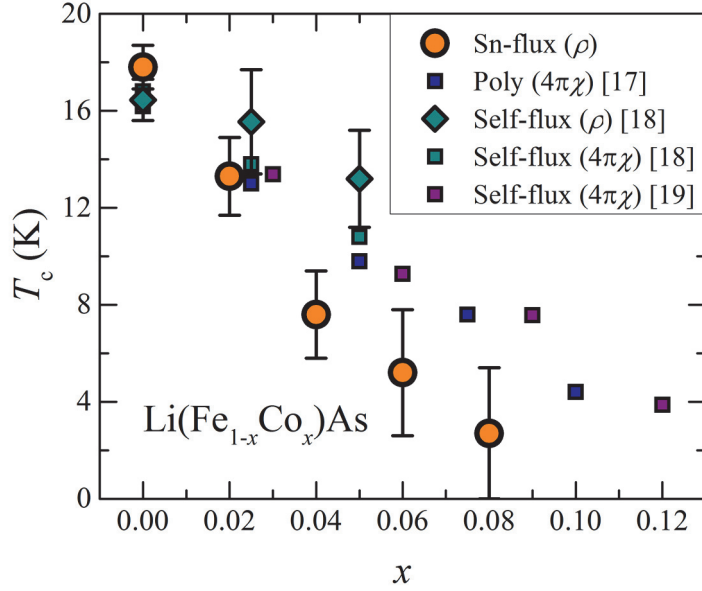


**Figure 5.4. Doping dependence of  $T_c$  of the  $\text{Li}(\text{Fe}_{1-x}\text{Co}_x)\text{As}$  single crystals. To compare, the doping dependence from the other results are shown in the figure. Circles and diamonds with error bars represent  $T_c$  determined from the resistivity of the crystals in this work and the self-flux crystals [18], respectively, while squares indicate  $T_c$  from the magnetic susceptibility of polycrystalline specimens and the self-flux crystals [17-19]. The criteria to determine  $T_c$  and the error bars are described in the text.**

Figure 5.4 summarizes the doping dependence of  $T_c$  for the single crystals grown by the Sn-flux method studied in this work as well as one for the other specimens including the polycrystalline samples and the single crystals grown by the self-flux method [17-19]. In this work,  $T_c$  is determined to be the mid-point between the temperature where 90 % of the normal state resistivity is realized ( $T_c^{90\%}$ ) and the temperature where zero resistivity is realized ( $T_c^{zero}$ ), and the transition width is defined as the difference between  $T_c^{90\%}$  and  $T_c^{zero}$ . For the single crystals

of  $x = 0.08$ ,  $T_c^{zero}$  is assumed to be 0 K since zero resistivity is not realized within the experimental limit of the temperature, down to 2 K.  $T_c$  and the transition width of the crystals grown by the self-flux method, shown in figure 5.4, are also determined with same criteria [18]. In addition, the transition temperature estimated from the magnetic susceptibility measurements are also plotted together for both of polycrystalline specimens and the other single crystals [17-19].

The doping dependence of  $T_c$  summarized in figure 5.4 for all the samples shows a monotonic decrease with increasing of  $x$  without any plateau-like feature [17-19]. In the comparison with other results, the single crystals grown by the Sn-flux method and studied in this work show a little steeper suppression of  $T_c$  than the other polycrystalline or single crystal samples, indicating the actual Co content may be a bit higher than the nominal one. On the other hand, the transition widths of the crystals in this work are narrower or approximately equal to those of the other crystals. Specifically, the transition widths of the Sn-flux crystals with  $x = 0.00, 0.02,$  and  $0.04$  are 1.8, 3.2, and 3.6 K respectively while the transition widths of the self-flux crystals with  $x = 0.00, 0.025,$  and  $0.05$  are 1.7, 4.3, and 4 K respectively [18]. Additionally,  $T_c$  of  $\sim 17.8$  K in the un-doped LiFeAs crystal in this work is significantly higher than one of  $\sim 16.5$  K in the LiFeAs crystal grown by the self-flux method [18]. These properties indicate the high quality of the single crystals grown by the Sn-flux method which is comparable to, or even better than in some respect, one of the single crystals grown by the self-flux method. The high quality of the Sn-flux crystals provides an improved opportunity to investigate the intrinsic transport properties of the  $\text{Li}(\text{Fe}_{1-x}\text{Co}_x)\text{As}$  series.

It is important to note that the systematic decrease of RRR in the series with increasing of  $x$ , presented in figure 5.3, contrasts strongly with other Fe-based

superconductor family such as  $(\text{Ba}_{1-x}\text{K}_x)\text{Fe}_2\text{As}_2$  and  $\text{Ba}(\text{Fe}_{1-x}\text{Co}_x)_2\text{As}_2$ , in which RRR increases with the increase of the doping level [5-8]. This contrast seems to be due to the difference between the spin fluctuation in the LiFeAs system and one in the others. According to the previous study of the Hall effect in  $\text{Ba}(\text{Fe}_{1-x}\text{Co}_x)_2\text{As}_2$  series, the electron-hole scattering associated with the spin fluctuations has been suggested to exist in un-doped and under-doped regimes, resulting in the increase of RRR with an increase of the doping level which reduces the spin fluctuation by the imbalance between the hole- and electron -pockets [7]. On the other hand, in LiFeAs, the hole- and electron-pockets in the Fermi surfaces indeed exist at the  $\Gamma$  and  $M$  points, respectively, while the antiferromagnetic spin fluctuations have been observed between the  $\Gamma$  and  $X$  points [21]. The doping dependence of RRR in the series, therefore, suggests that the inter-band scattering associated with the spin fluctuations may not play an important role in the transport properties in the normal state of the series. Instead, the characteristic of each band constituting the Fermi surfaces has to influence the transport properties more than the inter-band scattering. In this regard, the variation of the Fermi surface topology induced by the Co doping can be important to understand the transport properties of  $\text{Li}(\text{Fe}_{1-x}\text{Co}_x)\text{As}$ .

#### **5.4. Fermi liquid behavior and the increase of $A$**

The electrical resistivity of a multi-band metal can be described effectively with a simple parallel-resistor model,  $\rho = (\sum \rho_i^{-1})^{-1}$ . If the multi-band system is the Fermi-liquid one and the resistivity contribution of each band also follows the Fermi-liquid behavior, the  $T^2$  coefficient  $A$  in the total resistivity showing the Fermi-liquid behavior of  $\rho = \rho_0 + A \cdot T^2$  is understood to consist of the residual resistivity  $\rho_{0,i}$  and the  $T^2$  coefficient  $A_i$  from each band with the assumption of

the resistivity of each band which can be described with the Fermi-liquid formula. When the  $T^2$  coefficient is much larger than the residual resistivity,  $A \cdot T^2 \gg \rho_0$ , one can assume that the  $T^2$  coefficient of the total resistivity is determined by the simple parallel-resistor model,  $A \approx (\sum A_i^{-1})^{-1}$  while the coefficient would be expressed as a much more complicated formula consisting of the combination of  $\rho_{0,i}$  and  $A_i$  when the system is on the other limit of  $A \cdot T^2 \ll \rho_0$ . Since RRR of LiFeAs and the Co-doped series studied in this work is realized to be from 5 to 17 as presented earlier, one can expect to understand the Li(Fe<sub>1-x</sub>Co<sub>x</sub>)As series being in the limit of  $A \cdot T^2 \gg \rho_0$  up to the doping level of  $x = 0.08$ .

On the other hand, the resistivity should be sensitively determined by the mobility of both the hole- and electron-bands in the compensated metal system such as LiFeAs, having  $n_h \approx n_e$ , since the resistivity also can be described effectively as  $\rho = [e \cdot (n_e \mu_e + n_h \mu_h)]^{-1}$  within the 2-band approximation, where  $n_e$  and  $\mu_e$  represent the carrier density and the mobility of the electron carrier respectively while  $n_h$  and  $\mu_h$  represent those of the hole carrier, as well as the expression based on the Fermi-liquid formula discussed above. It is reported that the ratio between hole and electron mobility,  $\mu_e/\mu_h$ , in LiFeAs is about 1.6 within the 2-band approximation from the Hall effect measurements [13]. Both of the hole- and electron-bands, therefore, is expected to contribute to the total resistivity in LiFeAs, and also in the related compounds such as the Li(Fe<sub>1-x</sub>Co<sub>x</sub>)As series if the system still maintains the nearly-compensated band structure upon the doping. The coefficient  $A$ , moreover, is expected to be sensitive to the change of both the hole- and electron-bands in such compensated systems.

Figure 5.5 shows the  $T^2$  dependence of the resistivity curves. The open circles represent the measured resistivity and the solid lines represent the fitted curve in the

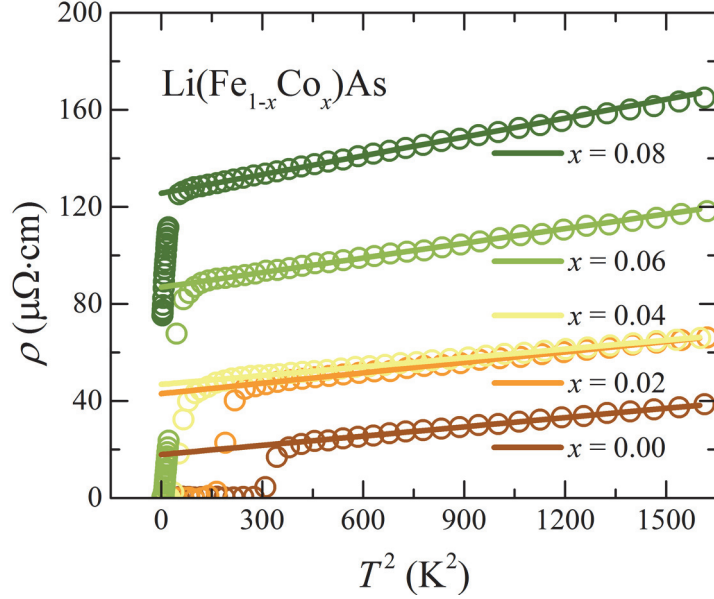


**Figure 5.5.** The  $T^2$  dependence of the resistivity curves. Open circles represent the measured resistivity of the  $\text{Li}(\text{Fe}_{1-x}\text{Co}_x)\text{As}$  single crystals and the solid lines indicate the fit with the formula of  $\rho = \rho_0 + A \cdot T^2$  in the temperature window of 20 K, described in the text.

temperature window of 20 K as mentioned earlier. Figure 5.6 displays the  $A$  values of the series obtained from the fit with the  $T^2$  dependence. From the variation of  $A$  upon the temperature window being varied from 5 to 25 K, the error bars in figure 5.6 are estimated. As presented in the figure,  $A$  shows an abrupt increase at the Co content of  $x = 0.06$ . Since the  $\text{Li}(\text{Fe}_{1-x}\text{Co}_x)\text{As}$  series show small  $\rho_0$  and large RRR, the abrupt increase of  $A$  may reflect a change of the Fermi surfaces.

For a single cylindrical 2-dimensional Fermi surface, the coefficient  $A$  is known to be  $A_i \approx (8\pi^3 a c k_B^2 / e^2 \hbar^3) \cdot (m_i^{*2} / k_F^3)$  [22], which implies that the decrease of  $k_F$  induces the increase of  $A$  for the specific band while the increase of  $k_F$  does the decrease of  $A$ . The Fermi energy level shift induced by the

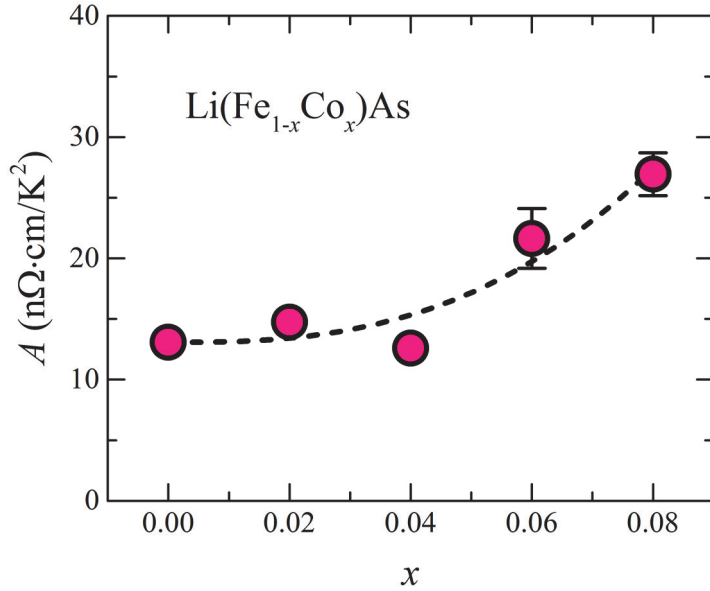


**Figure 5.6. Doping dependence of the coefficient  $A$ , estimated from the fitting explained in the text. The error bars are estimated from the variation of  $A$ . The dashed line is a guide to the eye.**

introduction of additional electron carriers, furthermore, results the shrinkage of the hole-pockets as well as the enlargement of the electron-pockets, therefore it is expected that the coefficient of the hole-bands  $A_h$  is increased and the coefficient of the electron-bands  $A_e$  is decreased by the electron-doping.

According to the previous experimental and theoretical studies on the bands structure of LiFeAs, 2 small hole-pockets at the  $\Gamma$  point have flat tops at a slightly higher level than the Fermi energy level [10, 11]. It is observed that the 2 hole-pockets shrink and the bottom of the 2 electron bands at the  $M$  point becomes deeper with the Co content of  $x = 0.05$  [18], implying that the Fermi energy level moves toward the top of the hole-pockets with accompanying shrinkage of the hole-pockets and enlargement of the electron-pockets. Since the band structure of the Fe-based

superconductors is known to be rigid upon the chemical substitution with additional charge carrier, such as Co- and K-doping in BaFe<sub>2</sub>As<sub>2</sub> [23], one can conclude that the band structure of the Li(Fe<sub>1-x</sub>Co<sub>x</sub>)As series is almost same with one of LiFeAs except that the Fermi energy level is shifted with the additional electron carriers.

In this respect, the coefficient  $A_h$  and  $A_e$  are expected to be increased and decreased, respectively, by the Co-doping from the original value of the pristine compound, and these changes of  $A_h$  and  $A_e$  may cause the increase of the coefficient  $A$  in the total resistivity. From the previous experimental and theoretical investigation of the band structure of LiFeAs [10, 11], the one of the hole-bands is much narrower than the electron-bands, which means the change of  $k_F$  in the narrower hole-bands is greater than the one in the electron-bands while the Fermi energy level is shifted and the bands structure is rigid. The difference of the band width of the hole- and electron-bands, therefore, results that the change of  $A$  is mainly contributed by the shrinkage of the hole-bands instead of the enlargement of the electron-bands.

Even though the scenario discussed above is consistent with the experimental observation of this chapter, some questions are still remaining. For example, the previous discussion is based on the assumption that the hole- and electron-bands of the series are fully 2-dimensional. For the band with 3-dimensional characters, however, the coefficient  $A$  is known to be  $A \propto 1/k_F^6$  [22]. It is expected, therefore, that the coefficient  $A$  would be increased when the Fermi vector  $k_F$  is decreased and vice versa, even if one consider the 3-dimensional character of the band such as the warping.

The Kadowaki-Woods relation, on the other hand, between the coefficient  $A$  and the electronic specific heat  $\gamma_N$  is  $\gamma_N = a_{KW} \cdot A^2$  while the ratio  $a_{KW}$  is

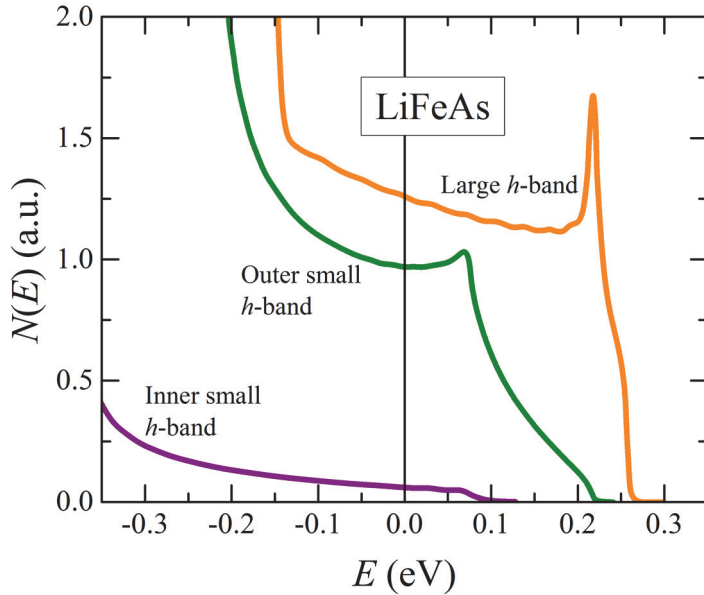


**Figure 5.7.** The partial density of states near the Fermi energy level calculated for the 3 hole-bands of LiFeAs [11]. The calculation is based on the fully self-consistent density functional theory. The energy indicate one from the Fermi level and the vertical line indicate the Fermi level. The top curve represents the large hole-band while the middle and bottom curves represent the outer and inner ones between the 2 small hole-bands.

determined by the detailed band structure of specific system [22]. Since the electronic specific heat is known to be proportional to the density of states at the Fermi level, one can predict that the increase of the density of states induces the increase of  $A$ . In the above discussion about the increase of  $A$  due to the decrease of  $k_F$ , however, the density of states is assumed to be not changed and the influence is not considered. To confirm the assumption, the partial density of states (PDOS) near the Fermi energy level is calculated for the 3 hole-bands of LiFeAs, based on the fully self-consistent density functional theory [11]. Figure 5.7 shows the

calculated PDOS of the 3 hole-bands. Except one of the large band, PDOS of the 2 small bands is not much varying with respect to the energy. Within the rigid band model, therefore, PDOS of hole-bands is expected not to be changed much by the Co content. It is concluded, furthermore, that the increase of the coefficient  $A$  is not caused by the increase of the density of states.

These results show that the transport properties at the normal state of the  $\text{Li}(\text{Fe}_{1-x}\text{Co}_x)\text{As}$  series depend on the characteristic of both hole- and electron-pockets at least in the Co content of  $x \leq 0.08$ . It is worth to point out that the actual significance of the complicated band structure in the transport properties has not been fully recognized for  $\text{Li}(\text{Fe}_{1-x}\text{Co}_x)\text{As}$  although the band structure of  $\text{LiFeAs}$  has been suggested previously to be the compensated metal. Even though the introduction of additional electrons induces a small imbalance between the hole and electron carrier density, the comparable hole and electron mobility values seem to ensure the multi-band characters in the transport properties including the resistivity investigated in this chapter as well as the reported Hall coefficient [13]. In addition, a study of the normal state transport properties in the  $\text{Li}(\text{Fe}_{1-x}\text{Co}_x)\text{As}$  single crystals with a broad doping range is likely to provide more evidences to understand the evolution of the Fermi surfaces with the introduction of additional electron carriers.

## 5.5. Summary

In this chapter, a comprehensive study of the transport properties in the high quality single crystals of the  $\text{Li}(\text{Fe}_{1-x}\text{Co}_x)\text{As}$  series grown by the Sn-flux method is presented. The superconducting phase diagram with respect to the Co content is obtained from the resistivity measurements.  $T_c$  is suppressed and RRR decreases as the Co doping level increases. It is found that the resistivity of the series shows the

Fermi-liquid-like behavior in the low temperature region and an abrupt increase of the  $T^2$  coefficient  $A$  is observed around the Co content of  $x = 0.06$ . The sudden change of  $A$  implies the enhancements of the density of states at the Fermi surface, which is expected to be due to the shift of the Fermi energy level by the introduction of electron carriers via the Co doping. The results of this work signify that the transport properties of the Li(Fe<sub>1-x</sub>Co<sub>x</sub>)As series are determined by the characteristic of both hole- and electron-bands, supporting that these series should be interpreted as nearly compensated metals within the Co content of  $x \leq 0.08$ .

## 5.6. References

- [1] G. R. Stewart, Rev. Mod. Phys. **83**, 1589 (2011)
- [2] X. C. Wang *et al.*, Solid State Commun. **148**, 538 (2008)
- [3] J. H. Tapp *et al.*, Phys. Rev. B **78**, 060505 (2008)
- [4] M. J. Pitcher *et al.*, Chem. Commun. **2008**, 5918 (2008)
- [5] M. Rotter *et al.*, Phys. Rev. Lett. **101**, 107006 (2008)
- [6] N. Ni *et al.*, Phys. Rev. B **78**, 214515 (2008)
- [7] J.-H. Chu *et al.*, Phys. Rev. B **79**, 014506 (2009)
- [8] L. Fang *et al.*, Phys. Rev. B **80**, 140508 (2009)
- [9] P. L. Alireza *et al.*, J. Phys.: Condens. Matter **21**, 012208 (2009)
- [10] S. V. Borisenko *et al.*, Phys. Rev. Lett. **105**, 067002 (2010)
- [11] G. Lee *et al.*, Phys. Rev. Lett. **109**, 177001 (2012)
- [12] O. Heyer *et al.*, Phys. Rev. B **84**, 064512 (2011)
- [13] F. Rullier-Albenque *et al.*, Phys. Rev. Lett. **109**, 187005 (2012)
- [14] M. Gooch *et al.*, Europhys. Lett. **85**, 27005 (2009)
- [15] M. Mito *et al.*, J. Am. Chem. Soc. **131**, 2986 (2009)

- [16] S. J. Zhang *et al.*, Phys. Rev. B **80**, 014506 (2009)
- [17] M. J. Pitcher *et al.*, J. Am. Chem. Soc. **132**, 10467 (2010)
- [18] S. Aswartham *et al.*, Phys. Rev. B **84**, 054534 (2011)
- [19] L. Y. Xing *et al.*, J. Phys.: Condens. Matter **26**, 435703 (2014)
- [20] B. Lee *et al.*, Europhys. Lett. **91**, 67002 (2010)
- [21] A. E. Taylor *et al.*, Phys. Rev. B **83**, 220514 (2011)
- [22] N. E. Hussey, J. Phys. Soc. Jpn. **74**, 1107 (2005)
- [23] M. Neupane *et al.*, Phys. Rev. B **83**, 094522 (2011)

## 6. Impurity effects in $\text{Li}(\text{Fe}_{1-x}\text{Mn}_x)\text{As}$

### 6.1. Introduction

The superconducting pairing mechanism is the most important underlying nature to understand many exotic phenomena of the superconductivity. For conventional superconductors, it is known that the phonon mediates the electron-electron interaction. In the superconductivity of unconventional superconductors including the high  $T_c$  cuprates, however, spin fluctuations associated with the anti-ferromagnetic ground state in pristine compounds are expected to play an important role in the superconducting pairing mechanism [1]. Fe-based superconductors, the recently-found unconventional superconductors, are also suspected to be the system whose superconductivity is mediated by the spin fluctuations because of the common phase diagram. The superconductivity of the Fe-based family arises when the spin-density-wave ground state of the pristine compound is suppressed by the chemical substitution or the external pressure, which is analogous to one of the famous cuprates [2, 3]. Recent reports about the orbital or charge ordering in the Fe-based superconductors, on the other hand, claim that charge fluctuations may substitute the spin fluctuations as the superconducting pairing glue [1].

This argument about the pairing mechanism of the Fe-based superconductivity is still one of the interesting subject to investigate and the answer is expected to provide more evidences to reveal the exotic nature of the Fe-based superconductors. According to the theoretical investigations, the superconducting gap symmetry of the Fe-based superconductors, for example, would be strongly dependent to the pairing mechanism [4]. The gap symmetry is predicted to be the sign-changing  $s_{\pm}$ -

wave if the spin fluctuations mediate the interaction while it would be the sign-preserving  $s_{++}$ -wave if the charge fluctuations do [4].

The effects of non-magnetic and magnetic impurities have been investigated due to the striking experimental facts that enormous non-magnetic impurities have almost no influence on the superconducting transition temperature of conventional superconductors with a single and isotropic  $s$ -wave superconducting energy gap while magnetic impurities kill their superconductivity very effectively [5]. For the unconventional superconductors such as the high- $T_c$  cuprates which are known to have a  $d$ -wave energy gap, on the other hand, the non-magnetic impurities suppress the superconductivity similarly, or even more strongly than the magnetic impurities [6]. These exotic impurity effects are understood to be related to the superconducting energy gap symmetry since the scattering with the magnetic impurity induces a phase shift of the quasi-particle while one with the non-magnetic impurity does not [7]. The superconducting properties of the superconductors with magnetic or non-magnetic impurities controlled intentionally, therefore, have been studied to reveal the symmetry of the superconducting energy gap even it is a bit challenging experimentally.

The impurity effect on the superconducting transition temperature  $T_c$  of the Fe-based superconductors, furthermore, seems to be a good measure to reveal their superconducting gap symmetry as well as the pairing mechanism. It, however, have not been studied well although their superconducting gap symmetry has been investigated quite well by both of experimental and theoretical methods. It is based on the experimental difficulties. While the intentional introduction and control of the impurity in the specimens are still challenging, the facts that most of the pristine compounds are compensated metals with bad metallicity and the superconducting

specimens already contain the chemical impurities to suppress the magnetic transition of the pristine one and to induce the superconductivity [3] disturb the certain realization of the impurity effects.

In that sense, LiFeAs is a perfect candidate to study the impurity effects on its superconductivity. First of all, the superconductivity is the ground state of LiFeAs even at the ambient condition, and the transition temperature is relatively high as  $\sim 18$  K. In addition, the system is known to be very clean, evidenced by the residual resistivity ratio to the room temperature resistivity (RRR) which is reported to be  $\sim 40$ -250 in the crystal grown by the self-flux method [8-10], and the experimental study about its upper critical fields [11].  $\text{KFe}_2\text{As}_2$ , another good candidate for the study, has also a superconducting ground state and even larger RRR of  $\sim 1280$ , but the transition temperature is relatively lower as  $\sim 3$  K [12]. Large single crystals of LiFeAs, furthermore, with typical size of  $5 \times 5 \text{ mm}^2$  are easily grown while the size of  $\text{KFe}_2\text{As}_2$  single crystals is relatively smaller [13]. Although it has been evidenced by several experimental results that LiFeAs has an  $s_{\pm}$ -wave superconducting gap symmetry which is typically found in the Fe-based superconductors [14-18], still there is a couple of suggestions about a  $p$ -wave gap symmetry of LiFeAs based on the theoretical and experimental studies [19-22]. The debate about the gap symmetry of LiFeAs encourages more detailed investigation, and the high quality single crystals of LiFeAs with impurities controlled intentionally can provide crucial evidences to reveal the gap symmetry of the system.

In this chapter, physical properties and phase diagram of  $\text{Li}(\text{Fe}_{1-x}\text{Mn}_x)\text{As}$  single crystals while Mn ions are introduced into the system as impurities successfully are presented, and the results are compared with one of  $\text{Li}(\text{Fe}_{1-x}\text{Co}_x)\text{As}$  prepared in the same methods. The series of the single crystals are grown by the self-flux method

and it is confirmed by the x-ray diffraction that the crystals have single phase without any other structural phases, and the compositional study confirms that the Mn ions exist in the crystals. DC magnetic susceptibility and electrical resistivity are measured for both the superconducting and normal states. The superconducting transition is clearly suppressed by the Mn content while a Curie-Weiss-like temperature dependence is observed in the normal state magnetic susceptibility. By a simple fitting, it is realized that a number of the local magnetic moment induced by the Mn doping seems to increase as the nominal Mn doping level increases. The experimental results lead a conclusion that the Mn content in the LiFeAs single crystals seem to act as magnetic impurities and suppress the superconductivity more effectively than the Co content. Based on these experimental results and also the other experiments reports, the LiFeAs system seems to have the  $s\pm$ -wave gap symmetry as well as the pairing mechanism based on the spin fluctuations.

## **6.2. Structural and compositional properties**

To confirm the actual Mn content and the structural phase, the electron probe micro-analyzer and the powder X-ray diffraction measurements are performed for the single crystals of  $\text{Li}(\text{Fe}_{1-x}\text{Mn}_x)\text{As}$  with the nominal Mn doping level  $x = 0.00, 0.02, 0.04,$  and  $0.06$ . By the former measurements, the actual Mn content in the crystals with nominal  $x = 0.02, 0.04,$  and  $0.06$  is measured to be  $\sim 0.012, 0.025,$  and  $0.030$ , respectively, which is estimated from the ratio between the Fe and Mn contents.

Figure 6.1 shows the powder X-ray diffraction patterns for the single crystals of  $\text{Li}(\text{Fe}_{1-x}\text{Mn}_x)\text{As}$  while the quartz capillary is employed for the measurements. The Rietveld analysis is performed for each measured pattern, shown as black circle

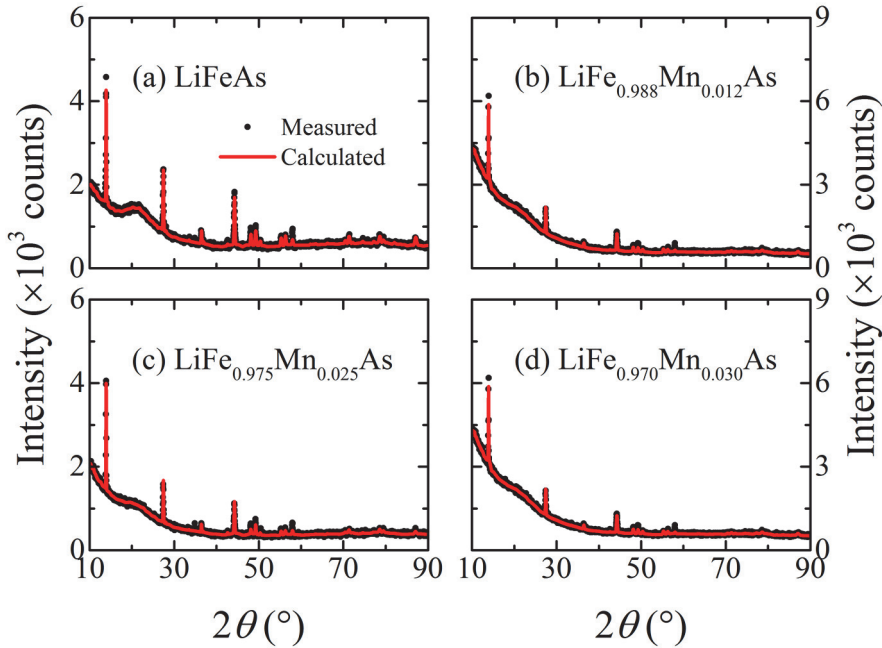


**Figure 6.1. Powder x-ray diffraction patterns of the  $\text{Li}(\text{Fe}_{1-x}\text{Mn}_x)\text{As}$  single crystals. The patterns of (a)  $x = 0.000$ , (b)  $x = 0.012$ , (c)  $x = 0.025$ , and (d)  $x = 0.030$  are presented. The black circles indicate the measured patterns and the red solid lines are the calculated pattern obtained from the Rietveld analysis.**

scatters in figure 6.1 while calculated pattern for each specimen is presented as a red solid line. The refinement is based on a single phase of the known structure of  $\text{LiFeAs}$  [23, 24], and all peaks in the patterns are included by the  $\text{LiFeAs}$ -based phase, implying the absence of any distinguishable impurity phase even in the crystal with highest doping level of  $x = 0.030$ .

From the analysis, lattice constants,  $a$  and  $c$ , are obtained for the crystals and presented with respect to the actual Mn content  $x$  in figure 6.2. Scatters of circles and squares indicate the obtained lattice constants  $a$  and  $c$ , respectively, while the dashed

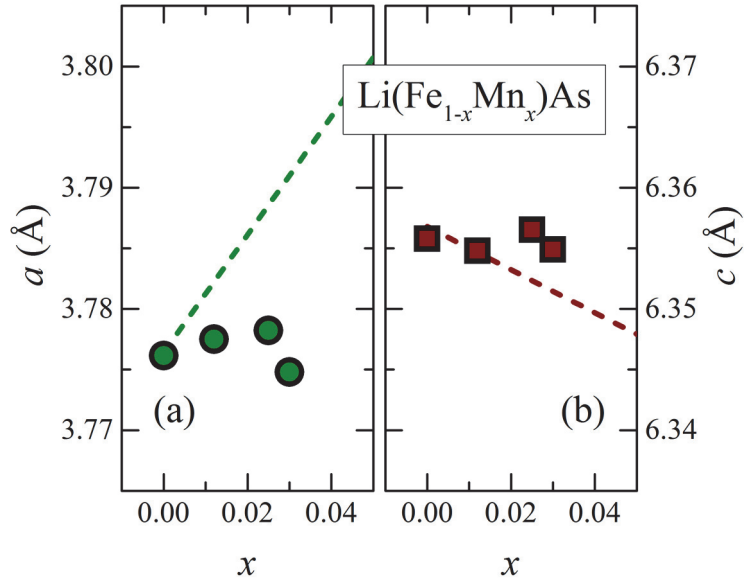


**Figure 6.2. The lattice constants (a)  $a$  and (b)  $c$  of the  $\text{Li}(\text{Fe}_{1-x}\text{Mn}_x)\text{As}$  series. The symbols represent the values realized from the Rietveld analysis and the dashed lines indicate the linear interpolations between the reported lattice constants of  $\text{LiFeAs}$  and  $\text{LiMnAs}$  [24, 25].**

lines represent linear interpolations between the reported lattice constants of  $\text{LiFeAs}$  and  $\text{LiMnAs}$  [24, 25] which imply the predicted values by the Vegard's law. Within the experimental results of the crystals in this work, however, both  $a$  and  $c$  of all crystals are realized to be within the range of  $0.005 \text{ \AA}$  and don't show any systematic doping dependences. This result means that the Vegard's law may not be applied on the  $\text{Li}(\text{Fe}_{1-x}\text{Mn}_x)\text{As}$  system.

### 6.3. Superconducting transition temperature

The DC magnetic volume susceptibility of the  $\text{Li}(\text{Fe}_{1-x}\text{Mn}_x)\text{As}$  single crystals is presented in figure 6.3 as well as one of the  $\text{Li}(\text{Fe}_{1-x}\text{Co}_x)\text{As}$  single crystals grown by

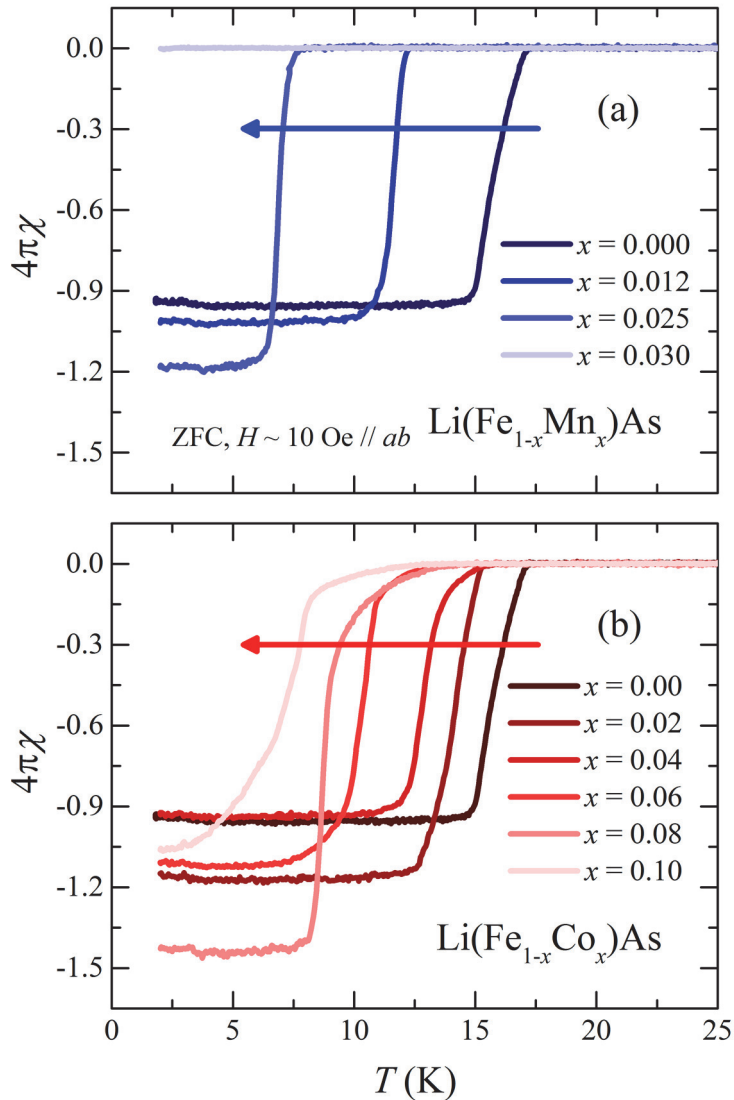


**Figure 6.3.** The magnetic volume susceptibility of the (a)  $\text{Li}(\text{Fe}_{1-x}\text{Mn}_x)\text{As}$  and (b)  $\text{Li}(\text{Fe}_{1-x}\text{Co}_x)\text{As}$  series measured under the zero-field-cooled condition with the magnetic fields of  $\sim 10$  Oe along the  $ab$ -plane.

the same manner to compare. The doping level of the  $\text{Li}(\text{Fe}_{1-x}\text{Mn}_x)\text{As}$  specimens presented in the figures and text below is the confirmed actual Mn content while

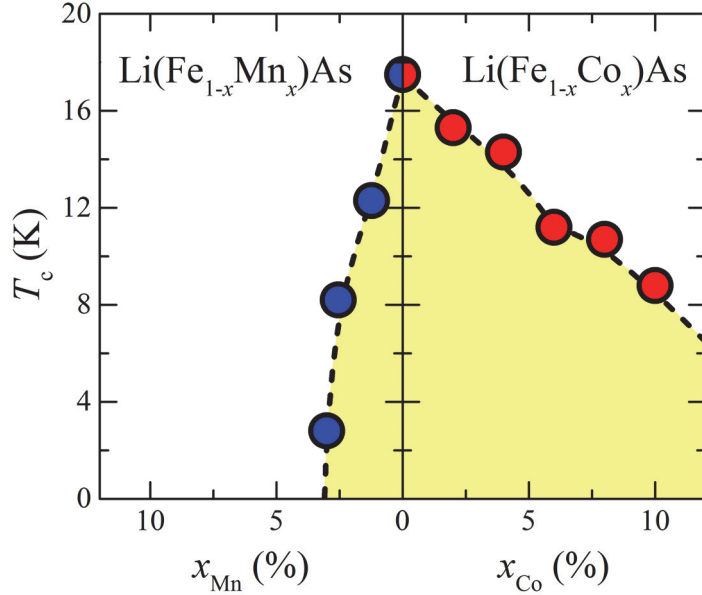


**Figure 6.4.** The doping dependence of  $T_c$  for the  $\text{Li}(\text{Fe}_{1-x}\text{Mn}_x)\text{As}$  and  $\text{Li}(\text{Fe}_{1-x}\text{Co}_x)\text{As}$  series. The transition temperature is realized from the magnetic susceptibility. The blue circles in the right side represent the  $\text{Li}(\text{Fe}_{1-x}\text{Mn}_x)\text{As}$  series while the red ones in the left side do the  $\text{Li}(\text{Fe}_{1-x}\text{Co}_x)\text{As}$  series. The dashed lines are drawn as simple guidelines by hand.

the nominal Co doping level is shown for the  $\text{Li}(\text{Fe}_{1-x}\text{Co}_x)\text{As}$  series. The presented susceptibility is measured with the magnetic fields of  $\sim 10$  Oe applied along the  $ab$ -plane at the zero-field-cooled condition. While the un-doped  $\text{LiFeAs}$  single crystal shows a clear superconducting transition with  $T_c$  of  $\sim 17.5$  K,  $T_c$  of both  $\text{Li}(\text{Fe}_{1-x}\text{Mn}_x)\text{As}$  and  $\text{Li}(\text{Fe}_{1-x}\text{Co}_x)\text{As}$  crystals monotonically decreases as the doping level  $x$  increases. The arrows in the figure guides the increase of  $x$ . In the Mn-doped series,  $T_c$  is suppressed as  $\sim 12.3$ ,  $8.2$ , and  $2.6$  K for the crystals with  $x = 0.012$ ,  $0.025$ , and  $0.030$ , respectively, which are realized by the comparison of the susceptibility measured at the zero-field-cooled and field-cooled conditions, and the

superconducting shielding fraction at 2 K almost disappears at  $x = 0.030$ . The suppression rate in  $\text{Li}(\text{Fe}_{1-x}\text{Mn}_x)\text{As}$  is relatively faster than one in  $\text{Li}(\text{Fe}_{1-x}\text{Co}_x)\text{As}$  while the superconducting transition of latter series is still clearly observed at  $x = 0.10$ , as presented in figure 6.3.

The doping dependence of the superconducting transition temperature  $T_c$  of the Mn- and Co-doped series is summarized in figure 6.4. The transition temperature is determined as the temperature where the diamagnetic signal starts to appear in the magnetic susceptibility measured under both the zero-field-cooled and field-cooled conditions. The blue circles in the left side indicate  $T_c$  of the Mn-doped series while the red circles in the right side indicate one of the Co-doped series. The dashed lines are just simple guidelines. As presented in figure 6.4 and also discussed above, the suppression of  $T_c$  is much faster in the Mn-doped specimens than the Co-doped specimens. One can easily estimate the suppression rate of  $T_c$  by a simple linear fit of the doping dependence and can obtain the suppression rates of the Mn- and Co-doped series of  $\sim 3.6$  and  $0.9$  K/%, respectively, from the slope of the linear fit. This huge difference in the suppression rate of  $T_c$  is expected to be caused by the impurity effects of the Mn and Co contents and will be discussed further at the end of this chapter.

#### **6.4. Curie-Weiss behavior and local magnetic moments**

As well as the magnetic susceptibility around the superconducting transition, one of the normal state is measured and shown in figure 6.5 for both of Mn- and Co-doped series. The magnetic susceptibility of  $\text{LiFeAs}$ , the un-doped specimen, exhibits a linear temperature dependence for the temperature window from 20 K, right above  $T_c$ , up to 300 K. While the susceptibility of the Co-doped crystals is

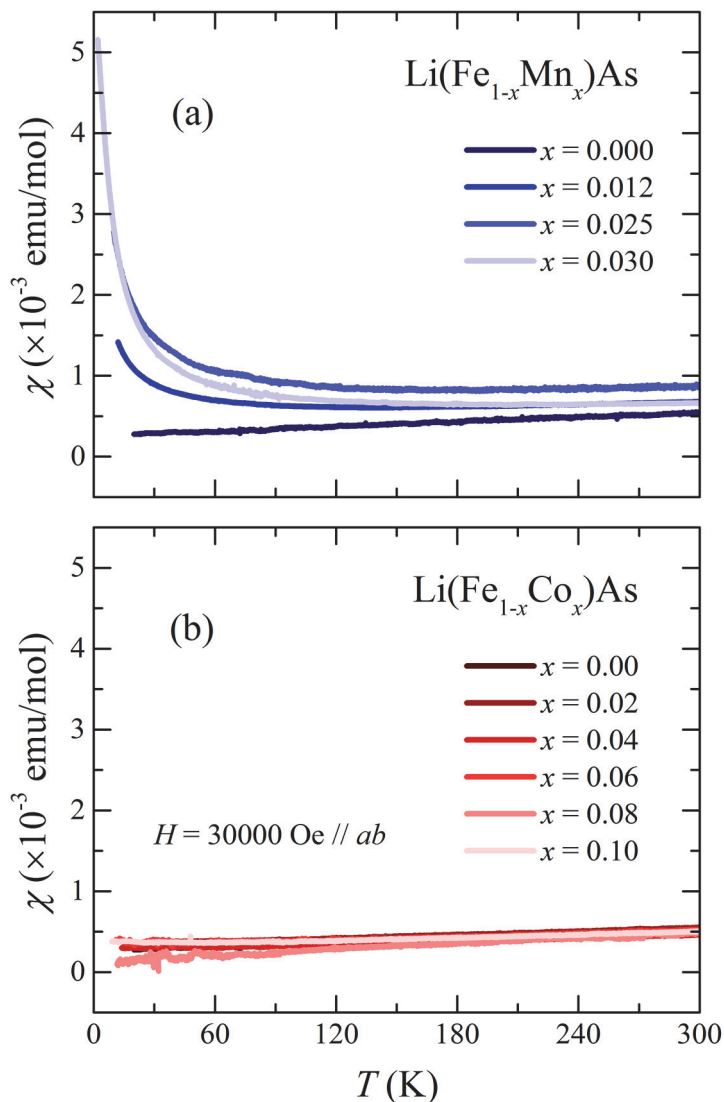


**Figure 6.5.** The temperature dependent DC magnetization curves of the (a)  $\text{Li}(\text{Fe}_{1-x}\text{Mn}_x)\text{As}$  and (b)  $\text{Li}(\text{Fe}_{1-x}\text{Co}_x)\text{As}$  series measured with the magnetic fields of  $\sim 30000$  Oe applied along the  $ab$ -plane.

almost unchanged from one of the un-doped specimen, as presented in figure 6.5 (b), the susceptibility of the Mn-doped crystals shows clear tendency of increasing as the

temperature is lowered and the temperature dependence seems to be similar to the Curie-Weiss behavior which implies the existence of the local paramagnetic moments. The Curie-Weiss-like increasing of the susceptibility, moreover, is even enhanced in the higher Mn doping level.

Since the linear temperature dependence of the susceptibility has been observed in the un-doped LiFeAs crystals, one can introduce a simple model for the temperature dependent magnetic susceptibility of  $\chi = \chi_P + A \cdot T + C_{CW}/(T + \Theta)$ , which includes the Pauli paramagnetic term  $\chi_P$ , the linear term  $A \cdot T$ , and the Curie-Weiss term  $C_{CW}/(T + \Theta)$  for the Mn-doped series. Figure 6.6 presents the coefficient  $C_{CW}$  from the fitting with respect to the Mn content  $x$ . As shown in the figure,  $C_{CW}$ , indicated as the symbols, increases as  $x$  increases and seems to be proportional to the Mn content.

The Curie-Weiss coefficient is known to be  $C_{CW} = \mu_0 n_{loc} \mu_{eff} / 3k_B T$  for a simple paramagnetic system, where  $\mu_0$  is the vacuum permeability,  $k_B$  is the Boltzmann constant,  $n_{loc}$  is the density of the local magnetic moments, and  $\mu_{eff}$  is the value of the effective magnetic moment [26]. The density of the local magnetic moments,  $n_{loc}$ , therefore, is expected to be proportional to  $C_{CW}$  and even to be estimated from the simple calculation if the effective moment,  $\mu_{eff}$ , is known. In this case of the Li(Fe<sub>1-x</sub>Mn<sub>x</sub>)As series, the doping dependence of  $C_{CW}$  which is proportional to the Mn doping level implies at least that the local paramagnetic moments are introduced with the Mn dopants, which may mean that the Mn dopants in the specimens are acting as magnetic impurities.

The Mn ions in LiMnAs, which is an isostructural compound with LiFeAs and also an antiferromagnetic semiconductor, are known to have the magnetic moment of  $3.76 \mu_B$  [27]. If one assumes that the Mn ions in the Li(Fe<sub>1-x</sub>Mn<sub>x</sub>)As crystals have

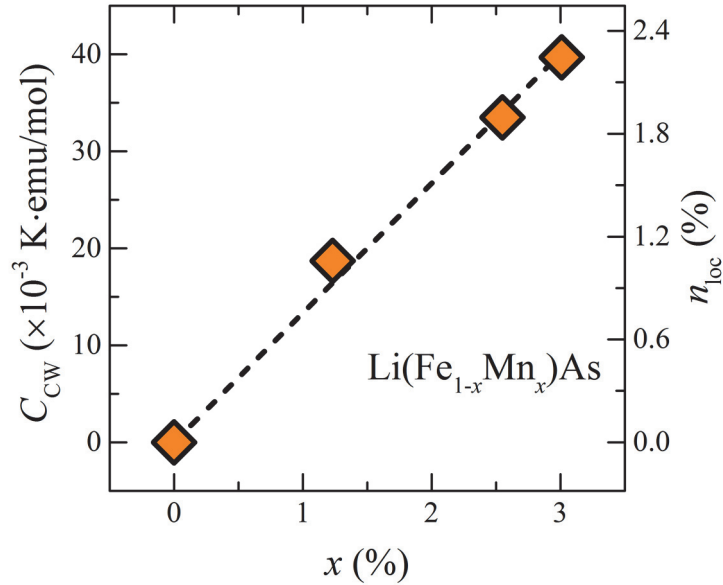


**Figure 6.6.** The Curie-Weiss coefficients of the  $\text{Li}(\text{Fe}_{1-x}\text{Mn}_x)\text{As}$  series realized from the fitting described in the text. The dashed line is a linear fit shown as a guideline.

same magnetic moments, the density of the local magnetic moments in the series can be realized. The right-side axis in figure 6.6 represents the calculated local moment density, and those density values are quite similar to the Mn content in the crystals. Even though the magnetic moment of each Mn ion in the  $\text{Li}(\text{Fe}_{1-x}\text{Mn}_x)\text{As}$  crystals is simply assumed to be same with the case of  $\text{LiMnAs}$ , the calculated local moment density may imply that the Mn content in the Mn-doped specimens introduces the localized magnetic moments into the system and the number of the introduced moments is proportional to the number of Mn dopants.

### 6.5. Electrical resistivity and impurity scattering

Electrical resistivity of each crystal is measured and shown in figure 6.7. The

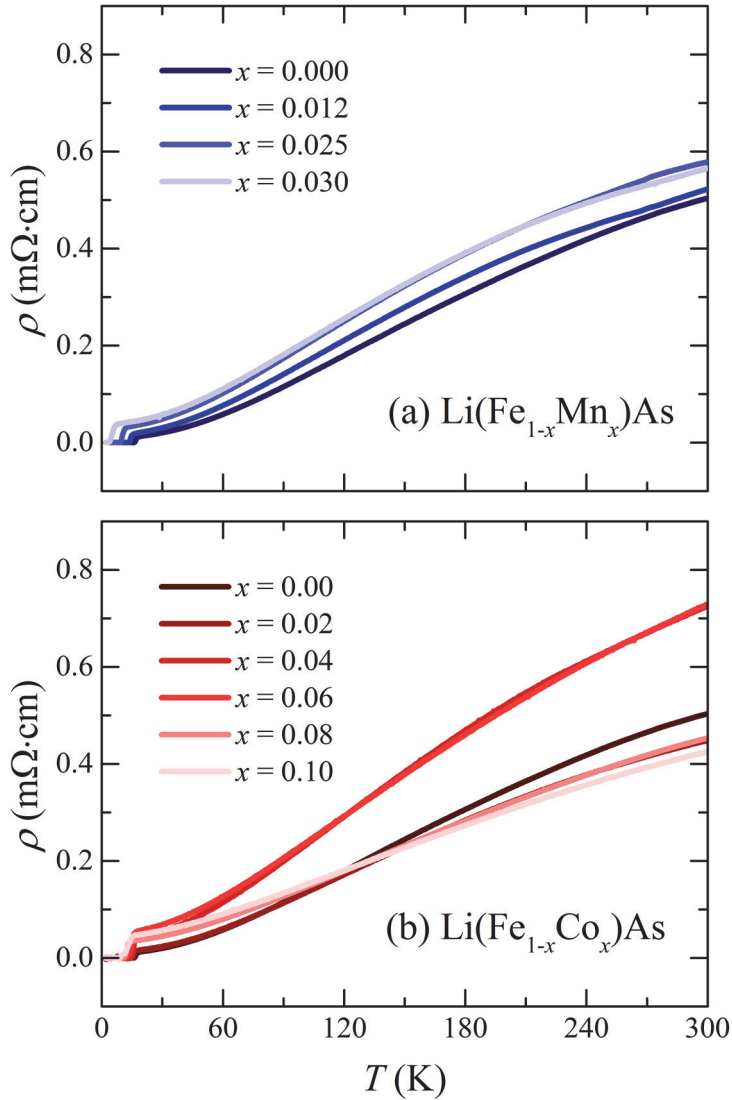


**Figure 6.7. The temperature dependent electrical resistivity curves of the (a)  $\text{Li}(\text{Fe}_{1-x}\text{Mn}_x)\text{As}$  and (b)  $\text{Li}(\text{Fe}_{1-x}\text{Co}_x)\text{As}$  series.**

measurements are performed down to 2 K and without any external magnetic fields. All specimens including both Mn- and Co-doped series exhibit the superconducting transition and achieve the zero resistivity within the experimental limit. The

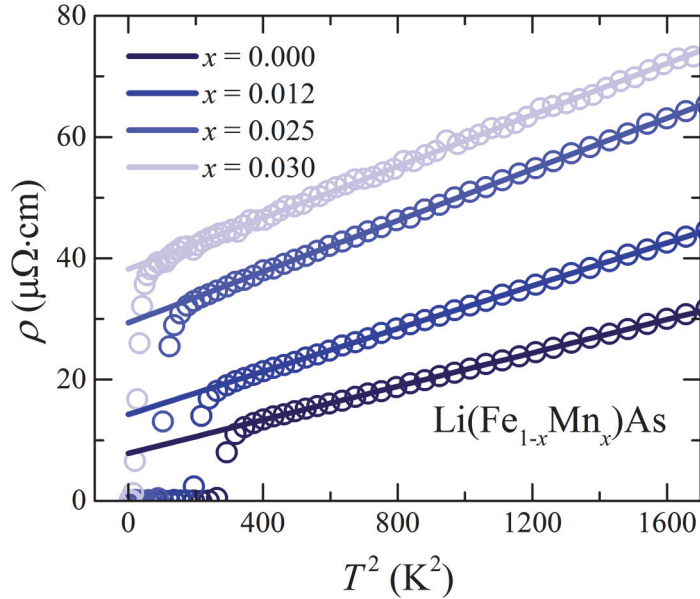


**Figure 6.8.** The  $T^2$  dependence of the resistivity of the  $\text{Li}(\text{Fe}_{1-x}\text{Mn}_x)\text{As}$  series. Open circles indicate the measured resistivity of the series and the solid lines represent the linear fits for the Fermi liquid behavior.

temperature where the zero resistivity is realized,  $T_{\text{zero}}$ , are  $\sim 15.7$ ,  $13.5$ ,  $9.1$ , and  $2.6$  K for the  $\text{Li}(\text{Fe}_{1-x}\text{Mn}_x)\text{As}$  crystals with  $x = 0.000$ ,  $0.012$ ,  $0.025$ , and  $0.030$ , respectively. These  $T_{\text{zero}}$  values realized in the resistivity curves are consistent with  $T_c$  obtained from the magnetic susceptibility, as commonly accepted consensus of that the demagnetization signal in the magnetic susceptibility due to the superconductivity starts to appear at the temperature where the resistivity becomes zero. As observed in the magnetic susceptibility, the superconducting transition is suppressed by both the Mn- and Co-doping while the suppression rate seems to be faster in the Mn-doped series. Any other anomaly except the superconducting transition is not found in the resistivity of the  $\text{Li}(\text{Fe}_{1-x}\text{Mn}_x)\text{As}$  crystals up to  $300$  K, which may indicate the absence of any long-range magnetic ordering.

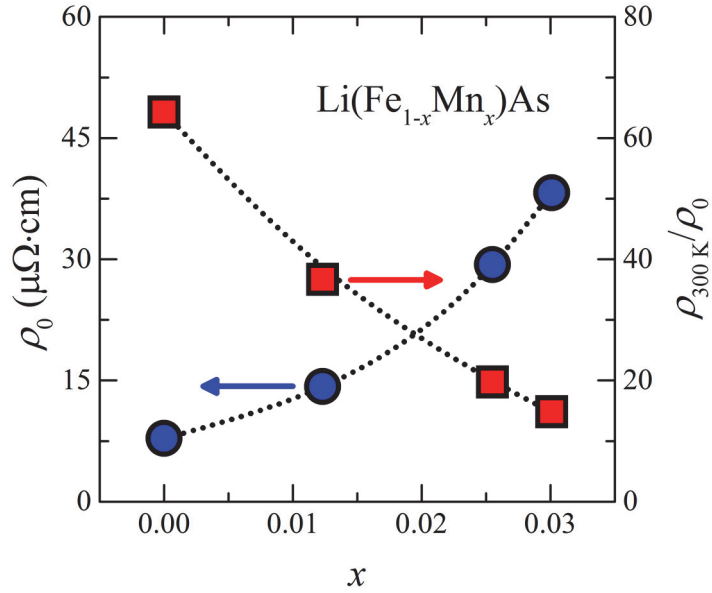


**Figure 6.9.** The doping dependence of the residual resistivity and RRR realized from the fitting for the resistivity of the  $\text{Li}(\text{Fe}_{1-x}\text{Mn}_x)\text{As}$  series. Blue circles with the left-side axis represent the residual resistivity realized from the fitting described in the text. Red squares with the right-side axis indicate the estimated RRR.

While the superconducting transition temperature is lowered by the Mn-doping, the residual resistivity  $\rho_0$  is increased by the dopants. With the same manner explained in the previous chapter for the Co-doped series, it is tried to fit the normal state resistivity of the  $\text{Li}(\text{Fe}_{1-x}\text{Mn}_x)\text{As}$  series at the low temperature slightly above  $T_c$  with the Fermi liquid model,  $\rho = \rho_0 + A \cdot T^2$ , to estimate the residual resistivity  $\rho_0$ . As presented in figure 6.8, the resistivity curves of the Mn-doped specimens show clear  $T^2$ -dependence at low temperature. The fitting is performed for the temperature window from 20 K to 40 K, and the fitting results are indicated as the solid lines in figure 6.8. The residual resistivity is realized as the intercept and

presented in figure 6.9 as well as RRR which is calculated as  $\rho_{300\text{ K}}/\rho_0$ .

The residual resistivity, which is represented as blue circles in figure 6.9, increases monotonically as the Mn content increases, resulting the monotonic decrease RRR, which is represented as red squares in the figure. The dotted lines are shown only as guidelines. RRR of the un-doped LiFeAs crystal, estimated to be  $\sim 64$ , is comparable to one of the cleanest single crystals of LiFeAs reported previously [8-10], and the RRR values become lower as  $\sim 37$ , 20, and 15 for  $x = 0.012$ , 0.025, and 0.030, respectively. Since the residual resistivity implies the scattering rate due to the impurity in the system, the increase of the residual resistivity and the associated increase of RRR evidences that the Mn content introduces the impurities into the system, which means that the Mn ions in the system play a role of the impurity.

## 6.6. Suppression rate of $T_c$ and impurity effects

Based on the results presented above, the Mn content in the  $\text{Li}(\text{Fe}_{1-x}\text{Mn}_x)\text{As}$  single crystals seems to play a role of the magnetic impurities while the Co content in the  $\text{Li}(\text{Fe}_{1-x}\text{Co}_x)\text{As}$  crystals is acting as the non-magnetic impurities. One should be extremely careful, however, to understand that the evolution of  $T_c$  by the Mn- and Co-doping is fully determined by the effect of the magnetic and non-magnetic impurity because the Co-doping shift the Fermi energy level as well as the Fermi surface topology, as discussed in previous chapter. The Mn-doping, on the other hand, seems not shifting the Fermi energy level, which means that the Mn-doping doesn't introduce any additional hole-carrier into the system, since that the band dispersion near the  $\Gamma$ -point of the Mn-doped crystal with  $x = 0.025$  remains unchanged from the un-doped one is observed in the experimental results of the angle-resolved

photoemission spectroscopy [28]. The change of the Fermi energy level and the Fermi surface also can influence many electronic properties such as the density of states at and near the Fermi level and the electron-electron interaction, which are strongly related to the superconductivity. Therefore, it is much more reasonable to understand that both of the non-magnetic impurity effect and the change of the electronic band structure affect the evolution of  $T_c$  in the  $\text{Li}(\text{Fe}_{1-x}\text{Co}_x)\text{As}$  series while only the magnetic impurity effect does in the  $\text{Li}(\text{Fe}_{1-x}\text{Mn}_x)\text{As}$  series.

Because of the difference between the doping effect by Mn- and Co-dopants, one needs to know the evolution of  $T_c$  by the other non-magnetic impurity to compare the magnetic and non-magnetic impurity effect on the superconductivity of  $\text{LiFeAs}$ . Recently, experimental results of  $\text{Li}(\text{Fe}_{1-x}\text{Cu}_x)\text{As}$  single crystals are reported and the Cu content in the system seems to be non-magnetic and also not to introduce any additional charge carrier into the system [29]. According to the authors,  $T_c$  is suppressed by the Cu content and the suppression rate of  $T_c$  is estimated to be  $\sim 1.9$  K/% from the linear fit [29], which is slower than the suppression rate of  $\sim 3.6$  K/% realized from the  $\text{Li}(\text{Fe}_{1-x}\text{Mn}_x)\text{As}$  crystals of this study. Figure 6.10, summarizing the doping dependence of the normalized transition temperature  $T_c/T_{c,0}$  while  $T_{c,0}$  is the transition temperature of the un-doped specimen, presents this contrast more clearly. Each symbol indicates the transition temperature realized in the magnetic susceptibility measurement and the dashed lines are drawn based on the linear fit which is employed to estimate the suppression rate. As expected in the comparison between the suppression rates, the Mn content kills the superconductivity more effectively than the Cu content, and this strong suppression of  $T_c$  by the Mn content can be the magnetic impurity effect.

A theoretical investigation about the impurity effect in the Fe-based

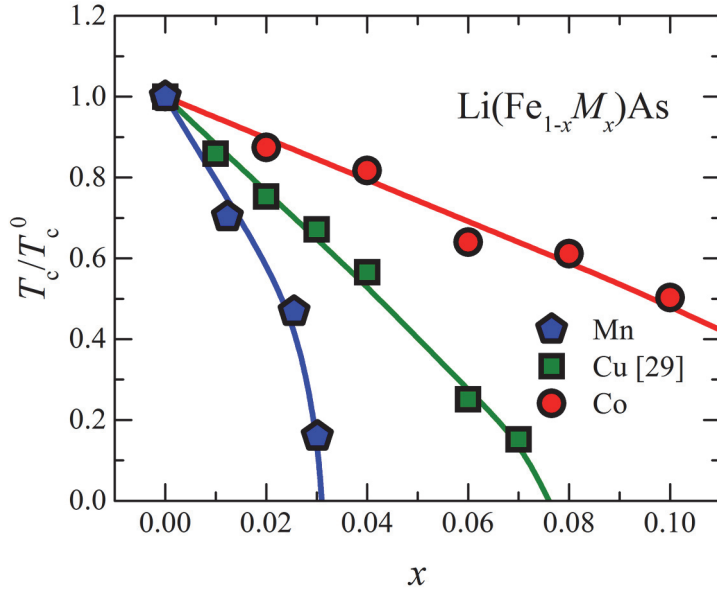


**Figure 6.10.** The normalized transition temperature of the  $\text{Li}(\text{Fe}_{1-x}\text{M}_x)\text{As}$  series with respect to the doping level. Blue pentagons, green squares, and red circles represent the transition temperature of the Mn-, Cu, and Co-doped series, respectively. The solid lines are drawn as guidelines based on the linear fit mentioned in the text.

superconductors has been reported and the suppression of  $T_c$  also has been discussed in the report [30]. It is well known that the Fe-based superconductors including LiFeAs have multiple Fermi surfaces where a superconducting gap is opened on each pocket. For the theoretical calculation, the electronic structure is approximated into a simple 2-band model and the  $s_{\pm}$ -wave gap symmetry has been employed to study the impurity effect. According to the report [30], the suppression rate of  $T_c$  caused by the magnetic impurity is slightly faster than one caused by the non-magnetic impurity. In addition, the contrast between the magnetic and non-magnetic impurity effect on the  $T_c$  suppression is expected to be clearer when the

ratio between the size of the large and small superconducting gaps is larger.

In the case of LiFeAs, it is well known that the effective 2-gap model is properly working to interpret many experimental results [14-18]. The specific heat of the LiFeAs crystals studied in this chapter is presented in figure 6.11 and the 2-gap feature is realized. The measured  $C_P/T$  of the normal states above 17 K is fitted with a formula of  $C_P/T = \gamma_N + \beta \cdot T^2 + \delta \cdot T^4$  and the coefficients are extracted as  $\gamma_N = 14.4 \text{ mJ/mol}\cdot\text{K}^2$ ,  $\beta = 0.214 \text{ mJ/mol}\cdot\text{K}^4$ , and  $\delta = 55.4 \text{ nJ/mol}\cdot\text{K}^6$ , resulting the Debye temperature of  $\Theta_D \sim 301 \text{ K}$  which is consistent with one estimated from the crystals grown by the Sn-flux method, discussed in the previous chapter. The fitted curve is shown as a red dashed line in figure 6.11 (a) with the measured data which is shown as blue circles. The electronic specific heat is presented in figure 6.11 (b) while the error bars are estimated as the standard deviation of the data measured at the same temperature. While the normal state electronic contribution is temperature-independent as  $\gamma_N$ , the clear jump-like feature associated with the superconducting transition is observed with the transition temperature of  $\sim 15.6 \text{ K}$ . The solid line in the figure indicate the calculation results based on the 2-gap model with the gaps of 1.3 and 3.0 meV sizes, and the calculation seems to agree with the experimental data within the error bars. These superconducting gaps result the ratio of  $\sim 2.3$ , which is consistent with previous reports, and one can expect that the suppression rates of  $T_c$  caused by the magnetic and non-magnetic impurities would be different to each other, based on this gap size and the theoretical prediction.

The suppression rate of  $T_c$  in the Li(Fe<sub>1-x</sub>Mn<sub>x</sub>)As series, therefore, is consistent with the theoretical prediction based on the  $s_{\pm}$ -wave gap symmetry. In the comparison with the  $T_c$  suppression in the Li(Fe<sub>1-x</sub>Cu<sub>x</sub>)As series, the Mn content

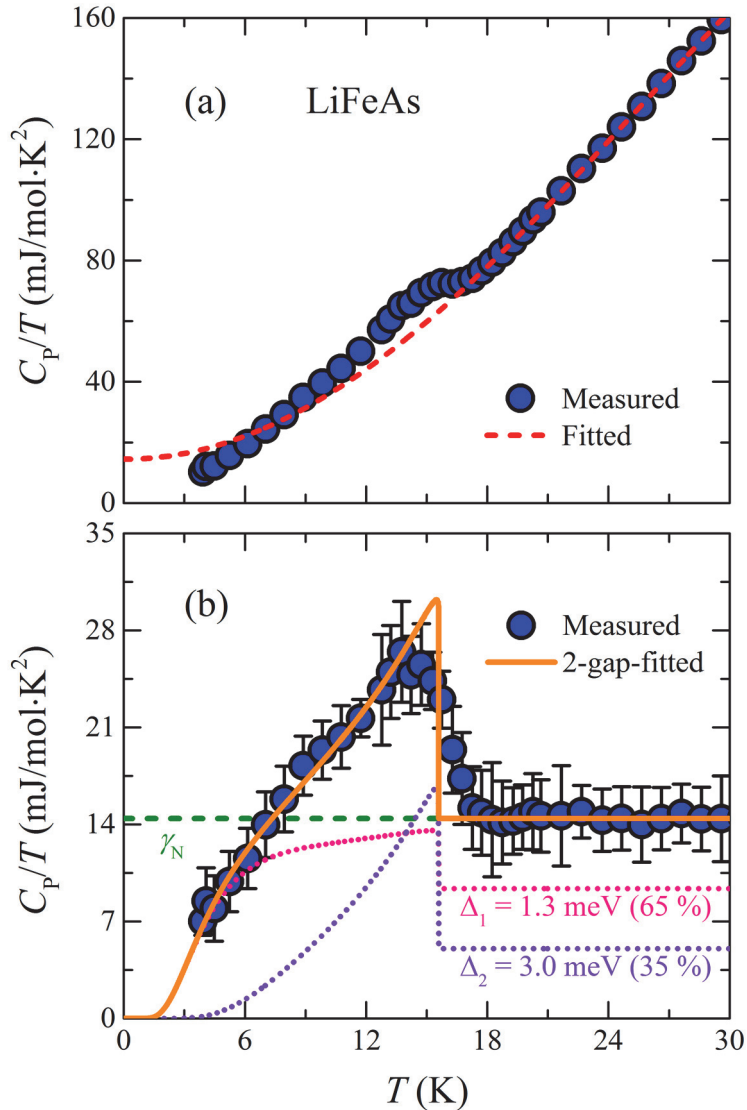


**Figure 6.11. (a) The total and (b) electronic specific heat of the LiFeAs single crystals. Blue circles represent the measured value with the error bar estimated as the standard deviation from the measurement. Dashed lines indicates the normal state specific heat realized from the fitting described in the text. Solid line in (b) represents the calculated curve from the 2-gap model while dotted lines indicate the contribution of each gap.**

acting as the magnetic impurity suppresses the superconducting transition faster than the Cu content acting as the non-magnetic impurity. These results agree with the prediction based on the sign-changing  $s_{\pm}$ -wave symmetry while the theoretical calculation based on the  $d$ -wave symmetry predicts the suppression by both the magnetic and non-magnetic impurity to be equal to each other [30]. In the case of the  $s_{++}$ -wave symmetry, which means the energy gap without any sign-changing character, it is expected that the magnetic impurity kill the superconductivity while the non-magnetic one doesn't suppress the transition as known in the conventional superconductors with the  $s$ -wave symmetry [5]. If LiFeAs has the  $p$ -wave symmetry, the  $T_c$  suppression should be rather quicker as observed in the case of  $\text{Sr}_2\text{RuO}_4$  [31].

These characteristic  $T_c$  suppressions due to the magnetic and non-magnetic impurity effects, moreover, evidence the pairing mechanism of the superconductivity in LiFeAs. Still there is an argument about the pairing mechanism of the Fe-based superconductors including LiFeAs even though the superconductivity arises in the vicinity where the spin-density-wave transition is fully suppressed in the phase space. Most favored scenario is that the spin fluctuation which originally mediate the spin-density-wave transition is acting as the superconducting pairing glue when the magnetic ground state is suppressed. Another possibility is that there is an orbital or charge ordering accompanying with the structural transition, whose transition temperature is slightly higher than the magnetic one, and the charge fluctuation mediate the superconductivity [4]. Theoretically, if the spin fluctuation mediates the superconductivity the superconducting gap symmetry is expected to be the sign-changing  $s_{\pm}$ -wave. If the charge fluctuation does, the sign-preserving  $s_{++}$ -wave is expected [4]. The observation of this study, therefore, which is supporting the  $s_{\pm}$ -wave symmetry, may also support the spin-fluctuation-mediated superconductivity

of LiFeAs even though any sign of the spin-density-wave transition is not found. It is expected that the observation will be a clue to reveal the general superconducting pairing mechanism of the entire Fe-based superconductor family.

## 6.7. Summary

In this chapter, several physical properties of the  $\text{Li}(\text{Fe}_{1-x}\text{Mn}_x)\text{As}$  single crystals with the doping level up to  $x = 0.030$  grown by the self-flux method are discussed. The superconducting transition temperature of the series is realized in the magnetic susceptibility and it is suppressed quickly by the Mn content. The magnetization of the series shows the Curie-Weiss-like temperature dependence, implying the introduction of the local magnetic moments. The Curie-Weiss coefficient, which is proportional to the local moment density in the system, increases as the Mn content increases. With the increase of the resistivity, one can conclude that the Mn dopants play a role of the magnetic impurity. The strong  $T_c$  suppression caused by the Mn content supports the  $s\pm$ -wave gap symmetry of LiFeAs. This result, furthermore, may evidence the spin-fluctuation-mediated superconductivity of LiFeAs.

## 6.8. References

- [1] D. J. Scalapino, Rev. Mod. Phys. **84**, 1383 (2012)
- [2] P. A. Lee *et al.*, Rev. Mod. Phys. **78**, 17 (2006)
- [3] G. R. Stewart, Rev. Mod. Phys. **83**, 1589 (2011)
- [4] A. Chubukov, Annu. Rev. Condens. Matter Phys. **3**, 57 (2012)
- [5] P. W. Anderson, J. Phys. Chem. Solids **11**, 26 (1959)
- [6] K. Ishida *et al.*, J. Phys. Soc. Jpn. **62**, 2803 (1993)
- [7] M. Tinkham, "Introduction to Superconductivity" 2nd ed. (Dover, 2004)

- [8] O. Heyer *et al.*, Phys. Rev. B **84**, 064512 (2011)
- [9] S. Kasahara *et al.*, Phys. Rev. B **85**, 060503 (2012)
- [10] F. Rullier-Albenque *et al.*, Phys. Rev. Lett. **109**, 187005 (2012)
- [11] S. Khim *et al.*, Phys. Rev. B **84**, 104502 (2011)
- [12] K. Hashimoto *et al.*, Phys. Rev. B **82**, 014526 (2010)
- [13] J. K. Dong *et al.*, Phys. Rev. Lett. **104**, 087005 (2010)
- [14] U. Stockert *et al.*, Phys. Rev. B **83**, 224512 (2011)
- [15] D.-J. Jang *et al.*, Phys. Rev. B **85**, 180505 (2012)
- [16] K. Hashimoto *et al.*, Phys. Rev. Lett. **108**, 047003 (2012)
- [17] Y. J. Song *et al.*, Europhys. Lett. **94**, 57008 (2011)
- [18] K. Umezawa *et al.*, Phys. Rev. Lett. **108**, 037002 (2012)
- [19] P. M. R. Brydon *et al.*, Phys. Rev. B **83**, 060501 (2011)
- [20] T. Hänke *et al.*, Phys. Rev. Lett. **108**, 127001 (2012)
- [21] G. Li *et al.*, Phys. Rev. B **87**, 024512 (2013)
- [22] S.-H. Baek *et al.*, J. Phys.: Condens. Matter **25**, 162204 (2013)
- [23] J. H. Tapp *et al.*, Phys. Rev. B **78**, 060505 (2008)
- [24] M. J. Pitcher *et al.*, Chem. Commun. **2008**, 5918 (2008)
- [25] W. Bronger *et al.*, Z. Anorg. Allg. Chem. **539**, 175 (1986)
- [26] S. Blundell, “Magnetism in Condensed Matter” (Oxford, 2001)
- [27] A. Beleanu *et al.*, Phys. Rev. B **88**, 184429 (2013)
- [28] J. Seo *et al.*, (to be submitted)
- [29] L. Y. Xing *et al.*, J. Phys.: Condens. Matter **26**, 435703 (2014)
- [30] Y. Bang *et al.*, Phys. Rev. B **79**, 054529 (2009)
- [31] N. Kikugawa *et al.*, J. Phys. Soc. Jpn. **72**, 237 (2003)

## 7. Phase competition in $(\text{Na}_{1-x}\text{Li}_x)\text{FeAs}$

### 7.1. Introduction

Among the Fe-based superconductors,  $A\text{FeAs}$  ( $A = \text{Li}$  and  $\text{Na}$ ), as known as the 111 system, is one of very unique system because of the ground state of the pristine compounds without any chemical substitution or applied external pressure [1-4]. While  $\text{LiFeAs}$  single crystals show a superconducting transition with a transition temperature of  $\sim 18$  K without any other transition or anomaly up to 300 K [1-3],  $\text{NaFeAs}$  single crystals exhibit all 3 of structural, magnetic, and superconducting transitions with transition temperatures of 52, 41, and 23 K, respectively, determined as the onset temperature in the temperature dependence of the resistivity [4]. The multiple phase transitions including both of the spin-density-wave (SDW) and superconducting transitions in  $\text{NaFeAs}$  is very unique since most of the pristine compounds of other Fe-based superconductor family only have structural and SDW transitions and the superconductivity is induced by chemical doping or external pressure while the SDW ground state is suppressed [5].

Intensive investigations, therefore, to reveal the relationship between the SDW and superconducting states in  $\text{NaFeAs}$  have been performed and reported. The superconducting volume fraction, for example, estimated from a DC magnetic susceptibility measurement at the zero-field-cooled condition is only  $\sim 10\%$  [4, 6-8] while a muon-spin resonance study on the polycrystalline specimen reveals the existence of a long-range antiferromagnetic order in most of the sample volume [8, 9]. From an angle-resolved photoemission spectroscopy (ARPES) experiment on the single crystal of  $\text{NaFeAs}$ , in addition, a superconducting gap is not observed [10],

which supports that the superconductivity of NaFeAs is not a bulk one and only very small fraction of  $\sim 10\%$  becomes superconducting while the rest is still in the SDW ground state.

The weakened superconductivity with the dominant SDW state is somewhat similar to the ground state of the under-doped regime in other Fe-based superconductors [5], and there have been several attempts to substitute the Fe-site in NaFeAs with other transition metal ions such as Co and Cu and to achieve the bulk superconductivity [6, 7]. As expected, the chemical doping of Co and Cu successfully suppresses the SDW transition as well as the structural one and enhances the superconducting transition temperature up to  $\sim 20$  and  $11.5$  K at the optimal doping level of  $2.8$  and  $1.9\%$ , respectively [6, 7], while subsequent scanning tunneling spectroscopy study suggests the microscopic coexistence of SDW and superconductivity in the under-doped crystal of  $\text{Na}(\text{Fe}_{1-x}\text{Co}_x)\text{As}$  [11]. These doping studies have provided important information about the superconductivity in the systems related to NaFeAs, such as relatively narrow superconducting dome in the phase diagram, however those are also limited in the chemical substitution on the Fe-site and direct introduction of additional electron carriers into the system. To expand the playground of the investigation about the superconductivity in NaFeAs, more studies about various substitution such as isovalent one are needed.

Several isovalent doping in the tetrahedral layer such as the Se, P, and Ru substitution on the Te-, As- and Fe-site have been reported to suppress the spin-density-wave state and induce the superconductivity [12-14], but the system with the substitution in the charge reservoir layer such as  $(\text{Ba}_{1-x}\text{Sr}_x)\text{Fe}_2\text{As}_2$  series didn't exhibit the superconducting transition in the whole series because both of the end-members,  $\text{BaFe}_2\text{As}_2$  and  $\text{SrFe}_2\text{As}_2$ , prefer to have the spin-density-wave ground state

instead of the superconducting one [15]. In this respect, the Li substitution on the Na-site of NaFeAs would be a good option to explore the phase space. The Li substitution is expected to be an isovalent doping in the charge reservoir layer instead of the Fe-As tetrahedral layer and LiFeAs is known to be a bulk superconductor while both of the spin-density-wave and superconducting transitions are observed in NaFeAs at the same time. The phase space between NaFeAs and LiFeAs, therefore, has been attractive from their discoveries, however the lack of high quality single crystals due to the experimental difficulties caused by the presence of Na and Li, has disrupted the research activities.

In this chapter, a successful growth of the high quality  $(\text{Na}_{1-x}\text{Li}_x)\text{FeAs}$  single crystals for the wide doping range up to  $x = 0.12$  is presented. The self-flux method accompanied with the Nb bomb technique is employed for the growth and actual Li content in the crystals is confirmed to be same with the nominal one for the crystals of  $x = 0.05$  which is optimal. From DC magnetic susceptibility and resistivity measurements, the doping dependence of the superconducting transition temperature is estimated and summarized into the phase diagram. To investigate the superconducting properties, lower critical fields and specific heat of the optimally-doped crystals are measured and the results suggest that a weakly-coupled gap is dominant in the superconductivity of the crystal without clear observation for the contribution of a strongly-coupled gap within a 2-gap model.

## **7.2. Structure, composition, and crystallinity**

Since the technical difficulty in the growth of high quality single crystals has disturbed the experimental studies on the  $(\text{Na}_{1-x}\text{Li}_x)\text{FeAs}$  series, the quality of the single crystals grown by the self-flux method, which are studied in this work, has to

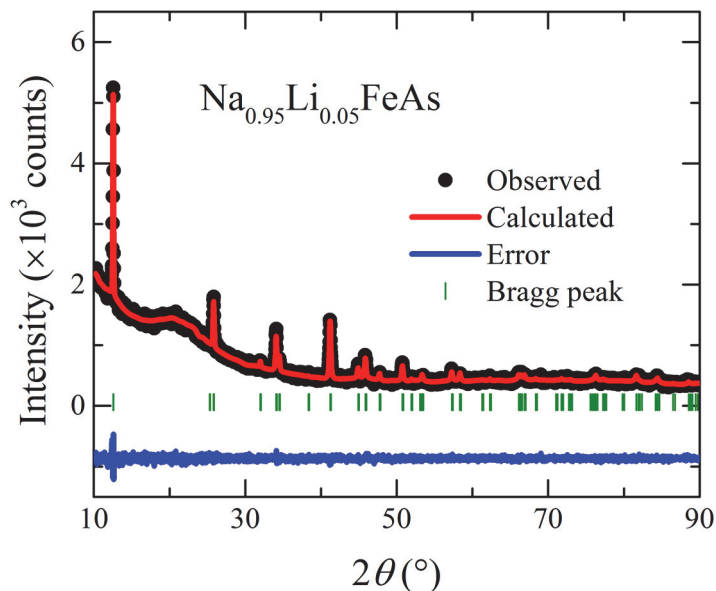


**Figure 7.1. Powder x-ray diffraction pattern of the  $(\text{Na}_{0.95}\text{Li}_{0.05})\text{FeAs}$  single crystals. Black circles and red solid line represent the measured and calculated patterns, respectively. Green ticks and blue solid line at the bottom indicate the Bragg peak position and the difference between the measured and calculated patterns. The calculated pattern and the difference are obtained from the Rietveld analysis.**

be confirmed. To check the quality, the inductively coupled plasma atomic emission spectroscopy (ICP-AES) and the powder x-ray diffraction experiment (XRD) are performed on the crystals with the nominal Li content of  $x = 0.05$ . While the molar ratio between Na and Li in the crystals is measured to be  $\text{Na} : \text{Li} = 0.944 : 0.056$  by the ICP-AES experiment, the powder XRD pattern of the crystals from the same batch is refined to be a single phase based on the  $\text{NaFeAs}$  structure without any impurity phases [16].

The result of the refinement is presented in figure 7.1. Black circles in the figure

indicate the measured pattern and a red solid line does the calculated pattern. Green ticks and a blue solid line at the bottom of the figure represent the Bragg peak position of the structural phase and the difference between the measured and calculated pattern, respectively. As mentioned above, the overall measured pattern well agrees with the calculated pattern and any peaks which can't be identified with the expected peak position are not found. These ICP-AES and XRD results imply that the actual Li content is almost same with the nominal one and it doesn't form any other structural phases but only the NaFeAs-based one.

In addition to these results, the nuclear magnetic resonance (NMR) experiments evidences the homogeneity of the crystals. The  $^{23}\text{Na}$  and  $^{75}\text{As}$  NMR spectra of the crystals with  $x = 0.05$ , ones from the same batch with the specimens used in the ICP-AES and XRD measurements, are measured to be a bit broader than ones of the parent NaFeAs [17], probably due to the disorder effect induced by the chemical substitution. The spectra, however, still are reasonably narrow and well-confined enough to conclude that the sample is single phase with reasonable disorder level [18], which is consistent and supporting the results discussed above.

Based on the above results, ICP-AES, XRD, and NMR, one can conclude that the grown crystals with the nominal Li content  $x = 0.05$  is actually the single crystals with the Li content  $x = 0.05$  and the Li content in the crystals distributes homogeneously. The Li content, furthermore, seems to introduce small disorder into the system, which is generally expected and realized for the chemical substitution. It is the first successful realization of the single crystals of the  $(\text{Na}_{1-x}\text{Li}_x)\text{FeAs}$  series, and the crystals with other doping level are grown by the same method and confirmed to be single phase as well by the powder XRD measurements.

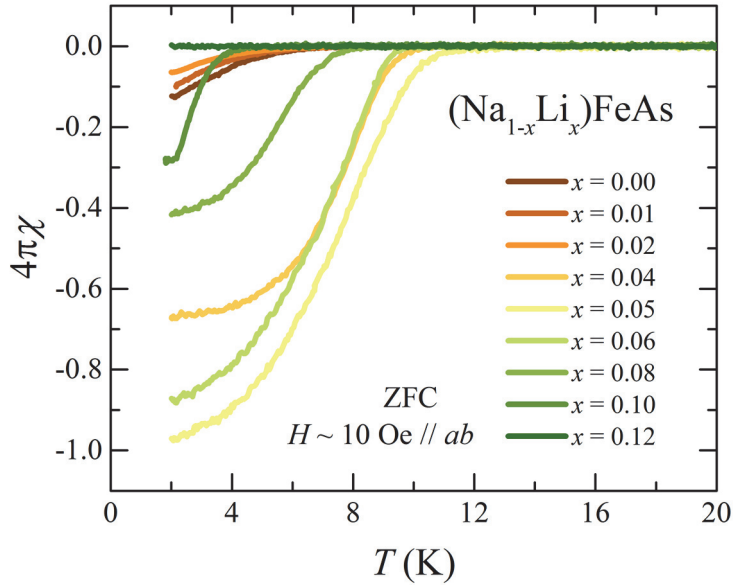


**Figure 7.2.** The DC volume magnetic susceptibility of the  $(\text{Na}_{1-x}\text{Li}_x)\text{FeAs}$  series measured under the zero-field-cooled condition with the magnetic fields of  $\sim 10$  Oe applied along the  $ab$ -plane.

### 7.3. Development of the superconductivity

Figure 7.2 shows the DC volume magnetic susceptibility of the  $(\text{Na}_{1-x}\text{Li}_x)\text{FeAs}$  series with the Li content of  $x \leq 0.12$ . The susceptibility is measured down to 2 K with the external magnetic fields of  $\sim 10$  Oe applied along the  $ab$ -plane under the zero-field-cooled condition. The demagnetization indicating the superconducting shielding fraction is observed even in the un-doped  $\text{NaFeAs}$  and it seems to be a bit suppressed by the low Li doping region,  $x = 0.01$  and  $0.02$ . Further doping, however, clearly enhance the superconducting shield fraction as well as the superconducting transition temperature  $T_c$  and the specimen with  $x = 0.05$  exhibits the highest  $T_c$  and the shielding fraction. In the high Li doping region where  $x > 0.05$ , the transition

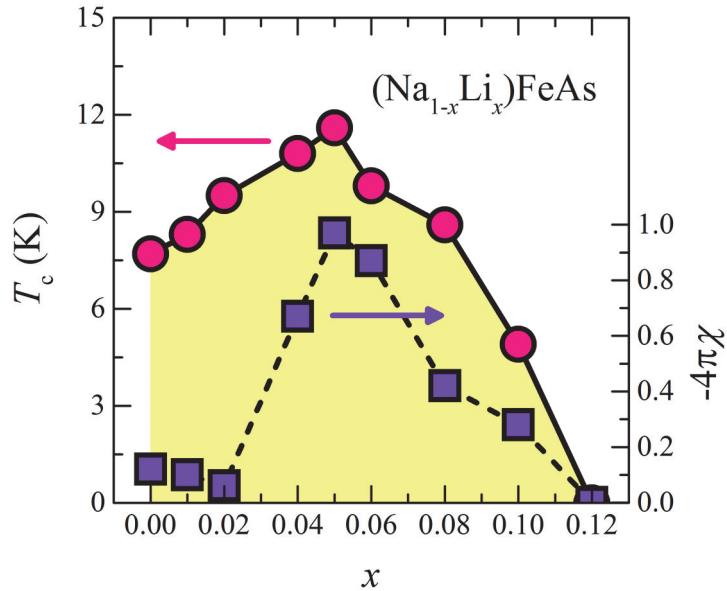


**Figure 7.3.** The doping dependence of the transition temperature and the superconducting shielding fraction of the  $(\text{Na}_{1-x}\text{Li}_x)\text{FeAs}$  series. Circles represent the transition temperature realized from the magnetic susceptibility with the left-side axis. Squares indicate the shielding fraction with the right-side axis, estimated as the susceptibility value at 2 K in the zero-field-cooled curve.

is again suppressed gradually and disappeared at  $x = 0.12$  within the experimental limit of 2 K.

The transition temperature, determined as the temperature where the zero-field-cooled susceptibility deviates from the field-cooled susceptibility, and the superconducting shielding fraction, realized as the volume susceptibility value measured at 2 K with the zero-field-cooled condition, of the whole series are summarized in figure 7.3. The circles and squares represent the transition temperature and the superconducting shielding fraction with left and right axes,

respectively. The solid and dashed lines are drawn as simple guidelines. As shown in figure 7.3, the transition temperature increases gradually up to  $x = 0.05$  and then suppressed rather quickly at further Li doping. The shielding fraction, however, is not increased at very low doping region while its decreasing trend at the high doping region seems to be accompanied by the suppression of  $T_c$ . Although the doping dependence of the transition temperature and the shielding fraction is not perfectly agreeing to each other, it is a quite firm conclusion that the superconductivity of the  $(\text{Na}_{1-x}\text{Li}_x)\text{FeAs}$  series is enhanced and suppressed by the Li substitution and the specimen with  $x = 0.05$  is the optimal one among these series up to  $x \leq 0.12$ .

#### 7.4. Suppression of the spin-density-wave transition

Electrical resistivity of the  $(\text{Na}_{1-x}\text{Li}_x)\text{FeAs}$  series is measured and presented in figure 7.4. For convenience, the resistivity of the under-doped specimens, whose Li content is  $0.00 \leq x \leq 0.05$ , and one of the over-doped specimens,  $0.05 \leq x \leq 0.12$ , are presented separately in figure 7.4 (a) and (b). The resistivity is measured with the applied electrical current in the  $ab$ -plane. As shown in the figure, features of the structural and magnetic transitions are clearly found in the resistivity of the un-doped  $\text{NaFeAs}$  crystals, which is consistent with previous reports [4]. The resistivity of  $\text{NaFeAs}$  monotonically decreases as the temperature decreases from the room temperature, and it suddenly increases and again decreases at  $\sim 53$  and  $44$  K, which seems to be accompanied by the structural and magnetic transitions, respectively. These upward and downward features are found to be suppressed in the resistivity of the low-doping specimens. The crystals of  $x = 0.01$  and  $0.02$  exhibit the sudden increase of the resistivity at the temperature lower than  $\sim 53$  K of the un-doped crystal and the increment becomes larger than one of the un-doped crystal. The

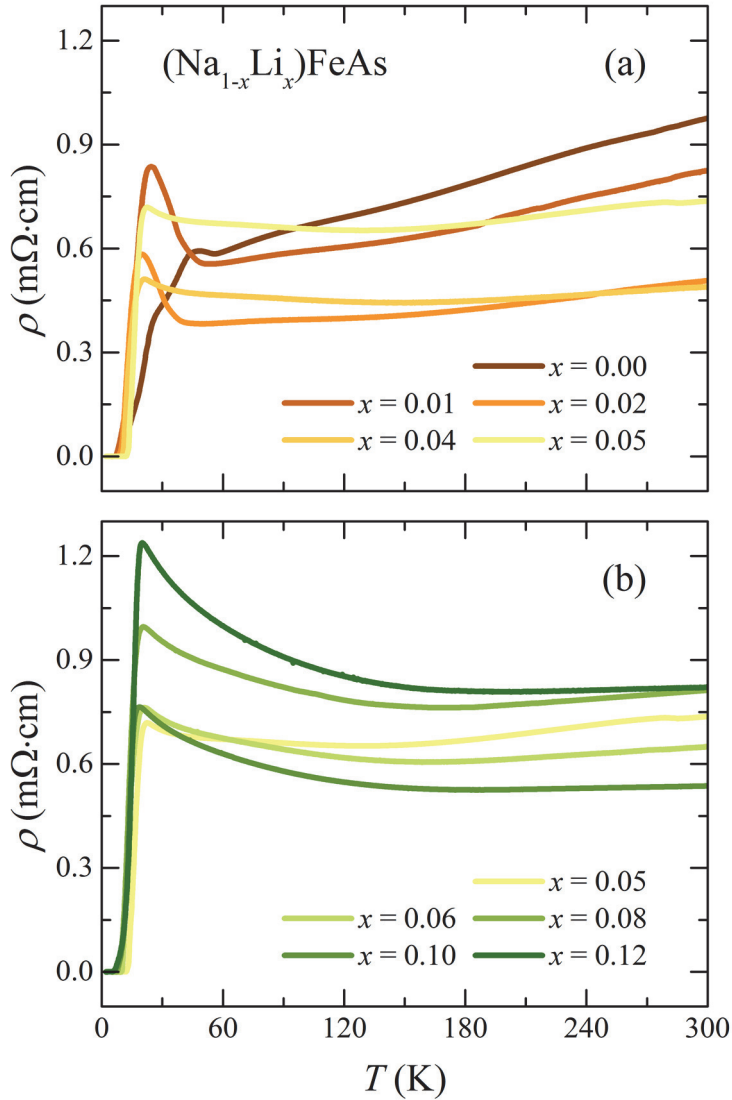


**Figure 7.4.** The electrical resistivity of the  $(\text{Na}_{1-x}\text{Li}_x)\text{FeAs}$  series for (a) the low doping region with  $0.00 \leq x \leq 0.05$  and (b) the high doping region with  $0.05 \leq x \leq 0.12$ .

increasing behavior of the resistivity, on the other hand, is not a sudden one any more but much smooth one in the crystals of  $x = 0.04$  and  $0.05$ . Even in the high doping

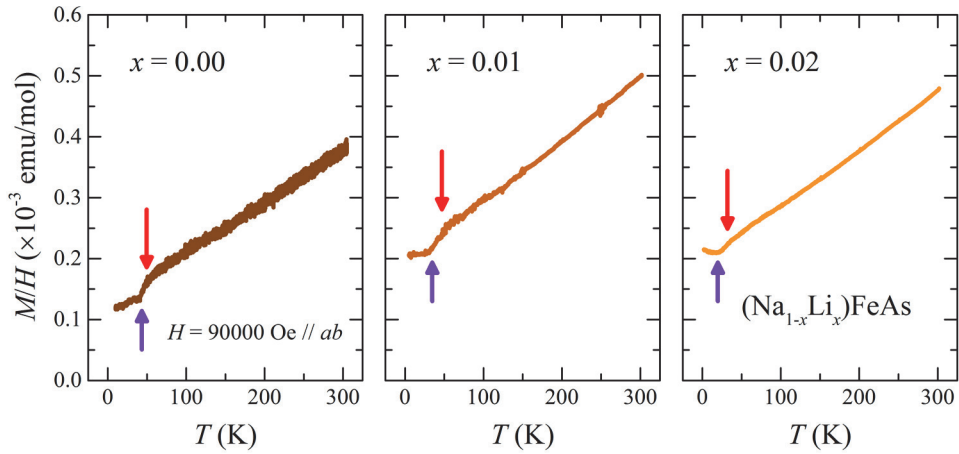


**Figure 7.5. The temperature dependent magnetization curves of (a) NaFeAs, (b)  $(\text{Na}_{0.99}\text{Li}_{0.01})\text{FeAs}$ , and (c)  $(\text{Na}_{0.98}\text{Li}_{0.02})\text{FeAs}$ . The magnetization is measured under the magnetic fields of  $\sim 90000$  Oe applied along the  $ab$ -plane. The red downward arrows and the violet upward ones in the figure indicate the structural and magnetic transition temperatures as described in the text.**

region, the samples become more insulating with higher Li content, as presented in figure 7.4 (b).

Since the anomalies in the resistivity of the low doping crystals seems to be the traces of the structural and magnetic transitions, one may conclude that the structural and magnetic transitions are suppressed by the Li content while the superconducting one is arisen. If the resistivity anomalies indicate the transitions, the change in the magnetization curve is expected to be observed at near temperature. The magnetization curves of the crystals with  $x = 0.00$ ,  $0.01$ , and  $0.02$  are shown in figure 7.5 (a), (b), and (c) respectively, which are measured under the magnetic fields of  $\sim 90000$  Oe applied along the  $ab$ -plane for the same pieces used for the volume susceptibility measurements in figure 7.2. While its magnetization is linear to the

temperature at the high temperature region as shown in figure 7.5 (a), the un-doped NaFeAs crystal shows slight curvature changes. The magnetization anomalies are determined as the temperatures where the magnetization curve deviates from the high temperature linear behavior, noted as the downward and red arrow in the figure, and where the curvature of the measured curve changes again at lower temperature, noted as the upward and violet arrow in the figure. The anomalies are realized at  $\sim 53$  and  $44$  K and these temperatures are consistent with the structural and magnetic transition temperatures reported previously [4]. In the crystals with the Li content of  $x = 0.01$  and  $0.02$ , similar curvature changes are observed. These anomalies in the Li-doped specimens, therefore, are suspected to be the traces of the structural and magnetic transitions.

To investigate further, the magnetization of the low temperature region and the first derivative of the resistivity are summarized in figure 7.6. In addition, the Hall effects of the specimens with Li content  $x = 0.00, 0.01,$  and  $0.02$  are measured with the external magnetic fields along the  $c$ -axis. The field-independent term of the Hall coefficients are presented in figure 7.6. The magnetization curves are shown in the first row of figure 7.6 (a), (b), and (c) for  $x = 0.00, 0.01,$  and  $0.02,$  respectively. The derivative of the resistivity and the Hall coefficients are shown in the second and third row of figure 7.6 with same order of the specimens. In the results of the un-doped specimen, presented in (a), (d), and (g), 2 dips are observed in the resistivity derivative at the temperature where the magnetization anomalies are found. 2 vertical lines, one dashed red line and another dot-and-dashed violet line, indicate the structural and magnetic transition temperatures, respectively. The dips in the resistivity derivative are also found in the figure (e) and (f) for  $x = 0.01$  and  $0.02$ . From the magnetization anomalies and the dips in the resistivity derivative, the

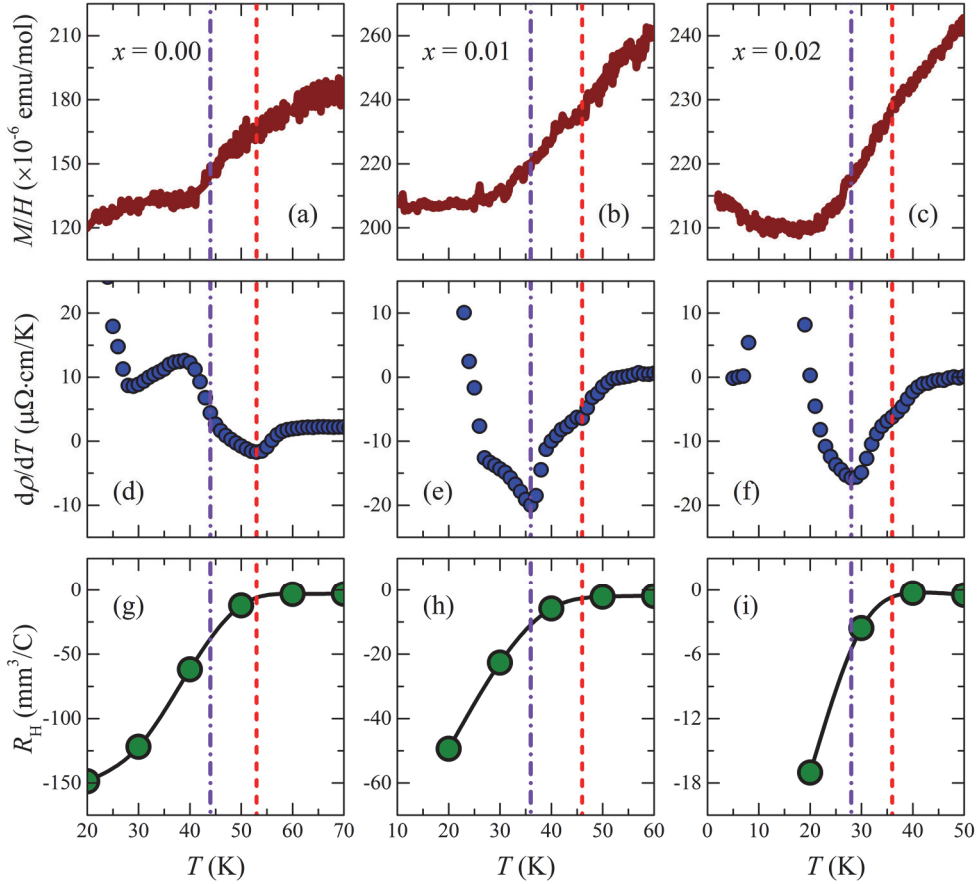


**Figure 7.6.** (a)-(c) The magnetization, (d)-(f) the 1st derivative of the resistivity, and (g)-(i) the Hall coefficient of the low doping crystals. The data of NaFeAs in (a), (d), (g), ( $\text{Na}_{0.99}\text{Li}_{0.01}$ )FeAs in (b), (e), (h), and ( $\text{Na}_{0.98}\text{Li}_{0.02}$ )FeAs in (c), (f), (i) are shown. The solid lines and the circles represent the measured data. The dashed line and dot-and-dashed line indicate the estimated structural and magnetic transition temperature, respectively.

structural and magnetic transition temperatures are realized as  $\sim 46$  and  $36$  K for  $x = 0.01$  and  $\sim 36$  and  $28$  K for  $x = 0.02$ . The Hall coefficients, furthermore, suddenly

increases below the temperature suspected to be the structural transition temperature, which is also consistent with the previous experimental results [4]. One can conclude that all 3 temperature dependent properties presented in figure 7.6 are consistent to each other to provide the traces of the structural and magnetic transitions, therefore.

### 7.5. Complete phase diagram

From the above discussion, the structural, magnetic, and superconducting transition temperatures of the  $(\text{Na}_{1-x}\text{Li}_x)\text{FeAs}$  series are determined. Figure 7.7 summarized the transition temperatures with respect to the Li content  $x$ . While the circles represent the superconducting transition temperature,  $T_c$ , realized from the volume magnetic susceptibility and the resistivity, the squares and pentagons represent the structural and magnetic transition temperatures,  $T_s$  and  $T_{\text{SDW}}$ , respectively, determined from the magnetization and the derivative of the resistivity. The temperature dependence of the Hall coefficient also is employed to determine the structural transition temperatures as discussed above. Solid lines in the figure are drawn as simple guidelines. Since any traces of the structural and magnetic transitions are not found in the specimen of  $x = 0.04$ , the transitions seem to be suppressed fully and disappeared at the Li content between  $0.02 \leq x \leq 0.04$ .

One can conclude that the structural and magnetic transitions are clearly suppressed by the Li substitution in the  $(\text{Na}_{1-x}\text{Li}_x)\text{FeAs}$  series. This suppression is quite similar to the doping dependence of the other NaFeAs-related series such as  $\text{Na}(\text{Fe}_{1-x}\text{Co}_x)\text{As}$  and  $\text{Na}(\text{Fe}_{1-x}\text{Ni}_x)\text{As}$ , but it has to be noted that the Li content is not substituted on the Fe-As tetrahedral layer which is in contrast to the Co or Ni contents. While the magnetic transition is suppressed and disappeared, the superconducting transition is enhanced with the increase of the Li content in the system and becomes

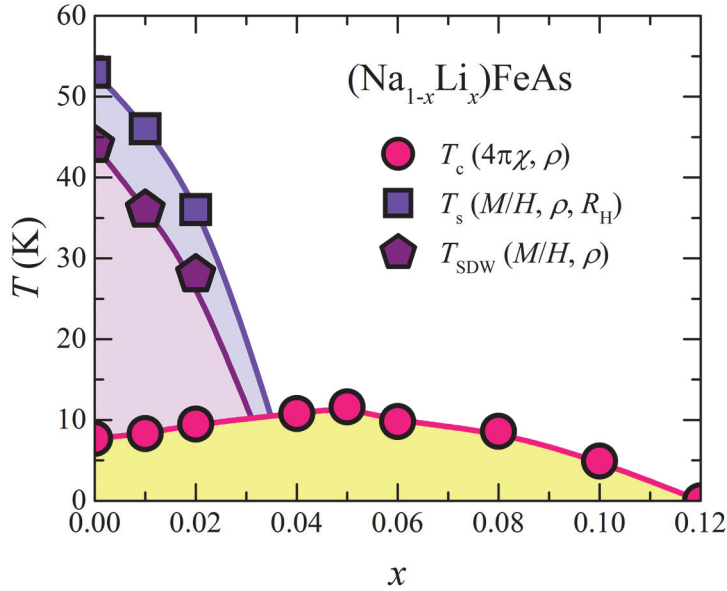


**Figure 7.7. The phase diagram of the  $(\text{Na}_{1-x}\text{Li}_x)\text{FeAs}$  series. Circles, squares, and pentagons represent the superconducting, structural, and magnetic transition temperatures, respectively. Each transition temperature is realized as explained in the text. The solid lines are drawn as guidelines.**

optimal at the doping level of  $x = 0.05$ . The development of the superconductivity is consistent to the understanding that the superconductivity of the Fe-based superconductors competes with the spin-density-wave ground state. It is, however, the very first discovery that the competition between the superconductivity and the spin-density-wave ground state can be controlled by the isovalent substitution in the charge reservoir layer of the Fe-based superconductors.

The substitution with charge-doping, for example  $(\text{Ba}_{1-x}\text{K}_x)\text{Fe}_2\text{As}_2$  [19], is understood to make the balance between the electron- and hole-pockets broken by the Fermi energy level shift induced by the introduction of additional charge carriers, resulting the breaking the nesting condition for the spin-density-wave state and the

superconductivity arisen from the competition while the magnetic state becomes unstable. The Li substitution in  $(\text{Na}_{1-x}\text{Li}_x)\text{FeAs}$ , on the other hand, is supposed not to introduce any additional charge carriers into the system but to control the phase competition between the magnetic and superconducting ground states.

### 7.6. Signature of disorder

One can suspect that the disorder caused by the Li substitution disturbs the stabilization of the spin-density-wave ground state and helps the superconductivity enhanced. The signatures of disorder are easily found in the electrical resistivity. Figure 7.8 shows the resistivity normalized by the room temperature value for the  $(\text{Na}_{1-x}\text{Li}_x)\text{FeAs}$  series. As mentioned previously, the series become more insulating with higher Li content and this trend is clearly distinguished in the figure. This insulating behavior may be somewhat similar to one found in the  $\text{Na}(\text{Fe}_{1-x}\text{Cu}_x)\text{As}$  series which is suspected to be caused by the Anderson localization [7]. Since the Li substitution doesn't modify the bands near the Fermi surface directly, the disorder effect, which may be a precursor of the Anderson localization, is suspected to cause the insulating or semiconducting behavior of the series, even further investigation, of course, has to be done to reveal the real origin.

Another signature of disorder is the transition width realized in the resistivity curves. The transition width is determined as the difference between  $T_{\text{zero}}$  and  $T_{90\%}$ , the temperature where the zero resistivity is achieved and the temperature where 90 % of the normal state resistivity is realized, respectively, and summarized in figure 7.9. The symbols indicate the realized transition width and the dotted line is a guideline. The transition width, as shown in the figure, is  $\sim 15$  K in the un-doped specimen and gradually decreases down to around  $\sim 7.5$  K as the Li content

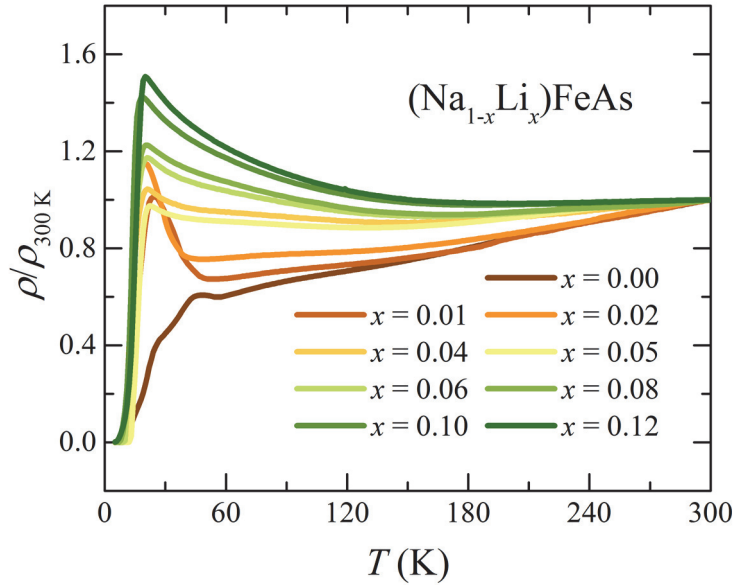


**Figure 7.8. The resistivity normalized with the room temperature resistivity of the  $(\text{Na}_{1-x}\text{Li}_x)\text{FeAs}$  series.**

approaches to the optimal value of 0.05. Then it again slowly increases as the Li content increases. A general consensus about the transition width is that the wider transition width implies more disorder in the system and vice versa. At the low doping region, the superconducting fraction in the system is enhanced to the full bulk limit and the superconducting transition becomes sharper even though the Li content introduces the disorder into the system. At the high doping region, on the other hand, the disorder suppresses the superconductivity as well and the transition becomes wider.

These 2 behaviors, the insulating resistivity and the wider transition width, of the high doping specimens, indicate the disorder induced by the Li substitution in the charge reservoir layer, and the disorder seems to influence on the electronic

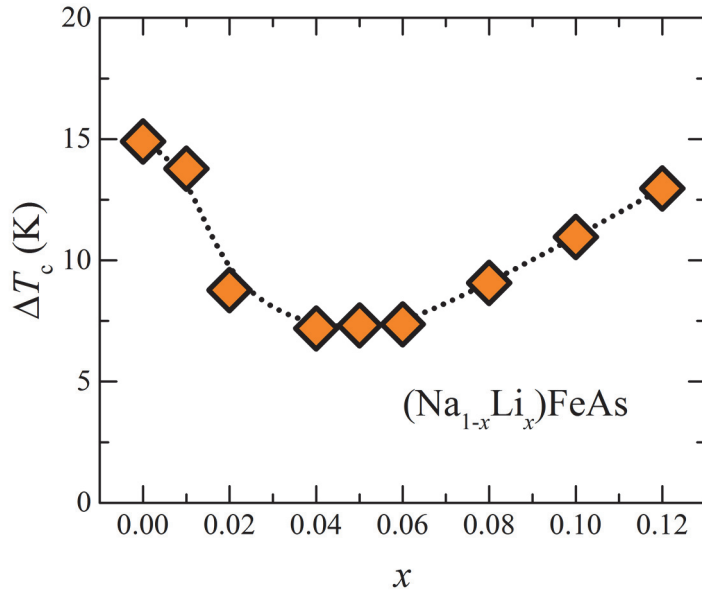


**Figure 7.9.** The transition width in the resistivity of the  $(\text{Na}_{1-x}\text{Li}_x)\text{FeAs}$  series. The transition width, shown as the square, is determined as the difference between the temperatures where the 90 % of the normal state value and the zero resistivity. The dotted line is a guideline by eye.

properties of the system. The disorder effect observed in the resistivity, therefore, is suspected to cause the evolution in the phase diagram and to play an important role in the competition between the superconductivity and the spin-density-wave ground state.

The other possible causes, such as the chemical pressure effect by the substitution, also need to be considered. The argument about the anion height dependence of  $T_c$  for the Fe-based superconductor family, for example, is one of the theory to explain the superconductivity of the entire Fe-based superconductor family [20]. According to the general phase diagram of the transition temperature with respect to the anion height from the Fe layer, however, it is not expected that

the transition temperature is enhanced in the phase space between NaFeAs and LiFeAs, and even NaFeAs itself is difficult to be included in the universal trend of the anion height dependence [20]. The deviation from the general structure-related trend of the Fe-based superconductor family imply that the phase competition in the  $(\text{Na}_{1-x}\text{Li}_x)\text{FeAs}$  series may have another origin such as the disorder effect.

Then, the remaining question is why the disorder caused by the Li substitution in the  $(\text{Na}_{1-x}\text{Li}_x)\text{FeAs}$  only is able to induce the superconductivity. One possible reason is much closer position of the charge reservoir layer from the Fe-As tetrahedral layer. The height of the charge reservoir layer from the Fe layer can be estimated as the difference along the crystallographic  $c$ -axis between the Fe layer and the closest atom in the charge reservoir layer. According to the previous experimental reports, the height of the charge reservoir layer from the Fe layer is 2.4698 Å for NaFeAs [16] while one is 2.1924 Å for LiFeAs [21]. For the other representing compounds, the height is known to be 2.8505 Å for  $\text{CaFe}_2\text{As}_2$ , 3.0911 Å for  $\text{SrFe}_2\text{As}_2$ , 3.2503 Å for  $\text{BaFe}_2\text{As}_2$ , and 3.1333 Å for LaOFeAs [15, 22-24]. One can easily found that the height of the charge reservoir layer is much shorter in the NaFeAs and LiFeAs compounds than the other 122 or 1111 compounds. This closer position of the charge reservoir layer may provide better environment that the disorder in the charge reservoir layer influences to the electronic properties in the Fe-As tetrahedral layer.

### 7.7. $H_{c1}$ and $C_P$ of $(\text{Na}_{0.95}\text{Li}_{0.05})\text{FeAs}$

To investigate the superconducting gap structure, the lower critical fields,  $H_{c1}$ , and the specific heat,  $C_P$ , of the  $(\text{Na}_{0.95}\text{Li}_{0.05})\text{FeAs}$  crystals, which is the optimal one in the series, are measured. Since only the  $(\text{Na}_{0.95}\text{Li}_{0.05})\text{FeAs}$  crystals show the

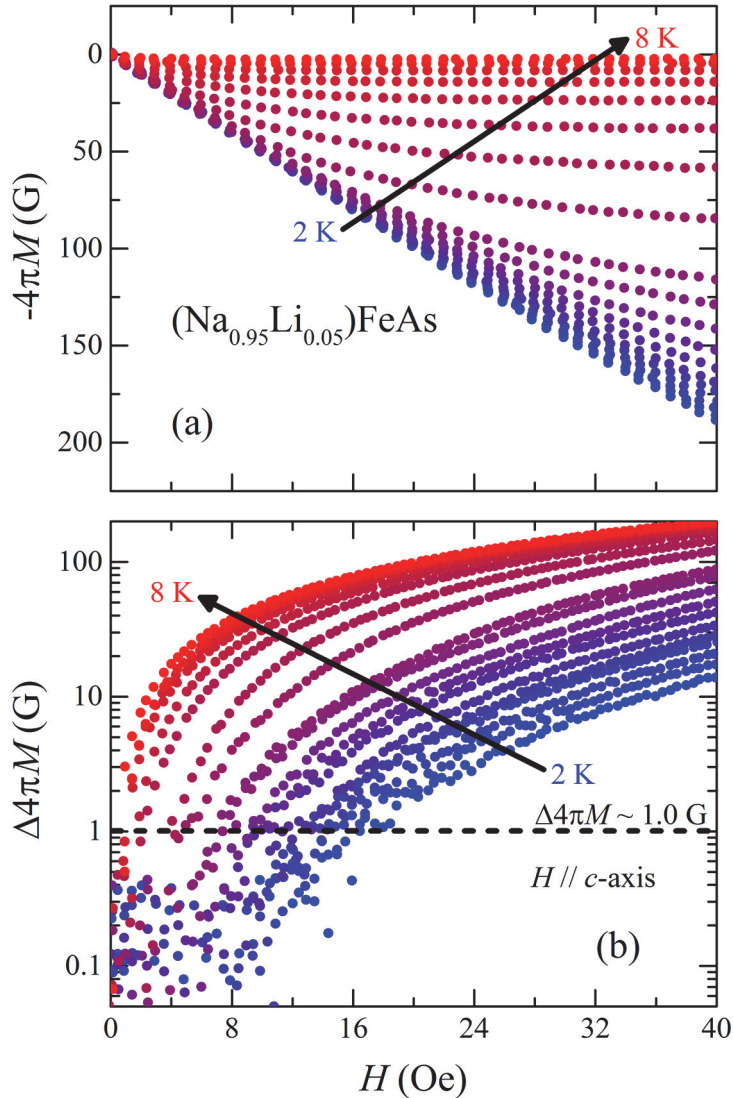


**Figure 7.10.** (a) The magnetic field dependence of magnetization of the  $(\text{Na}_{0.95}\text{Li}_{0.05})\text{FeAs}$  single crystal measured at specific temperature and (b) the difference from the Meissner line. The measurements are performed at the temperature from 2 to 8 K while the magnetic fields are applied along the  $c$ -axis. The dashed line in (b) indicate the criterion of the 1 G difference to determine the lower critical fields as described in the text.

superconducting shielding fraction of  $\sim 100\%$  at 2 K, it is the most favorable candidate with the fully opened bulk superconducting gaps.

The lower critical fields is extracted from the isothermal magnetization curves measured at the temperature from 2 to 8 K as shown in figure 7.10 (a). The magnetic fields dependence of the magnetization is measured with the magnetic field step of  $\sim 0.5$  Oe. The full shielding line, so called the Meissner line, is realized from the linear fitting of the isothermal magnetization curves at very low fields and also the theoretical calculation including the geometry factor [25]. Since the crystal sample used for the  $H_{c1}$  measurements has the size of  $1.45 \times 1.45 \times 0.16$  mm<sup>3</sup>, the geometry factor is estimated to be  $\sim 0.197$  for the sample based on the formula of  $\tanh \sqrt{0.36 \cdot t/w}$  where  $t$  is the thickness and  $w$  is the lateral width of a sample with a square and plate-like shape [25]. The lower critical fields for each temperature are determined as the magnetic fields where the measured curve deviates from the Meissner line. The difference between the measured curves and the Meissner line is presented in figure 7.10 (b). The criterion of  $\Delta 4\pi M \sim 1$  G is employed to determine whether the measured curves deviate from the Meissner line.

The extracted lower critical fields are summarized in figure 7.11 with respect to the temperature. The circles in the figure indicate the extracted values and the solid line represents the temperature dependence from the 2-gap fitting. The transition temperature is determined to be 7.8 K by hand before the fitting performed. A simple isotropic  $s$ -wave gap function is employed for the temperature dependence of the energy gaps and the fitting is performed within the 2-gap model. The overall behaviors of the measured results and the fitted curve seem to agree with each other where the zero temperature value,  $H_{c1}(0)$ , is estimated to be  $\sim 113$  Oe. It should be noted, however, that the fraction of one superconducting gap is almost  $\sim 100\%$  in

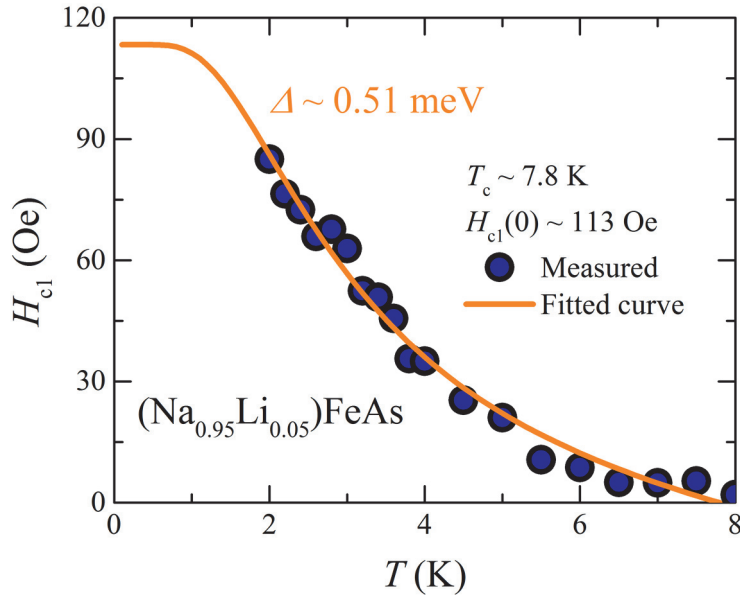


**Figure 7.11.** The lower critical fields of the  $(\text{Na}_{0.95}\text{Li}_{0.05})\text{FeAs}$  single crystal. Circles represent the value measured from the isothermal magnetization curves. The solid line is the calculated curve with the superconducting gap of  $\sim 0.51$  meV, whose value is realized from the fitting based on the 2-gap model. The transition temperature and the zero temperature lower critical fields are estimated as  $\sim 7.8$  K and  $\sim 113$  Oe, respectively.

the fitting results. In addition, the size of the dominant superconducting gap is estimated to be  $\sim 0.51$  meV, which is unexpectedly small and implying a weakly-coupled gap.

The specific heat of the  $(\text{Na}_{0.95}\text{Li}_{0.05})\text{FeAs}$  crystals is also measured to reveal the superconducting gap structure. The specific heat is measured from 2 to 20 K and presented in figure 7.12 (a) as the circles. A large specific heat jump at the superconducting transition temperature is not observed, but a small hump-like feature exists below  $\sim 10$  K. The normal state specific heat including both phonon

and electron contribution is realized from the fitting of the measured data at the temperature window above 11 K. A fitting formula of  $C_P/T = \gamma_N + \beta \cdot T^2 + \delta \cdot T^4$  is employed for the fitting. The red dashed line in figure 7.12 (a) represents the fitted curve. The fitting results the coefficients as  $\gamma_N \sim 5.19$  mJ/mol·K<sup>2</sup>,  $\beta \sim 0.320$  mJ/mol·K<sup>4</sup>, and  $\delta \sim -0.152$  μJ/mol·K<sup>6</sup>. From the phonon contribution, the Debye temperature is estimated to be  $\Theta_D \sim 263$  K. The Sommerfeld coefficient of  $\sim 5.19$  mJ/mol·K<sup>2</sup>, in addition, supports that the Li substitution is the isovalent doping. This value is almost same with one of the un-doped NaFeAs [4], and also relatively smaller than one of the electron-doped Na(Fe<sub>0.0972</sub>Co<sub>0.028</sub>)As [6]. Since the coefficient is known to be proportional to the density of states at the Fermi level, the value estimated to be similar to the un-doped one and smaller than the electron-doped one is supporting the isovalent substitution of the (Na<sub>1-x</sub>Li<sub>x</sub>)FeAs series.

The electronic specific heat is realized as the subtraction of the phonon specific heat from the total specific heat, and presented in figure 7.12 (b). The error bar in the figure represents the standard deviation from the measurements. The green dashed line represents the normal state electronic specific heat, the Sommerfeld coefficient. As shown in the figure, the electronic specific heat is clearly larger than the normal state one at the temperature below  $\sim 10$  K although the jump size is very small. The expected electronic specific heat in the superconducting state is calculated with various gap structure including the 1-gap model as well as the 2-gap model. The orange line, calculated from the transition temperature of  $\sim 9.0$  K and the single *s*-wave superconducting gap with the size of  $\sim 0.5$  meV, seems to agree with the experimental results. More accurate data with smaller error and the specific heat at the lower temperature below 2 K, of course, will be crucial to perform the fitting for the superconducting energy gaps, however the small but clear specific heat jump at

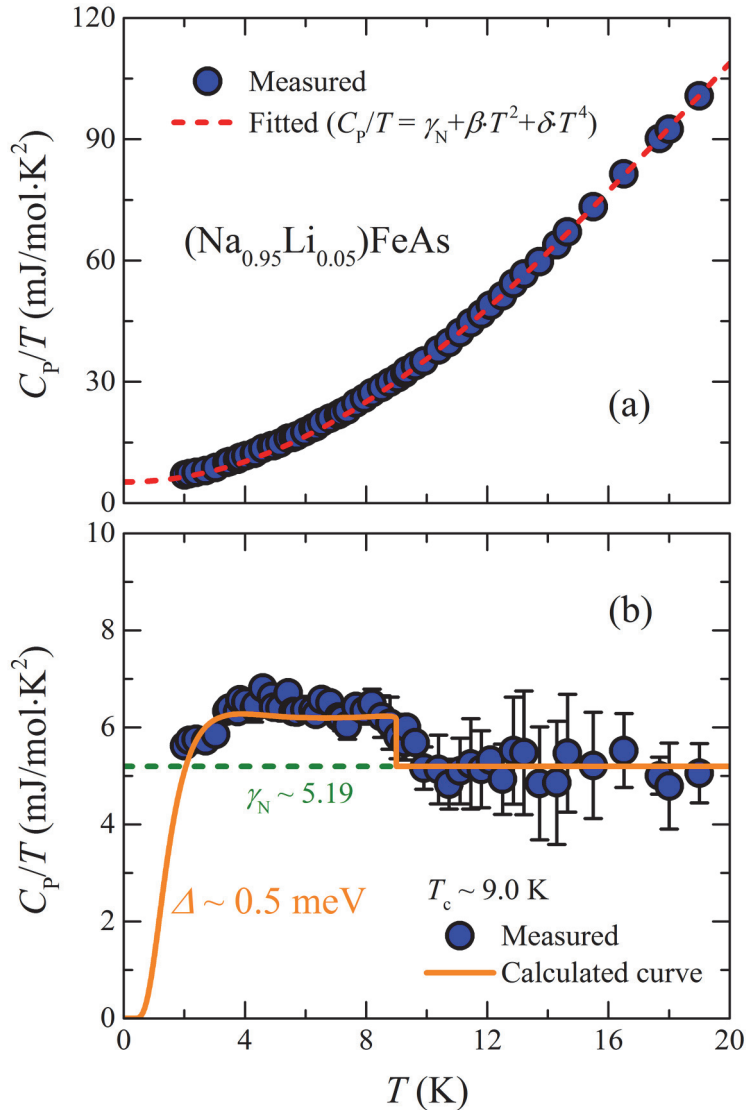


**Figure 7.12.** (a) The total and (b) electronic specific heat of the  $(\text{Na}_{0.95}\text{Li}_{0.05})\text{FeAs}$  single crystals. The circles represent the measured data with the error bar estimated as the standard deviation from the measurements. The dashed lines indicate the normal state specific heat in both (a) and (b) estimated from the fitting described in the text. The solid line is the calculated curve based on the 1-gap model with the gap of  $\sim 0.5$  meV and the transition temperature of  $\sim 9.0$  K.

the superconducting transition temperature still evidences the small-gap-dominant superconducting gap structure of  $(\text{Na}_{0.95}\text{Li}_{0.05})\text{FeAs}$ .

### **7.8. Small-gap-dominant superconductivity**

Both experimental results in this chapter, the lower critical fields and the electronic specific heat, of  $(\text{Na}_{0.95}\text{Li}_{0.05})\text{FeAs}$  imply very similar superconducting gap structure. The gap structure seems to be dominated by the small superconducting gap with the size of  $\sim 0.5$  meV. It is very different from the expectation since the undoped  $\text{NaFeAs}$  is known to be a multi-band system [10] and most of the Fe-based superconductors is known to have multiple superconducting gap as well as multiple bands at the Fermi level [5]. The Li substitution on the Na-site is predicted not to change the Fermi surface topology since it is the isovalent doping on the charge reservoir layer. The band structure of  $(\text{Na}_{0.95}\text{Li}_{0.05})\text{FeAs}$ , therefore, consists of multiple bands at the Fermi energy level, similar to one of  $\text{NaFeAs}$ . Within the assumption of the isovalent doping, the small-gap-dominant gap structure is very unexpected and strange.

One can expect that the gap structure of other  $\text{NaFeAs}$ -related systems provides evidences to understand one of  $(\text{Na}_{0.95}\text{Li}_{0.05})\text{FeAs}$ . Experimental results of the angle-resolved photoemission spectroscopy on the  $\text{Na}(\text{Fe}_{1-x}\text{Co}_x)\text{As}$  single crystals, for instance, are reported and the superconducting gaps at the hole- and electron pockets are discussed for the under-doped and optimally-doped specimens [26]. According to their results, the gap on the hole-pocket at the  $\Gamma$  point is a relatively small gap of  $\sim 5$  meV for both of under-doped,  $x = 0.0175$ , and optimally-doped,  $x = 0.045$ , specimens. The gap on the electron-pockets at the zone corner of the under-doped specimen, on the other hand, is a larger one which is anisotropic and varying from 4

to 7 meV with respect to the direction in the momentum space, while one of the optimally-doped specimen is isotropic with the size of  $\sim 5.4$  meV. These gap structures of the  $\text{Na}(\text{Fe}_{1-x}\text{Co}_x)\text{As}$  series provide several information. First, the gap opened on the hole-pockets at the  $\Gamma$  point is isotropic and almost independent to the Co content, and corresponding introduction of additional electron carriers. In addition, it is the small gap of the system. Second, the gap opened on the electron-pockets are affected a lot and developed by the Co content and the electron doping. And it is the large gap of the system. Since the small gap is independent to the electron doping and the larger gap is highly depending on the electron doping, one can suspect that the small gap on the hole-pockets is also independent to the Li substitution in the  $(\text{Na}_{1-x}\text{Li}_x)\text{FeAs}$  series and the large gap on the electron-pockets of the series is not developed without the introduction of the electron carriers.

The possible scenario is that the disorder effects induced by the Li substitution suppress the spin-density-wave ground state of  $\text{NaFeAs}$  and the superconductivity arises from the competition between the magnetic ground state. Then, the superconducting gap at the hole-pockets, which is the smaller one, is expected to be rigid upon the doping and therefore to play a dominant role in the bulk superconductivity arisen by the Li substitution. The other gap, however, on the electron-pockets seems not to be developed by the isovalent Li doping. The selective evolution of the superconducting gap may cause the lower critical fields and the electronic specific heat dominated by only the small gap without noticeable existence of the large gap. Further and detailed investigation about the band structure as well as the superconducting gap structure of the  $(\text{Na}_{1-x}\text{Li}_x)\text{FeAs}$  series are necessary to prove the scenario much firmly, however the experimental results in this chapter clearly evidences the strange superconducting gap structure of the series.

## 7.9. Summary

In this chapter, the successful single crystal growth and the physical properties of the  $(\text{Na}_{1-x}\text{Li}_x)\text{FeAs}$  series with the Li content up to  $x = 0.12$  are discussed. In the magnetic volume susceptibility in the superconducting state and the electrical resistivity, the superconductivity is found to be enhanced by the Li substitution and to become optimal at  $x = 0.05$ . From the normal state magnetization, the first derivative of the resistivity, and the Hall coefficients, the traces of the structural and magnetic transitions are observed in the low doping region. The phase diagram of the series is presented based on the observation of the transition temperatures, and the disorder introduced by the Li substitution is expected to suppress the spin-density-wave ground state and let the superconductivity arise from the phase competition. The superconducting gap structure, in addition, of the optimal  $(\text{Na}_{0.95}\text{Li}_{0.05})\text{FeAs}$  is investigated from the lower critical fields and the electronic specific heat. The experimental results clearly indicate the small gap of  $\sim 0.5$  meV is dominating the superconductivity in the system. This unexpected gap structure seems to be caused by the disorder effect without the introduction of any additional charge carrier, but more detailed study is expected to prove it firmly.

## 7.10. References

- [1] I. Morozov *et al.*, *Cryst. Growth & Des.* **10**, 4428 (2010)
- [2] Y. J. Song *et al.*, *Appl. Phys. Lett.* **96**, 212508 (2010)
- [3] B. Lee *et al.*, *Europhys. Lett.* **91**, 67002 (2010)
- [4] G. F. Chen *et al.*, *Phys. Rev. Lett.* **102**, 227004 (2009)
- [5] G. R. Stewart, *Rev. Mod. Phys.* **83**, 1589 (2011)

- [6] A. F. Wang *et al.*, Phys. Rev. B **85**, 224521 (2012)
- [7] A. F. Wang *et al.*, Phys. Rev. B **88**, 094516 (2013)
- [8] D. R. Parker *et al.*, Phys. Rev. Lett. **104**, 057001 (2010)
- [9] J. D. Wright *et al.*, Phys. Rev. B **85**, 054503 (2012)
- [10] C. He *et al.*, Phys. Rev. Lett. **105**, 117002 (2010)
- [11] P. Cai *et al.*, Nature Comm. **4**, 1596 (2013)
- [12] B. C. Sales *et al.*, Phys. Rev. B **79**, 094521 (2009)
- [13] S. Jiang *et al.*, J. Phys.: Condens. Matter **21**, 382203 (2009)
- [14] A. Thaler *et al.*, Phys. Rev. B **82**, 014534 (2010)
- [15] M. Rotter *et al.*, Phys. Rev. B **82**, 014513 (2010)
- [16] D. R. Parker *et al.*, Chem. Commun. **2009**, 2189 (2009)
- [17] K. Kitazawa *et al.*, J. Phys. Soc. Jpn. **80**, 033705 (2011)
- [18] S.-H. Baek *et al.*, (to be submitted)
- [19] C. Liu *et al.*, Phys. Rev. Lett. **101**, 177005 (2008)
- [20] Y. Mizuguchi *et al.*, Supercond. Sci. Technol. **23**, 054013 (2010)
- [21] M. J. Pitcher *et al.*, Chem. Commun. **2008**, 5918 (2008)
- [22] R. Mittal *et al.*, Phys. Rev. B **83**, 054503 (2011)
- [23] M. Tegel *et al.*, J. Phys.: Condens. Matter **20**, 452201 (2008)
- [24] Y. Kamihara *et al.*, J. Am. Chem. Soc. **130**, 3296 (2008)
- [25] E. H. Brandt, Phys. Rev. B **60**, 11939 (1999)
- [26] Q. Q. Ge *et al.*, Phys. Rev. X **3**, 011020 (2013)

## 8. Conclusion

In this thesis, the comprehensive investigations on the superconducting properties of the LiFeAs, NaFeAs, and related compounds are discussed. Preparation of high quality single crystals is the key to expand available phase space, and properly designed flux methods are successfully employed to do so. By the Sn- and self-flux method, the  $\text{Li}(\text{Fe}_{1-x}\text{Co}_x)\text{As}$ ,  $\text{Li}(\text{Fe}_{1-x}\text{Mn}_x)\text{As}$ , and  $(\text{Na}_{1-x}\text{Li}_x)\text{FeAs}$  single crystals are prepared and examined to study the doping and impurity effects on the normal state properties as well as on the superconductivity.

At the early of this work, the physical properties of LiFeAs are investigated in the very first crystals grown by the Sn-flux method, and the bulk superconductivity is confirmed. The upper critical anisotropy near the transition temperature is estimated to be  $\sim 2.3$ , which evidences the electron-electron correlation in the system. The initial slope of the upper critical fields is also measured for many crystal pieces whose residual resistivity as well as the impurity level are controlled, and it is revealed that the initial slope is independent to the impurity level in the piece. The results imply the clean limit superconductivity of LiFeAs.

The  $\text{Li}(\text{Fe}_{1-x}\text{Co}_x)\text{As}$  single crystals are grown by the Sn-flux method. The electrical resistivity of the  $\text{Li}(\text{Fe}_{1-x}\text{Co}_x)\text{As}$  series shows the Fermi liquid behavior at the low temperature. From the transport properties, the Co content induces the gradual increase of the residual resistivity ratio to the room temperature resistivity and the sudden increase of the Fermi liquid  $T^2$  coefficient. Since the increase of the residual resistivity ratio indicates the absence of the scattering between the conducting electrons and the spin fluctuations, the change of the Fermi liquid coefficient is caused by the change of the Fermi surface topology. The introduction

of additional electron carrier by the Co doping shifts the Fermi energy level in the  $\text{Li}(\text{Fe}_{1-x}\text{Co}_x)\text{As}$  series, and it causes the increase of the coefficient.

The  $\text{Li}(\text{Fe}_{1-x}\text{Mn}_x)\text{As}$  single crystals are grown by the self-flux method, and their electrical resistivity and magnetization are measured. The superconducting transition is suppressed very quickly by the Mn content while the magnetization of the series clearly has the Curie-Weiss-like temperature dependence. From the fitting, the Curie-Weiss coefficient is obtained for each specimen and it is realized that the density of the local magnetic moments increases as the Mn content increases, implying that the Mn content acts as the magnetic impurity in the system. The strong suppression of the superconductivity by the Mn content, therefore, is understood as the magnetic impurity effect on the superconducting transition temperature. Based on the comparison with the cases of other non-magnetic impurities, the suppression by the Mn content is consistent with the theoretical prediction of the  $s\pm$ -wave gap symmetry. The results, therefore, evidence the  $s\pm$ -wave gap symmetry, regardless of other possible gap symmetry, and also the spin-fluctuation-mediated pairing mechanism of  $\text{LiFeAs}$ .

At last, the single crystals of  $(\text{Na}_{1-x}\text{Li}_x)\text{FeAs}$  series are prepared by the self-flux method and the phase diagram is discussed with the complete superconducting dome. By the Li substitution in the charge reservoir layer, the spin-density-wave state is suppressed and the superconductivity is enhanced. It is the first observation among the Fe-based superconductor family that the superconductivity is developed by the isovalent doping on the charge reservoir layer. The disorder seems to be induced by the Li substitution, and it is expected to influence the phase competition between the magnetic ground state and the superconductivity. The superconducting gap structure, furthermore, of the optimal  $(\text{Na}_{0.95}\text{Li}_{0.05})\text{FeAs}$  crystals is examined by the means of

lower critical fields and electronic specific heat. Temperature dependences of the lower critical fields and the specific heat are fitted and compared with the theoretical calculation based on the 2-gap model. The both results agree well with the small-gap-dominant structure with the gap size of  $\sim 0.5$  meV, which is unique in the Fe-based superconductor family. It is suspected that the large gap opened at the electron-pocket is not developed by the isovalent Li substitution while the small gap opened at the hole-pocket is more rigid upon the doping.

## List of publications

1. “Enhanced density of states in  $\text{Li}(\text{Fe}_{1-x}\text{Co}_x)\text{As}$  single crystals near  $x = 0.06$  as implied by transport properties”, **Bumsung Lee**, Seunghyun Khim, Byung-Jo Jeon, Ju-Young Park, Suk Ho Lee, Ki-Young Choi, G. R. Stewart, and Kee Hoon Kim, *Physica C* **495**, 130-133 (2013).
2. “Single-crystal growth and superconducting properties of  $\text{LiFeAs}$ ”, **Bumsung Lee**, Seunghyun Khim, Jung Soo Kim, G. R. Stewart, and Kee Hoon Kim, *Europhys. Lett.* **91**, 67002 (2010).
3. “Longer-range lattice anisotropy strongly competing with spin-orbit interactions in pyrochlore iridates”, L. Hozoi, H. Gretarsson, J. P. Clancy, B.-G. Jeon, **B. Lee**, K. H. Kim, V. Yushankhai, Peter Fulde, D. Casa, T. Gog, Jungho Kim, A. H. Said, M. H. Upton, Young-June Kim, and Jerome van den Brink, *Phys. Rev. B* **89**, 115111 (2014).
4. “Enhanced upper critical fields in a new quasi-one-dimensional superconductor  $\text{Nb}_2\text{Pd}_x\text{Se}_5$ ”, Seunghyun Khim, **Bumsung Lee**, Ki-Young Choi, Byung-Gu Jeon, Dong Hyun Jang, Deepak Patil, Seema Patil, Rokyeon Kim, Eun Sang Choi, Seongsu Lee, Jaejun Yu, and Kee Hoon Kim, *New J. Phys.* **15**, 123031 (2013).
5. “Temperature- and Magnetic-Field-Induced Change of Electric Polarization in a Multiferroic  $\text{Mn}_{0.93}\text{Co}_{0.07}\text{W}_{0.93}\text{O}_{4-\delta}$  Single Crystal”, Li Qin Yan, **Bumsung Lee**, Sae Hwan Chun, Ingyu Kim, Jae-Ho Chung, Sung Baek Kim, Ju-Young

- Park, Suk Ho Lee, Yisheng Chai, and Kee Hoon Kim, *J. Phys. Soc. Jpn.* **82**, 094708 (2013).
6. “Orbital Selective Fermi Surface Shifts and Mechanism of High  $T_c$  Superconductivity in Correlated  $A\text{FeAs}$  ( $A = \text{Li, Na}$ )”, Geunsik Lee, Hyo Seok Ji, Yeongkwan Kim, Changyoung Kim, Kristjan Haule, Gabriel Kotliar, **Bumsung Lee**, Seunghyun Khim, Kee Hoon Kim, Kwang S. Kim, Ki-Seok Kim, and Ji Hoon Shim, *Phys. Rev. Lett.* **109**, 177001 (2012).
  7. “Probing the order parameter of superconducting  $\text{LiFeAs}$  using  $\text{Pb/LiFeAs}$  and  $\text{Au/LiFeAs}$  point-contact spectroscopy”, Xiaohang Zhang, **Bumsung Lee**, Seunghyun Khim, Kee Hoon Kim, Richard L. Greene, and Ichiro Takeuchi, *Phys. Rev. B* **85**, 094521 (2012).
  8. “Pauli-limiting effects in the upper critical fields of a clean  $\text{LiFeAs}$  single crystal”, Seunghyun Khim, **Bumsung Lee**, Jae Wook Kim, Eun Sang Choi, G. R. Stewart, and Kee Hoon Kim, *Phys. Rev. B* **84**, 104502 (2011).
  9. “Magnetic-field-dependent pinning potential in  $\text{LiFeAs}$  superconductor from its Campbell penetration depth”, Plengchart Prommapan, Makariy A. Tanatar, **Bumsung Lee**, Seunghyun Khim, Kee Hoon Kim, and Ruslan Prozorov, *Phys. Rev. B* **84**, 060509 (2011).
  10. “Electronic structure of detwinned  $\text{BaFe}_2\text{As}_2$  from photoemission and first principles”, Yeongkwan Kim, Hyungju Oh, Chul Kim, Dongjoon Song, Wonsig Jung, Beomyoung Kim, Hyoung Joon Choi, Changyoung Kim, **Bumsung Lee**, Seunghyun Khim, Hyungjoon Kim, Keehoon Kim, and

Yongseung Kwon, *Phys. Rev. B* **83**, 064509 (2011).

11. “Chemical doping-induced flop of ferroelectric polarization in multiferroic  $\text{Mn}_{0.9}\text{Co}_{0.1}\text{WO}_4$ ”, Y.-S. Song, Li Qin Yan, **Bumsung Lee**, Sae Hwan Chun, Kee Hoon Kim, Sung Baek Kim, A. Nogami, T. Katsufuji, J. Schefer, and J.-H. Chung, *Phys. Rev. B* **82**, 214418 (2010).
12. “Realization of Giant Magnetoelectricity in Helimagnets”, Sae Hwan Chun, Yi Sheng Chai, Yoon Seok Oh, Deepshikha Jaiswal-Nagar, So Young Haam, Ingyu Kim, **Bumsung Lee**, Dong Hak Nam, Kyung-Tae Ko, Jae-Hoon Park, Jae-Ho Chung, and Kee Hoon Kim, *Phys. Rev. Lett.* **104** 037204 (2010).

## **Appendix A. Manual for the arc melting chamber**

Nb bombs have advantages over quartz ampoules. The bomb can hold much higher pressure than the quartz. The melting temperature of Nb is also much higher than one of the quartz. Nb is expected to less react with other metals including the alkali and alkaline earth metals than the quartz. These advantages make much more various growth conditions possible. Single crystals containing Na, for example, are difficult to grow with the quartz ampoule because Na evaporates easily at high temperature and the Na vapor reacts with the quartz to break it. The Nb bomb, therefore, is a perfect substitute of the quartz ampoule for the growth of that crystals.

The arc melting chamber is employed in this thesis to weld the Nb bombs. Because of the high melting temperature of Nb,  $\sim 2477$  °C, typical torch technique with the mixture of oxygen and propane gas can't be used to weld the bombs. The arc melting method can provide much higher temperature. With this aspect, the arc melting chamber is prepared. Figure A.1 shows the arc melting chamber used in this work. It consists of a main chamber with a handle, a high voltage power supply, a diffusion pump, and a touchscreen panel. Every operation can be done by the touchscreen panel. In this appendix, the procedure to operate the arc melting chamber properly including the Nb bomb welding.

### **How to activate the diffusion pump**

- ① Open the cooling water inlet valve at the sink. If the water flow is enough, the water pressure warning on the panel disappeared. Also check the water flow coming out through the outlet.
- ② Turn on the rotary pump placed behind the chamber and close the rotary

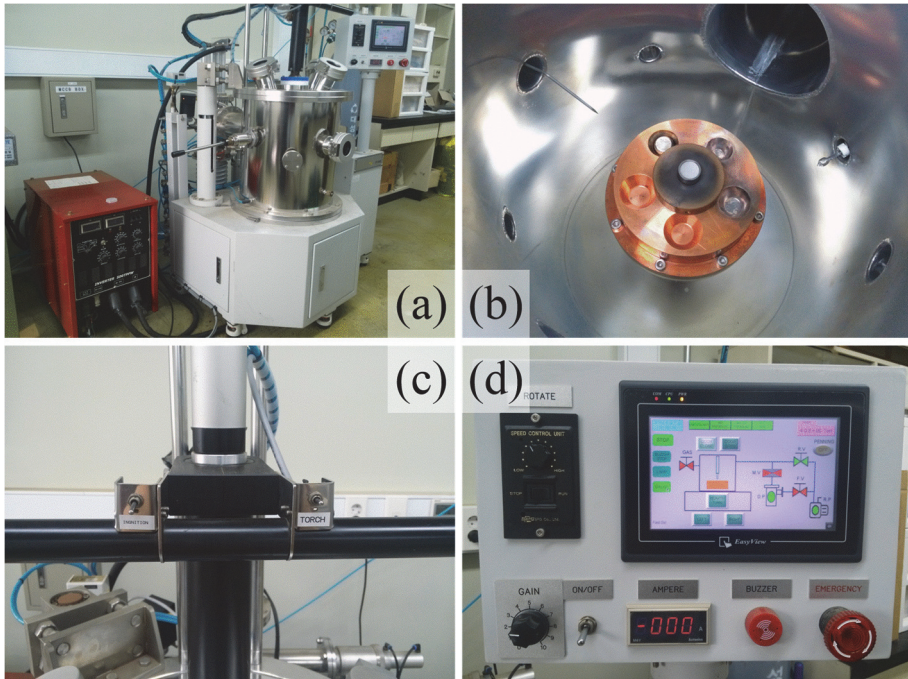


**Figure A.1. Photograph of the arc melting chamber. (a) Overall equipment including the power supply as the red metal box, (b) inside of the chamber with the hearth top containing a Nb bomb to weld, (c) the handle with the IGNITION and TORCH switches at left and right respectively, and (d) the touchscreen panel with the rotation speed knob, the gain knob, and the emergency stop switch.**

pump venting valve shown as R.P. in the panel. Only the R.P. button becomes green when it is closed and red when it is opened. Other valves in the panel has opposite relation, green is open and red is close.

- ③ Wait more than 1 minute, and then open the backing valve shown as F.V. in the panel. The inside of the diffusion pump will be pumped out.
- ④ Turn on the heater of the diffusion pump by press the D.P. button.
- ⑤ Wait more than 1 hour to heat up the oil inside the diffusion pump.

## **How to place the sample to melt or the bomb to weld**

- ① Close the diffusion valve and the roughing valve, shown as the M.V. button and the R.V. button in the panel, respectively.
- ② Open the venting valve if the chamber is not vented. Press the DOOR OPEN button on the panel to open the chamber.
- ③ Do not touch whatever inside the chamber with bare hands. The bare hands contaminate the chamber. Any materials which can be an outgassing source must be excluded from the chamber.
- ④ If the sample would be loaded, clean the Cu crucibles at the hearth with acetone very carefully. Then, place the sample in one of the crucibles. The pellet form is expected to be more appropriate for the arc melting.
- ⑤ If the bomb would be loaded, secure the hearth top part first. The inside the chamber and the hearth top should not be touched by bare hands.
- ⑥ Unscrew 2 bolts in the part to disassemble the hearth top into 2 halves. Place the prepared bomb between the 2 halves with a piece of Cu foil to make the mechanical and electrical contact between the bomb and the hearth better. And then, screw the 2 bolts to tighten up the hearth top.
- ⑦ Mount the hearth top on the hearth by screwing. Tighten enough to make sure the contact between them.
- ⑧ Press the DOOR CLOSE button on the panel to close the chamber. While the door is closed automatically, it is better to align the door to the chamber by hand. Misalignment may disrupt the closing. Bad o-ring seal can cause the vacuum problem.

### **How to purge the chamber**

- ① Place the sample in the chamber and close the chamber properly.
- ② Close the backing valve, F.V., on the panel. And then open the roughing valve, R.V., to pump the chamber.
- ③ Turn on the gauge by pressing the GAUGE button on the panel after the pressure of the analogue gauge becomes less than 100 torr.
- ④ Wait until the pressure read from the Pirani gauge becomes less than  $10^{-1}$  torr. Then, close the roughing valve.
- ⑤ Press the GAS button to fill the chamber with the Ar gas. Fill the gas more than 650 torr read from the analogue gauge. However, do not exceed the atmosphere, 760 torr.
- ⑥ Repeat the sequence from 2 to 5 more than 2 times to purge the chamber 3 times. Remember that always more purging is better.
- ⑦ After the last purging, wait until the pressure becomes less than  $10^{-1}$  torr.
- ⑧ Close the roughing valve, open the backing valve, and open the diffusion valve, M.V. to pump out the chamber by the diffusion pump.
- ⑨ If the Pirani gauge becomes under-ranged, wait more than 30 minutes from that moment. The Penning gauge can be turned on manually, but do not let the Penning gauge turned on for long time. The pressure is expected to be almost minimum after 1-hour-pumping by the diffusion pump.

### **How to melt or weld**

- ① If the chamber is purged enough, close the diffusion valve. And open the gas valve with the GAS button on the panel to fill the Ar gas in the chamber.

The inside pressure is determined based on the purpose, but do not exceed the atmosphere, 760 torr. Too high pressure makes the ignition difficult.

- ② During the gas filling, turn on the power supply, press the HEARTH TURN button to rotate or to align the hearth, and adjust the position of the torch with the TORCH switch on the handle. Close the gas valve after the filling.
- ③ If the sample to melt is loaded, aim at the edge of the crucible. The sample itself has poor electrical connection with the hearth, therefore the ignition is difficult. If the bomb to weld is loaded, aim at the position where is very close vertically but slightly outer horizontally from the edge of the bomb.
- ④ Grip the handle very carefully. The torch tip must not touch anything.
- ⑤ Click the ignition switch at the handle to make a flame. Don't worry even though the flame is not ignited easily. It is very common. Treat the switch similar to a disposal cigarette lighter. Try again until it is ignited. If the ignition is too difficult, adjust the tip position closer to the target.
- ⑥ If the flame is ignited, at first, move the torch away from the target. It is usually very strong to destroy everything. Adjust the distance between the torch tip and the target carefully. The bomb can be collapsed.
- ⑦ To melt the sample thoroughly, control the flame to approach the sample from many directions. Flip the sample for the back-side. Turn off the flame for a short time to flip and turn it on again.
- ⑧ Click the ignition switch to turn it off. Switch off the power supply after all.
- ⑨ Wait at least 1 hour to cool down the sample or the bomb. And then, vent the chamber with the venting valve at the front of the chamber. Release it to fill the air and open the door. Take out the sample or the bomb carefully

## **Appendix B. Service manual for the glove box**

A glove box is the very essential equipment in the experimental investigation on the intermetallic compounds. For this thesis, the glove box with purified Ar atmosphere whose oxygen and moisture levels are controlled to be below 1 ppm is used. To maintain the atmosphere inside, the pure Ar gas has to be supplied continuously and the purifier equipped in the glove box has to be regenerated periodically. In this appendix, how to service the glove box is noted.

### **How to change the Ar gas cylinder**

- ① Check the pressure of the cylinder frequently. Stock extra Ar cylinders always. The cylinder with the purity of 99.999 % is used usually. This purity is equal to 10 ppm of impurities.
- ② If the pressure of the cylinder becomes zero, close the main valve at the top of the cylinder and open the regulator valve to stop the gas flowing.
- ③ Loosen the connection between the regulator and the cylinder. Separate the regulator from the cylinder and place it safely.
- ④ Bring new cylinder and change the old one with it.
- ⑤ Connect the regulator to the new cylinder but do not tighten it much. Small leakage is needed at the moment.
- ⑥ Prepare to tighten the regulator, and then open the main valve slightly. While the gas is leaking, tighten the regulator immediately after realizing the leaking.
- ⑦ Close the regulator valve slightly and make some gas flow. Adjust the regulator pressure to appropriate value.

## **How to regenerate the purifier**

- ① Secure the forming gas cylinder. Typical forming gas of He 5 % and Ar mixture gas can be used. It has to be connected to the glove box properly.
- ② Make sure the venting line from the vent port at the back of the glove box is connected to proper outlet. The moisture will come out during the regeneration procedure.
- ③ Turn off the blower. The pressure control doesn't need to be turned off.
- ④ Press the RGN button on the panel. Check the pneumatic valves at the inlet and outlet of the purifier are closed. The purifier is equipped at the bottom cabinet of the glove box. The pneumatic valves have a yellow line indicating the status. The yellow line should be rotated. The pressure for the pneumatic valves are supplied from the Ar cylinder, therefore the cylinder must be connected to the glove box always.
- ⑤ Press the START button on the panel. Then the HEAT indicator is turned on and the purifier starts to be heated up. It takes 3 hours.
- ⑥ After the heating of 3 hours, the purifier is purged and the PURGE indicator is turned on. The forming gas is supplied only during the purging. Check the gas flowing. The flowmeter level should be at around the middle. It takes 2 hours.
- ⑦ After the purging of 2 hours, the purifier is evacuated and the EVA indicator is turned on. The forming gas flow will stop and the moisture will come out through the vent port. It takes 8 hours.
- ⑧ After the evacuating of 8 hours, the REFILL indicator is turned on and the sequence is over. Press the RGN button again to open the pneumatic valves.

Check the valves are working properly with the yellow lines. When the valves are opened again, a lot of Ar gas in the glove box is sucked into the purifier because it is fully evacuated during the regeneration. Be careful about the sudden decrease of the pressure inside the glove box.

- ⑨ After the pressure stabilized, turn on the blower and set the blower speed to maximum. Let the regenerated purifier purifies the atmosphere.
- ⑩ When the oxygen level becomes less than 1 ppm and stabilized, set the blower speed to lower value. Slightly less than the middle is usually used.

## **Appendix C. Capillary preparation for XRD**

An X-ray diffraction measurement with a capillary has advantages over typical powder X-ray diffraction measurements. First of all, powders in a spinning capillary can't have any preferred orientation. It is possible, in addition, to seal capillaries made of quartz or glass with a torch or a lighter to protect the powder from any kind of exposure if it is necessary. These advantages provide better opportunities to measure more accurate diffraction patterns.

However, there are also disadvantages and difficulties of the capillary measurement. The capillary demands the Debye-Scherrer geometry while the typical sample holder does the Bragg-Brentano geometry. And the powder sample for the capillary has to be very fine. If the powder is not fine enough, the capillary will be blocked and one will not be able to put enough powder into it. Careful loading of the powder is important.

Weaker diffraction intensity is another weakness of the capillary measurement. Relatively smaller amount of the sample in the cross section reduce the measured intensity, but one can't increase the intensity simply with more sample. While the diffraction happens at the surface of the sample in the Bragg-Brentano geometry with typical sample holders, the transmission through the sample and the capillary is accompanied by the diffraction. More sample, therefore, causes longer path to transmit resulting reduction of the intensity.

From the experiences, several options are considered as the optimal ones. Thinner capillary with very fine powder filled as much as possible is better for most of cases. Good alignment for the spinning stage and a combination of appropriate slits are also important. Below sequence is the procedure to prepare the capillary and

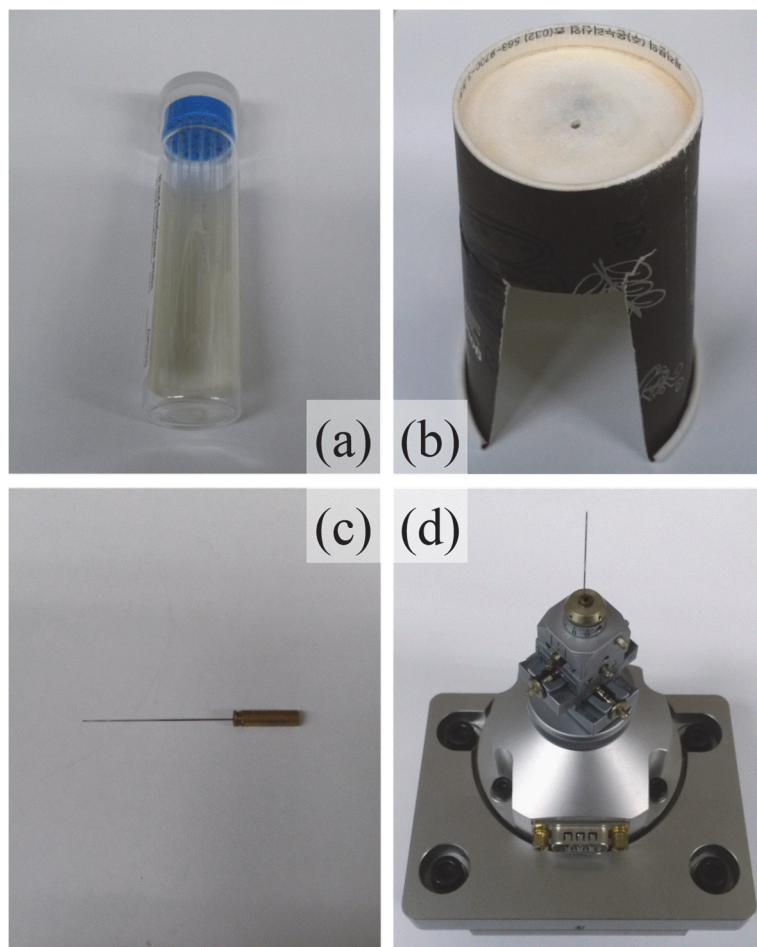


**Figure C.1. Photograph of (a) the capillaries in the bottle, (b) a holder with a hole made of a paper cup, (c) the capillary loaded in the Cu adaptor, and (d) the spinning capillary stage.**

to perform the measurement with it.

- ① Prepare the sample. Whether the sample is crystal pieces or powder, size of the particle must be very small or very fine. If not, it will not go into the capillary.
- ② Take out a capillary from the carrier and put it into a hole of a holder.

Usually, a paper cup with a hole at its bottom is employed as a holder. Be careful not to break the capillary.

- ③ Pour the sample into the capillary. Since the entrance of the capillary is very narrow, a guiding carrier with sharp ends are necessary. An weighing paper folded along its diagonal is good to use. Do not pour the sample too fast. Slower pouring is usually better.
- ④ Let the sample placed at the very end of the capillary. Shaking or knocking the capillary can be helpful. Not to break the capillary, use the holder for shaking or knocking.
- ⑤ Seal or cut the capillary carefully after the sample loading. Appropriate length is about 5-7 cm. Sealing is better than cutting because there is no chance to spill the sample.
- ⑥ Put the prepared capillary into an adaptor. The Cu adaptor has a groove at one side and the capillary is better to be placed at the grooved side. Apply paraffin in the empty hole of the adaptor and melt it with a soldering machine. When the paraffin is melted, put the capillary into the hole carefully. It is better to align the capillary straight before the paraffin solidifies.
- ⑦ Mount the adaptor with the capillary on the spinning stage properly.
- ⑧ Align the stage to make the capillary very straight. There are 2 linear stages and 2 angular alignment goniometers on the stage. During the alignment, try to rotate the stage manually to check the status.
- ⑨ Mount the stage on the diffractometer and connect the motor power supply cable to the stage. Turn on the switch to spin the capillary.
- ⑩ Measure the diffraction for short window around a peak to check the signal-

to-background ratio. Change the slit combination to find out the optimal combination.

- ⑪ Measure the diffraction pattern carefully. Many repetition with proper time-per-step should be done to accumulate enough intensity.

## Appendix D. Drawings and designs

Several tools are designed for this thesis and other experiments. In this appendix, drawings and photographs of the designed tools are presented. Key ideas of the designs are also discussed.

### Specific heat probe for CCR

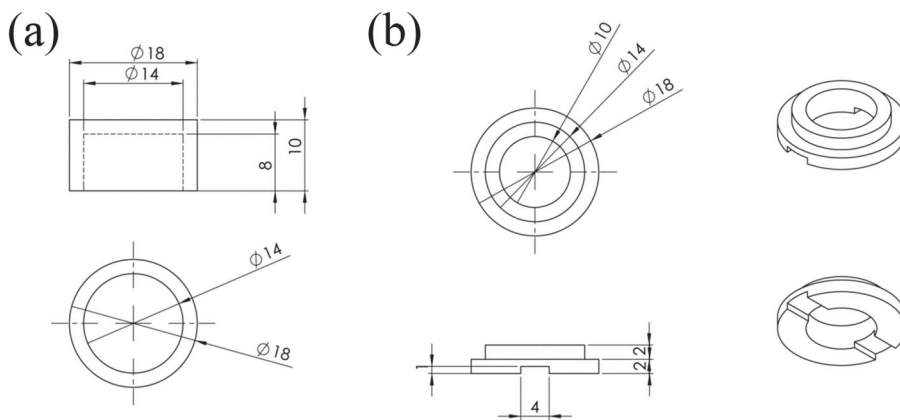


**Figure D.1. The drawings of the specific heat probe for CCR. (a) The radiation cap and (b) the bottom ring.**

Figure D.1 shows the drawings of the radiation cap and the bottom ring of the specific heat probe for CCR. The cap and the ring are made of brass. The cap is mounted on the ring by screwing. For this, the screw thread is prepared for both sides. At the bottom of the ring, grooves are machined for the wires and also for the gas flow. Thick copper wires are attached at the inner side the ring by the stycast to support the platform and also to provide electrical connection. Figure D.2 presents the photograph of the resultant probe. It is attached on CCR by the varnish. The old

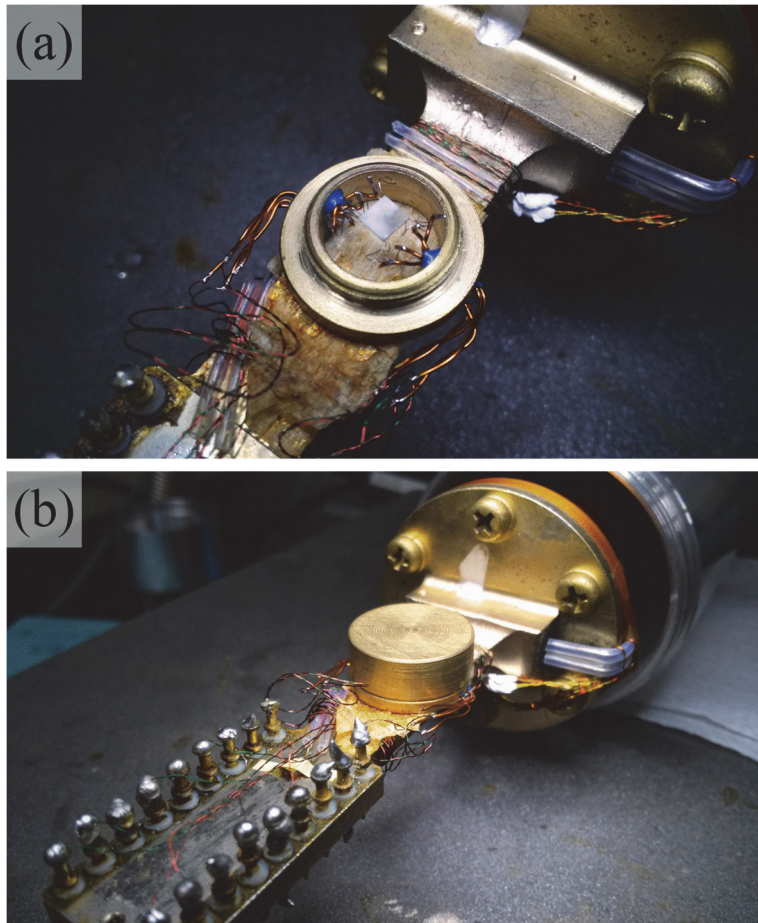


**Figure D.2. The photographs of the specific heat probe attached on CCR. (a) The platform and the ring without the cap and (b) the capped probe.**

PPMS platform is employed.

### **$^3\text{He}$ cryostat for the pulsed field magnet**

A  $^3\text{He}$  cryostat is designed for the pulsed field magnet with a custom-designed  $^4\text{He}$  cryostat. To make it compatible to the existing  $^4\text{He}$  cryostat, the bore size is limited. Figure D.3 presents the drawings of parts and the schematic figure of the

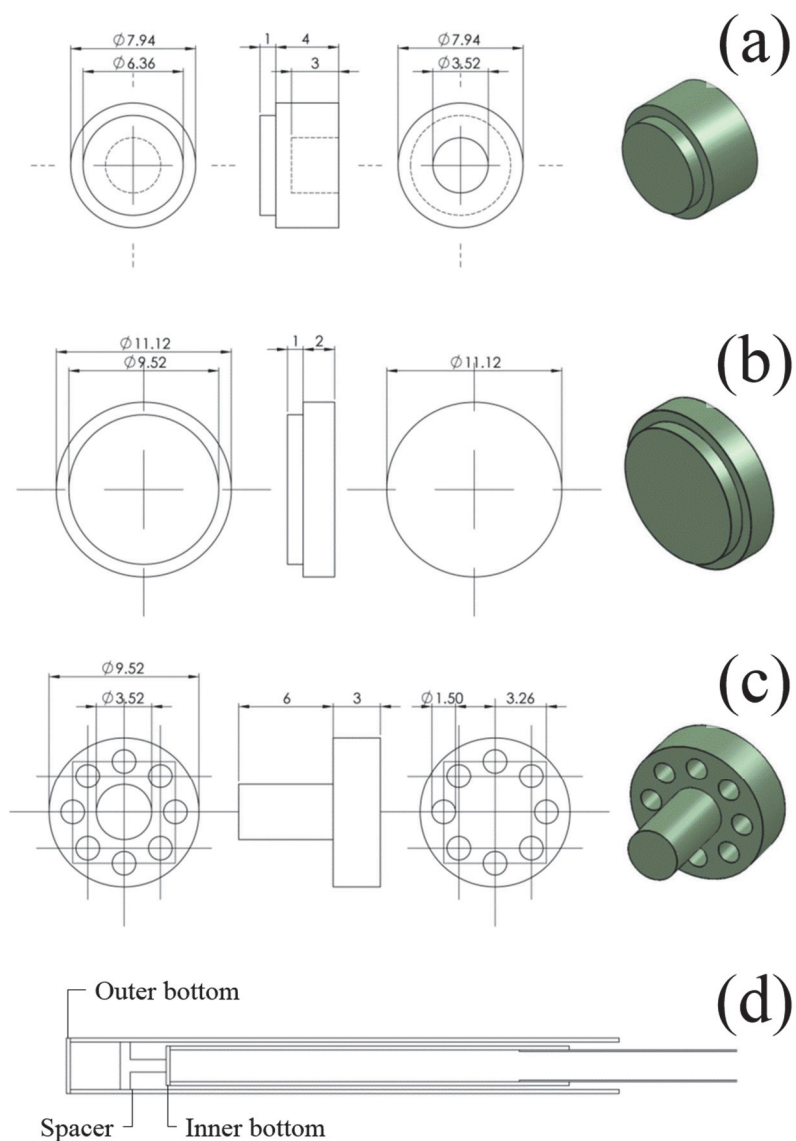


**Figure D.3. The drawings of (a) the inner bottom, (b) the outer bottom, and (c) the spacer noted in (d) the schematic figure of the  $^3\text{He}$  cryostat.**

assembled cryostat. All parts are made of the G10 plastic. Enough space between the

inner G10 tube and outer one is necessary to break the thermal contact between the sample space, inside of the inner tube, and the  $^4\text{He}$  liquid, which will be at the outside of the outer tube. The space is expected to be vacuum by the cryogenic pumping of charcoal. The spacer is prepared to make the space enough for the charcoal. The inner bottom part is attached at the end of the inner tube by the stycast. The other side of the G10 tubes are connected to the thin stainless steel tube and also sealed by the stycast. And then the charcoal is placed in the space. This procedure to load the charcoal is performed in the glove box filled with the pure argon gas without nitrogen or oxygen. The outer bottom part is also attached on the tube at last, and it also done in the glove box. After all, all G10 parts are covered by the stycast to prevent the  $^3\text{He}$  leakage.

### **Magneto-caloric effect probe for CCR**

Basically, the measurement of the magneto-caloric effect is very similar to one of the specific heat under the adiabatic condition. The temperature change due to the fast magnetic field sweep has to be measured before the heat is relaxed to the bath. To achieve the adiabatic condition, one can consider 2 options. First one is to reduce the thermal conduction between the sample and the bath as little as possible. However, it also results the long waiting time for the temperature stabilization before the measurements. Another option is to sweep the magnetic fields fast enough to neglect the thermal relaxation. The probe for CCR in this appendix is designed and built for the latter option. Figure D.4 shows the drawings of several parts and figure D.4 does the photograph of the resultant probe.

The sample platform, shown in figure D.4 (a), is made of teflon to reduce the thermal relaxation, and the radiation cap, shown in figure D.4 (b), is made of brass

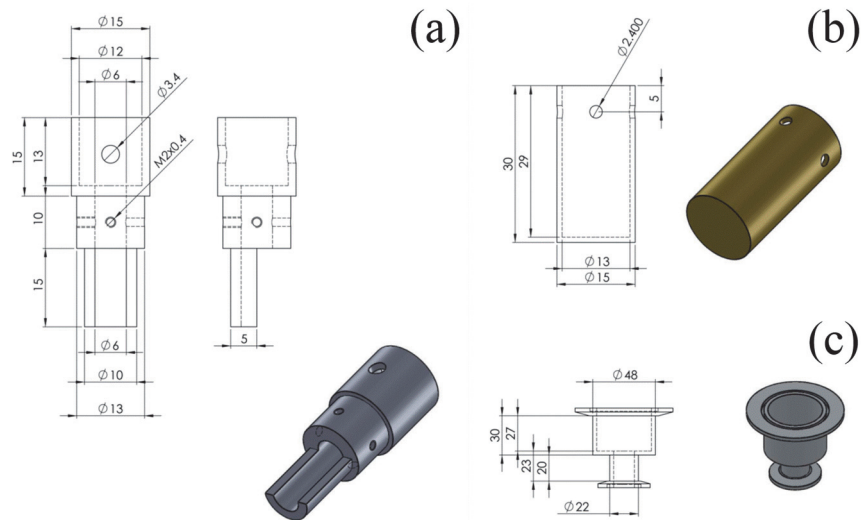


**Figure D.4. The drawings of (a) the sample platform, (b) the radiation cap, and (c) the fitting for the electrical feedthroughs of the magneto-caloric effect probe.**

and fixed on the sample platform with brass screws. The electrical feedthroughs are attached on the top of the fitting shown in figure D.4 (c). The sample platform has the hemisphere shape with hollow inside to hang the sample with minimum contact to the thermal bath. The resultant probe is equipped on CCR with extended vacuum chamber. To maintain the vacuum level, the chamber of CCR is evacuated by a turbo pump. A Pt-100 temperature sensor is used to measure the sample temperature, as shown in figure D.5 (c). The sensor is directly attached on the polycrystalline sample with the crystal glue. The wires are wound on the platform for the thermal stabilization.

To control the sample temperature, the end of the probe, the brass radiation cap, is touched to the coldhead of CCR before sweeping the magnetic fields. The

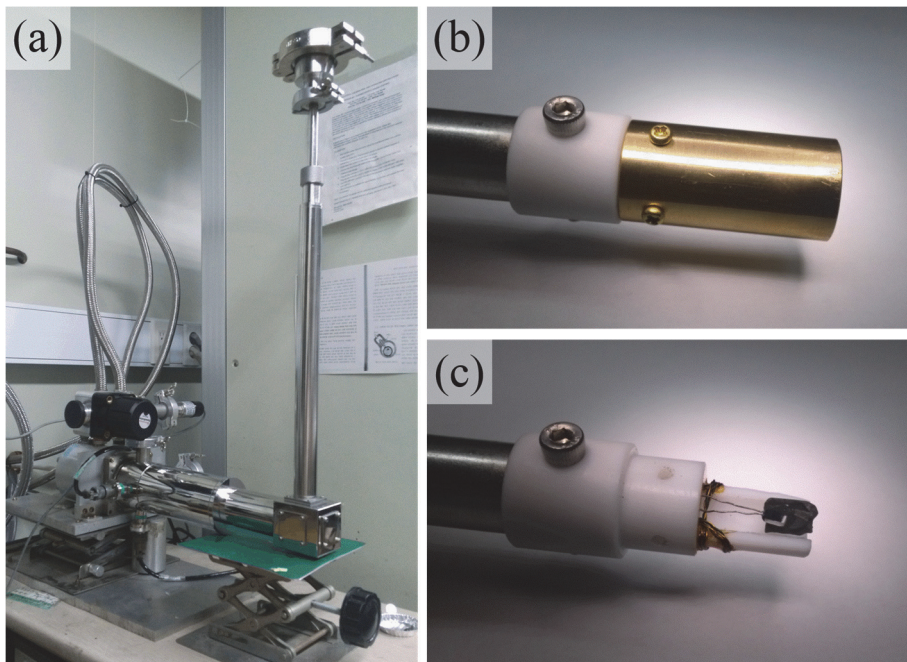
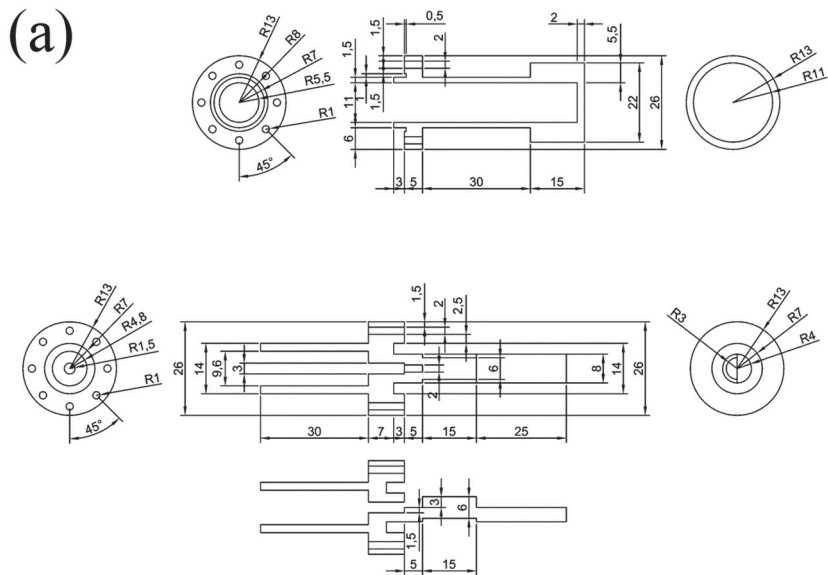


**Figure D.5. The photograph of (a) the assembled probe, (b) the sample platform with the radiation cap, and (c) the sample loaded on the platform with the temperature sensor.**

temperature controller connected to CCR is used to control the background temperature. With the sliding seal at the top of the extended chamber, one can move the probe without breaking the vacuum. To sweep the magnetic fields, CCR is placed in a DC magnet and the constant magnetic fields are applied continuously. After the temperature is stabilized, the probe is detached slightly from the coldhead and the background temperature drift is measured with respect to the time. And then, the probe is pulled out as quick as possible. Since the magnetic fields produced by the magnet is highest at the center, to pull out the probe from the center is effectively same to the down sweep of the magnetic fields. The temperature is recorded during the sweeping.



(b)

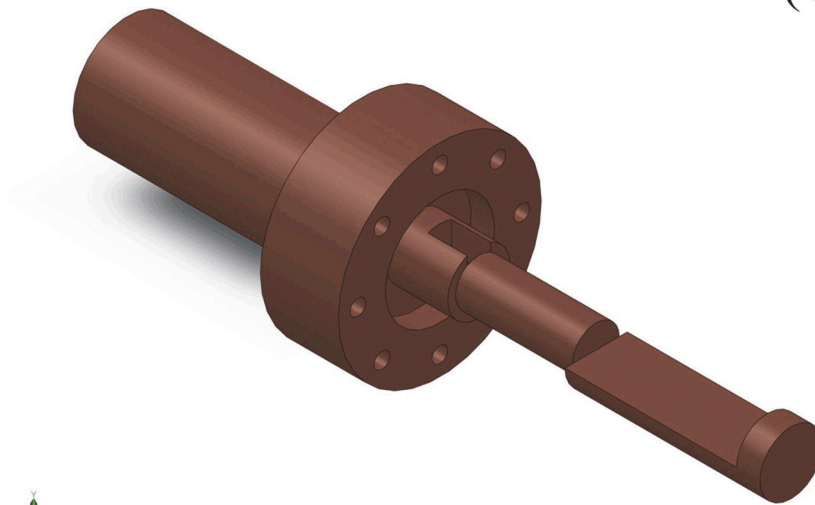


Figure D.6. (a) The drawings of the vacuum cap and the sample platform and (b) the schematic figure of the platform of the In-sealed vacuum dipstick.

### **In-sealed vacuum dipstick**

A dipstick whose sample space can be evacuated and sealed is designed. Indium metal which is very soft is employed to seal the probe. Figure D.6 presents the drawings of the In-sealed vacuum dipstick. There is a groove at the platform to put indium in. Indium filled in the groove is squeezed by 8 pairs of bolt and nut which are placed at the holes around the platform. Since the parts are made of copper with the gold coating, the screw thread can't be machined. The bolt-nut pairs should be outside of the indium groove. Used indium can be recycled by melting. The cap is designed within the consideration of the compatibility to PPMS.

## Appendix E. Mathematica codes

One of many powerful functions of Mathematica from Wolfram Research is to solve or calculate equations numerically. For example, the temperature dependence of the electronic entropy and the lower critical fields can be numerically evaluated from the formula including some complex integrals. In this appendix, the codes to simulate the electronic entropy and the lower critical fields are presented. In addition, the code to fit the experimental results of the lower critical fields is also presented. One has to be careful about the capital letters of the functions. Several programming grammar are also important, for example to distinguish “=” and “:=”, and “\_” right after the parameters. It is recommended to learn about detailed rules from other references such as textbooks and the help browser of the program.

### Simulation of the electronic entropy

```
k=8.6173324*10^-2      /* Boltzmann constant */
Ts=9                   /* Superconducting transition temperature */
f[T_,eps_]:=1/(Exp[eps/(k*T)] + 1)      /* Fermi function */
d1[T_,d10_]:=d10*Tanh[1.82*(1.018*(Ts/T - 1))^0.51]
d2[T_,d20_]:=d20*Tanh[1.82*(1.018*(Ts/T - 1))^0.51]
                        /* Gap functions for 2 gaps */
i1[T_,d10_]:=NIntegrate[(f[T, eps]*Log[f[T, eps]] + (1 - f[T, eps])*Log[(1 - f[T,
eps]]))*eps/Sqrt[eps^2 - d1[T, d10]^2], {eps,d1[T, d10], 50}]
i2[T_,d20_]:=NIntegrate[(f[T, eps]*Log[f[T, eps]] + (1 - f[T, eps])*Log[(1 - f[T,
eps]]))*eps/Sqrt[eps^2 - d1[T, d20]^2], {eps,d1[T, d20], 50}]
                        /* Numerical integrations for 2 gaps */
```

```

s[T_,d10_,d20_,f1_,gn_]:=6/Pi^2/k*(i1[T, d10]*f1 + i2[T, d20]*(1 - f1))*gn
/* Entropy equation for the 2-gap model */
s1[T_,d10_,gn_]:=6/Pi^2/k*i1[T, d10]*gn
/* Entropy equation for the 1-gap model */

d10=1.3
d20=3.0 /* Gap size at zero temperature of 2 gaps */
f1=0.65 /* Fraction of the gap #1 */
gn=0.00519476 /* The normal state electronic specific heat  $\gamma_N$  */
spc 0.01 /* Temperature spacing to evaluate */
ent=Table[{T, s[T, d10, d20, f1, gn]}, {T, spc, Ts - spc, spc}]
/* Calculated entropy for the 2-gap model */
ent1=Table[{T, s1[T, d10, gn]}, {T, spc, Ts - spc, spc}]
ent2=Table[{T, s1[T, d20, gn]}, {T, spc, Ts - spc, spc}]
/* Calculated entropy for the 1-gap model */
Show[ListPlot[ent,PlotRange->All,PlotStyle->{Red,PointSize->0.02}],
ListPlot[ent1,PlotRange->All,PlotStyle->{Blue,PointSize->0.01}],
ListPlot[ent2,PlotRange->All,PlotStyle->{Green,PointSize->0.01}]]
/* Showing a plot of the results */

```

### Simulation of the lower critical fields

```

D=Import["D:\\Working on\\Mathematica\\BS386.txt","table"]
/* Importing the data as a table */
k=8.6173324*10^-2 /* Boltzmann constant */
Ts=16.2 /* Superconducting transition temperature */
f[T_,eps_]:=1/(Exp[eps/(k*T)] + 1) /* Fermi function */

```

```

d1[T_,d10_]:=d10*Tanh[1.82*(1.018*(Ts/T - 1))^0.51]
d2[T_,d20_]:=d20*Tanh[1.82*(1.018*(Ts/T - 1))^0.51]
/* Gap functions for 2 gaps */
i1[T_,d10_]:=NIntegrate[D[f[T,eps],eps]*eps/Sqrt[eps^2-d1[T,d10]^2],
{eps,d1[T,d10],50}]
i2[T_,d20_]:=NIntegrate[D[f[T,eps],eps]*eps/Sqrt[eps^2-d2[T,d20]^2],
{eps,d2[T,d20],50}] /* Numerical integrations for 2 gaps */
r[T_,H0_,d10_,d20_,f1_]:=H0*(1+2*(f1*i1[T,d10]+(1-f1)*i2[T,d20]))
/* Hc1 equation for the 2-gap model */
r1[T_,H0_,d10_]:=H0*(1+2*i1[T,d10])
/* Hc1 equation for the 1-gap model */
H0=502 /* Hc1 at zero temperature */
d10=2.71
d20=0.56 /* Gap size at zero temperature of 2 gaps */
f1=0.61 /* Fraction of the gap #1 */
res=Table[{T,r[T,H0,d10,d20,f1]},{T,0.1,Ts,0.1}]
/* Calculated Hc1 for the 2-gap model */
res1=Table[{T,r1[T,H0,d10]},{T,0.1,Ts,0.1}]
res2=Table[{T,r1[T,H0,d20]},{T,0.1,Ts,0.1}]
/* Calculated Hc1 for the 1-gap model */
Show[ListPlot[d,PlotRange->All,PlotStyle->{Black,PointSize->0.03}],
ListPlot[res,PlotRange->All,PlotStyle->{Red,PointSize->0.02}],
ListPlot[res1,PlotRange->All,PlotStyle->{Blue,PointSize->0.01}],
ListPlot[res2,PlotRange->All,PlotStyle->{Green,PointSize->0.01}]]
/* Showing a plot of the results with the data*/

```

## Fitting of the lower critical fields

```

data=Import["D:\\Working on\\Mathematica\\BS386.txt","table"]
          /* Importing the data as a table */
kb=8.6173324*10^-2      /* Boltzmann constant */
Tc=16                  /* Superconducting transition temperature */
dfermi[T_?NumberQ,epsilon_?NumberQ]:=
  -Exp[epsilon/(kb*T)]/(kb*T*(Exp[epsilon/(kb*T)] + 1)^2)
          /* Fermi function */
delta1[T_?NumberQ,delta10_?NumberQ]:=
  delta10*Tanh[1.82*(1.018*(Tc/T - 1))^0.51]
delta2[T_?NumberQ,delta20_?NumberQ]:=
  delta20*Tanh[1.82*(1.018*(Tc/T - 1))^0.51]
          /* Gap functions for 2 gaps */
integ1[T_?NumberQ,delta10_?NumberQ]:=Re[NIntegrate[dfermi[T,epsilon]
  *epsilon/Sqrt[epsilon^2-delta1[T,delta10]^2],{epsilon,delta1[T,delta10],50},
  PrecisionGoal->3,MaxRecursion->100]]
integ2[T_?NumberQ,delta20_?NumberQ]:=Re[NIntegrate[dfermi[T,epsilon]
  *epsilon/Sqrt[epsilon^2-delta2[T,delta20]^2],{epsilon,delta2[T,delta20],50},
  PrecisionGoal->3,MaxRecursion->100]]
          /* Numerical integrations for 2 gaps */
rho[T_?NumberQ,Hc10_?NumberQ,delta10_?NumberQ,delta20_?NumberQ,x1_?
  NumberQ]:=Hc10*(1+2*(x1*integ1[T,delta10]+(1-x1)*integ2[T,delta20]))
          /* Hc1 equation for the 2-gap model */
fit=NonlinearModelFit[data,{rho[T,Hc10,delta10,delta20,x1],450<Hc10<600,0<de

```

```

lta20<delta10<20,0<x1<1},{Hc10,530},{delta10,3.0},{delta20,0.5},{x1,0.0
5}},T,PrecisionGoal->3,MaxIterations->1000]
      /* Fitting of the data with the 2-gap model */
fit["ParameterTable","AdjustedRSquared","RSquared"]
      /* Defining the fitting results */
Show[ListPlot[data,PlotRange->All,PlotStyle->{Black,PointSize->0.03}],
      Plot[fit[T],{T, 0, Tc},PlotRange->All,PlotStyle->{Red,Thickness[0.01]}]]
      /* Showing a plot of the fit with the data*/

```

## 국문초록

철기반 초전도체는 2008년 새롭게 발견된 비전통적인 초전도체로써, 유명한 구리산화물 고온 초전도체가 발견된 이후 가장 큰 관심을 모은 비전통적 초전도체이다. 특히 철기반 초전도체는 구리산화물 초전도체와 많은 유사한 특징을 갖고 있는데, 원형 물질이 자기적 기저 상태를 갖는 가운데 화학적 치환 혹은 첨가나 외부 압력에 의해 초전도 현상이 유도되는 것이 가장 중요한 공통점이다. 이러한 흥미로운 특징들로 인해 철기반 초전도체는 응집물질물리학계의 많은 관심을 얻었고, 이에 대한 집중적인 연구가 이루어질 수 있었다. 그러한 연구를 통해 철기반 초전도체는 많은 밴드로 이루어진 페르미 면을 갖고 있으며 스핀 요동이 그 초전도 쌍의 형성을 매개하는 것이 밝혀졌다. 이러한 특징들로 인해 철기반 초전도체의 초전도 갭은 기존의 초전도체들과는 달리  $s_{\pm}$ -파 갭 대칭성을 갖게 된다는 것이 예측되었다.

이러한 철기반 초전도체 가운데, 111 계라고 불리는  $\text{LiFeAs}$ 와  $\text{NaFeAs}$ 는 다른 철기반 초전도체의 원형 물질들과는 달리 대단히 흥미로운 기저 상태를 갖는 예외적인 물질들이다.  $\text{LiFeAs}$ 의 경우 치환이나 압력이 없는 상태에서도 구조적 혹은 자기적 상전이가 없는 온전한 초전도체인 반면,  $\text{NaFeAs}$ 는 반강자성 스핀-밀도-파동 상과 초전도 상이 공존하는 기저 상태를 갖고 있다. 이렇게 특수한 기저 상태를 갖는 물질들은 해당 물질들의, 나아가 철기반 초전도체의 초전도 현상과 그에 관련된 상 경쟁을 연구하기에 좋은 대상이라고 생각된다.

이 학위논문에서는 용제법을 통한 성공적인  $\text{LiFeAs}$  및  $\text{NaFeAs}$  단결정 성장을 보고하고, 여러 종류의 첨가물이 더해진 단결정 시료들에 대한 실험을 통해 111 계의 초전도 현상에 대해 연구한 결과를 논한다.

먼저 LiFeAs 단결정의 자화율과 비열 측정을 통해 해당 물질의 온전한 초전도상을 확인하였다. 상전이 온도 근처에서의 윗임계 자기장이 측정되었고, 그 이방성을 통해 전자간의 상호작용이 존재하는 것을 증명하였다. 또한 윗임계 자기장의 초기 기울기를 통해 LiFeAs이 깨끗한 초전도체임을 인지하였다.

첨가물에 의한 물성 변화는  $\text{Li}(\text{Fe}_{1-x}\text{Co}_x)\text{As}$  및  $\text{Li}(\text{Fe}_{1-x}\text{Mn}_x)\text{As}$  군에 대해서 연구하였다.  $\text{Li}(\text{Fe}_{1-x}\text{Co}_x)\text{As}$  군의 비저항 측정을 통해 해당 군이 저온 영역에서 페르미 액체의 온도 의존성을 보이며 페르미 액체  $T^2$  계수가 Co 첨가량이 증가함에 따라 증가하는 것을 발견하였다. 이러한 계수의 증가는 Co 첨가물의 증가와 함께 추가적인 전자가 물질에 첨가됨에 따라 발생한 페르미 에너지 준위의 이동으로 인한 것으로 예상된다. 반면 Mn 첨가물의 경우는  $\text{Li}(\text{Fe}_{1-x}\text{Mn}_x)\text{As}$  군의 자화율 측정을 통해 국소적인 자기 모멘트를 만드는 것을 확인하였다. 또한 Mn 첨가물에 의한 초전도 상의 억제 속도가 Co 첨가물 혹은 Cu 첨가물에 의한 억제 속도에 비해 매우 빠른 것도 확인하였다. 이러한 결과는 LiFeAs의 초전도 갭 대칭성이  $s_{\pm}$ -파이며 스핀 요동이 초전도 쌍 형성을 매개한다는 것을 의미한다.

마지막으로 해당 물질들의 자화율, 비저항, 그리고 홀 효과가 측정을 통해  $(\text{Na}_{1-x}\text{Li}_x)\text{FeAs}$  군의 상그림을 완성하였다. Li 치환에 의해 스핀-밀도-파동 상이 억제되었고, 이에 따라 초전도 상이 상 경쟁을 통해 유도되었다. 또한 가장 높은 상전이 온도를 갖는  $(\text{Na}_{0.95}\text{Li}_{0.05})\text{FeAs}$ 의 초전도 갭 구조를 연구하기 위하여 해당 물질의 아랫임계 자기장과 비열을 측정하였다. 이 물성들을 분석하여 이 물질의 초전도 상에서는 약 0.5 meV의 작은 초전도 갭이 지배적인 역할을 하고 있는 것을 확인하였다. 이렇게 초전도 상을 유도하고 작은 갭이 지배적인 초전도 갭 구조를

만드는 Li 치환 효과의 근본적인 특성 및 기작에 대해서 논하였다.

주요어: 철기반 초전도체, 초전도 단결정 성장, 상 평형도, 불순물 효과,  
상 경쟁, 초전도 에너지 갭.

학 번: 2008-20445